Final Technical Report

High Reynolds Number Micro-bubble and Polymer Drag Reduction Experiments

HR0011-04-1-001

Prof. Steven L. Ceccio (Principal Investigator)
Mechanical Engineering, University of Michigan, Ann Arbor

Prof. David R. Dowling (Co-Principal Investigator)
Mechanical Engineering, University of Michigan, Ann Arbor

Prof. Marc Perlin (Co-Principal Investigator)
Naval Architecture and Marine Engineering, University of Michigan, Ann Arbor

Prof. Michael Solomon (Co-Principal Investigator)
Chemical Engineering, University of Michigan

Background: This effort was a continuation of the joint ONR and DARPA programs of the PI and Co-PI's initiated as part of the DARPA Friction Drag Reduction Program (ATO/TTO). The purpose of the investigation was to examine the physics and engineering of friction drag reduction methods for turbulent boundary layers (TBL) found in hydrodynamic flows. Three methods of friction drag reduction (FDR) were examined:

- ***Polymer Drag Reduction***- solutions containing extensible, long-chain molecules are injected into a TBL. The polymer molecules interact with the underlying turbulent flow and lead to a reduction of the correlated velocity fluctuations and, hence, a reduction of the turbulent transport of momentum across the TBL. This leads to local drag reduction of up to ~70% for a TBL flow over smooth surfaces compared to a flow without polymer injection.

- ***Micro-bubble Drag Reduction***- air is injected into the TBL with the aim of producing a large volume of small bubbles in the near-wall region of the TBL. The presence of the bubbles reduces the bulk density of the fluid near the wall and possibly alters the turbulent velocity fluctuations. These effects can combine to locally reduce the friction drag over 80%.

- ***Air Layer Drag Reduction***- air is injected into the TBL with the aim of creating a stable gas layer of very high void fraction (> 80% void fraction), separating the liquid flow from the solid surface. This results in friction drag reductions of over 80% compared to the friction drag of an unmodified TBL.

These FDR methods have been studied for some time on the laboratory scale, yielding a great deal of information on their engineering potential and underlying methods. However, the flow physics responsible for FDR does not easily scale from the laboratory to full-scale hydrodynamic applications. Hence, our effort focused on conducting a series of experiments at both large size scales and high Reynolds numbers in order to further explore the flow physics and practicality of these FDR methods.

Our experiments were performed on a canonical TBL flow formed on a flat plate, zero-pressure gradient boundary layer. The maximum length of the test model was ~ 10 m, and the maximum velocity of the flow was ~ 20 m/s, making the Reynolds number based on maximum length ~ 200 million. Our experiments were conducted in the William B. Morgan Large Cavitation Channel (LCC), owed and operated by the Naval Surface Warfare Center-Carderock Division of the U. S. Navy.

During this portion of our research program, three rounds of testing in the LCC were conducted:

- Phase III (Polymer FDR)
- Phase IV (MBDR/ALDR)
- Phase V (Polymer FDR).

Two additional rounds of testing were conducted under the first portion of ONR and DARPA support: Phase I was a baseline test of the model, and Phase II was on MBDR. Also, a portion of Phase V was devoted to examining the influence of roughness on Polymer FDR and ALDR. This portion of the effort was supported under DARPA contract "Influence of Surface Roughness on Polymer Drag Reduction" (HR0011-06-1-0057), and these results are included in the final report for that effort.

All of the experimental efforts were conducted in coordination with modeling efforts conducted by DARPA contractors. The planning, conduct, and data analysis were jointly coordinated, and the experimental results of this test program were used to verify and validate the model development for polymer FDR and MBDR. The results of these comparisons are not presented here, but are presented in the final reports of those contractors. In this report, the principal findings of our effort are summarized. Moreover, a more detailed presentation of our methods, analysis, and results are included as appendices (which represent manuscripts intended for archival publication in the technical journals).

Baseline High Reynolds Number Flow: The flow over the test model represents a high-quality data set combining friction drag and near-wall velocity data for a high Reynolds number TBL. This data and analysis are presented in *Appendix A*, and this work has been submitted for publication in the *Journal of Fluid Mechanics*.

- Oweis, G. F., Winkel, E. S., Cutbirth, J. M., Ceccio, S. L., Perlin, M., and Dowling, D. R., "Smooth-Flat-Plate Turbulent Boundary Layer Measurements at High Reynolds Number," *Journal of Fluid Mechanics*, (submitted) (2008)

Polymer Drag Reduction: The injection of solutions containing long-chain polymers into the TBL will result in significant reductions in friction drag, which is a well-documented phenomenon. The use of polymer injection for external flows presents a singular challenge. In external flows, the mixing of the injected polymer in the TBL is reduced at the highest levels of drag reduction. But, the mixing across the TBL never ceases. Hence, the near-wall concentration of the polymer will be continually reduced downstream of the injection location (usually a line source perpendicular to the stream-wise direction). As the near-wall concentration of polymer is reduced, the amount of drag reduction is decreased until the effect is lost. In the present experiments, we examined a variety of parameters that influence the amount of drag reduction that was achieved through the injection of aqueous solutions of Poly(Ethylene Oxide). The influence of polymer flux, concentration, molecular weight, and injector geometry on the developed friction drag reduction were examined. These data were combined with measurements of the local near-wall polymer concentration and flow fields to understand how the mixing processes influence the reduced drag. Finally, measurements of the polymer solution rheology prior to and after injection were employed to examine the processes of flow induced polymer degradation.

Appendix B presents detailed results from our polymer drag reduction effort. This work has been submitted for publication in the *Journal of Fluid Mechanics*:

- Winkel, E. S., Oweis, G., Vanapalli, S. A., Dowling, D. R., Perlin, M., Solomon, M. J. and Ceccio, S. L., "Friction Drag Reduction of a High Reynolds Number Turbulent Boundary Layer with Wall Injected Polymer Solutions," *Journal of Fluid Mechanics*, (submitted) (2008)

Other details of this work have been published in the following manuscripts:

- Vanapalli, S. A., Ceccio, S. L., and Solomon, M. J., "Universal scaling for polymer chain scission in turbulence," *Proc. National Academy of Science*, Vol. 103, No. 45, pp 16660-16665 (2006)

- Winkel, E. S., Elbing, B. R., Dowling, D. R., Ceccio, S. L., and Perlin, M. "High-Reynolds-Number Turbulent-Boundary-Layer Surface Pressure Fluctuations with Bubble or Polymer Additives," *Proc. of 2005 ASME I.M.E.C.E*, Orlando, (2005).

- Garwood, G. C., Winkel, E. S., Vanapalli, S., Elbing, B., Walker, D. T., Ceccio, S. L., Perlin, M., Solomon, M. J., "Drag Reduction by a Homogenous Polymer Solution in Large Diameter, High Shear Pipe Flow," *Proc. of 2nd Int. Symp. on Seawater Drag Reduction*, Busan, Korea (2005)

- Almeida, T. G., Walker, D. T., Leighton, R. I., Alajbegovic, A., Pankajakshan, R., Taylor, L. K., Whitfield, D. L., and Ceccio, S. L., "A Reynolds Averaged Model for the Prediction of Friction Drag Reduction by Polymer Additives," *Proc. 26th Symposium on Naval Hydrodynamics*, Rome, (2006)

Micro-bubble Drag Reduction: The injection of micro-bubbles into the TBL was examined over large size scales and high Reynolds numbers. In the first part of the DARPA FDR program, we examined MBDR and found that injection of gas would lead to large, local reductions of friction drag. But, the downstream persistence of the FDR was limited. It was hypothesized that the reason for the loss of drag reduction was due to the stratification of the bubbles away from the near-wall region. This result was reported in the following manuscript:

- Sanders, W. C., Winkel, E. S., Dowling, D. R., Perlin, M., and Ceccio, S. L. "Bubble Friction Drag Reduction in a High Reynolds Number Flat Plate Turbulent Boundary Layer," *Journal of Fluid Mechanics*, Vol. 552, pp 353-380 (2006)

- Kunz, R. F., Gibeling, H. J., Maxey, M. R., Tryggvason, G., Fontaine, A. A., Petrie, H. L., and Ceccio, S. L., "Validation of Two-Fluid Eulerian CFD Modeling for Microbubble Drag Reduction across a Wide Range of Reynolds Numbers," *Journal of Fluids Engineering*, Vol. 129, No. 1, pp 66-79 (2007)

In this phase of the FDR program, these experiments were repeated to determine the influence of surfactants and injector geometry. Moreover, optical and electrical impedance measurements were conducted to specifically examine the near-wall void fraction. These data confirmed that a region largely devoid of bubbles (a "liquid layer") formed near the surface of the model when the friction drag reduction was lost. Also, it was found that the presence of surfactants, while leading to a reduction in the average bubble size, did not significantly alter the observed drag reduction. In addition changes in the gas injection method had little effect.

Appendix C presents detailed results from our MBDR effort. This work has been submitted for publication in the *Journal of Fluid Mechanics*:

- Belbing, B. R., Winkel, E. S., Lay, K. A., Ceccio, S. L., Dowling, D. R., and Perlin, M., "Bubble-Induced Skin-friction Drag Reduction and the Abrupt Transition to Air-layer Drag Reduction," *Journal of Fluid Mechanics*, (submitted) (2008)

Other details of this work have been published in the following manuscripts:

- Winkel, E. S., Elbing, B. R., Ceccio, S. L., Perlin, M., Dowling, D. R., "High-Reynolds-number turbulent-boundary-layer wall pressure fluctuations with skin friction reduction by gas injection," *Journal of the Acoustical Society of America*, (in press) (2008)

Air Layer Drag Reduction: If enough air is injected into the TBL, the gas can coalesce into a layer under the influence of buoyancy. This was observed in the first round of MBDR testing at lower speeds, where the friction drag was reduced by over 80% over the full stream-wise extent of the test model. In the follow-on experiments, we observed this Air Layer Drag Reduction at higher speeds, with increased gas flux. The critical gas flux and dynamics of the air layers were examined for flow over the smooth HIPLATE.

Appendix C presents detailed results from our ALDR effort. This work has been submitted for publication in the *Journal of Fluid Mechanics*:

- Belbing, B. R., Winkel, E. S., Lay, K. A., Ceccio, S. L., Dowling, D. R., and Perlin, M., "Bubble-Induced Skin-friction Drag Reduction and the Abrupt Transition to Air-layer Drag Reduction," *Journal of Fluid Mechanics*, (submitted) (2008)

Conclusions: The UM FDR effort helped reveal the underlying physical process responsible for the development and loss of friction drag reduction with the injection of polymer solutions and gas into a high Reynolds number TBL. At the conclusion of our study, we have come to the conclusion that all three drag reduction methods can lead to significant, local reductions in friction drag. However, only ALDR and PDR remained as methods that could lead to persistent reduction of friction drag over large stream-wise extents on our test model. We continue to perform cost-benefit analysis of both ALDR and PDR. Our analysis of PDR has led us to conclude that it is not cost effective, given the necessary flux of polymer, the rate of polymer mixing, and the relative cost of polymer compared to typical fuel costs. Our analysis of ALDR has led us to conclude that ALDR may be cost effective if the gas is not pumped into a prohibitively large back-pressure, and if the air layers can made to persist for longer distances than observed on our present test model.

Appendix A:

Smooth-Flat-Plate Turbulent Boundary Layer Measurements at High Reynolds Number

Ghanem F. Oweis[1&], Eric S. Winkel[1], James M. Cutbrith[2$], Steven L. Ceccio[1], Marc Perlin[3],
and David R. Dowling[1]

[1]Department of Mechanical Engineering
[3]Department of Naval Architecture and Marine Engineering
University of Michigan
Ann Arbor, MI 48109

[2]Naval Surface Warfare Center-Carderock Division
W. B. Morgan Large Cavitation Channel
2700 Channel Avenue
Memphis, TN 38113

Abstract

The characteristics of smooth-flat-plate turbulent boundary layers and their dependence on Reynolds number have been studied for nearly a century. However, there is a relative dearth of measurements at Reynolds numbers typical of full-scale marine and aerospace transportation systems ($Re_\theta = U_e\theta/\nu > 10^5$, where U_e is the exterior or free stream flow speed, θ is the momentum thickness of the boundary layer, and ν is the kinematic viscosity of the fluid). This paper presents the results of a new experimental study of the boundary layer that forms on a flat plate for Re_θ up to and exceeding 150,000. The experiments were conducted in the William B. Morgan Large Cavitation Channel (LCC) at nominal water flow speeds from 3 to 20 m/s on a flat-plate test model 12.9 m long and 3.05 m wide. The model's test surface was polished to $k/l_\nu = k^+ < 0.2$, where k is the root-mean-square roughness height of the surface, $l_\nu = \nu\sqrt{\rho/\tau_w}$ is the usual viscous wall unit, ρ is the fluid density, and τ_w is the wall shear stress. The flow closely approached the zero pressure gradient condition; side-wall and model-surface boundary-layer growth in the LCC's test section caused a streamwise flow speed increase of ~2.5% over the 11-m-long test surface. The overall data set is uniquely complete for an experimental investigation in this Reynolds number range. Direct measurements of static pressure and wall shear stress vs. downstream distance were obtained with pressure taps and floating-plate skin-friction force balances. Composite wall-normal profiles of the mean velocity and second-order turbulence statistics were measured with conventional two-component laser-Doppler velocimetry and a unique near-wall implementation of particle-tracking velocimetry. The resulting flow profiles span the wall-normal

---

[&]Currently at The American University in Beirut, Lebanon.

[$] Currently at Mainstream Engineering Corporation, Rockledge, FL coordinate (y) range from $y^+ = y/l_v$ below unity to $y > \delta_{99}$, where δ_{99} is the wall-normal location where 99% of the free-stream flow speed is achieved. Internal consistency checks within the data set show that τ_w determined from the force balances, the PTV-measured mean wall-gradient of streamwise velocity, and the sum of the LDV-measured mean viscous and Reynolds-shear stresses, all agree within experimental uncertainty. This data set provides a unique opportunity for evaluating boundary layer scaling laws.

1.0 Introduction

Turbulent boundary layers are ubiquitous in both natural and human-engineered fluid flows. They commonly set heat and mass transfer rates in the ocean and atmosphere, and are often a critical factor in determining the efficiency and performance of transportation systems. The simplest possible boundary layer forms where a uniform unidirectional flow contacts a smooth flat surface. This boundary layer will be turbulent if the Reynolds number of the flow is high enough to sustain turbulence, and an intentional or naturally occurring disturbance has caused transition from laminar to turbulent flow.

Given the importance of the phenomena and the simplicity of the flow geometry, flat-plate turbulent boundary layers (TBLs) have been investigated for the greater part of the last century. Much is known about the mean and fluctuating components of flat plate TBL flow from controlled laboratory-scale investigations conducted at momentum-thickness-based Reynolds numbers $Re_\theta = U_e\theta/\nu < 10^4$, where U_e is the exterior or free stream flow speed, θ is the momentum thickness of the boundary layer, and ν is the kinematic viscosity of the fluid. Additional investigations conducted in the atmospheric boundary layer and in special testing facilities at higher Reynolds numbers – where the investigations cannot be as well controlled or as complete as the laboratory scale studies – have allowed scaling laws developed from the laboratory studies, the governing equations, and dimensional reasoning to be at least partially evaluated at much higher Reynolds numbers. The primary purpose of this manuscript is to report the characteristics of the TBL that develops on a smooth flat plate under well-controlled conditions for $6\times10^3 \le Re_\theta \le 1.5\times10^5$ (or, alternatively in terms of the downstream-distance-based Reynolds number, $3\times10^6 \le Re_x = U_e x/\nu \le 2.2\times10^8$). The experimental results presented here are unique in their completeness in this Reynolds number range.

Although the flat-plate geometry is idealized compared to that of practical aerodynamic and hydrodynamic devices, the structure and scaling of flat-plate TBLs remain important topics because moderate-Reynolds-number results are commonly scaled-up when designing or predicting the performance of fluid dynamic devices that operate at high Reynolds numbers where experimental measurements are sparse or non existent. Furthermore, the numerical values and functional forms used in computational models of wall-bounded turbulence are based on the flow structure and empirical constants (κ and B) determined from TBL studies (see Launder and Spalding 1972, or Pope 2000). Thus, the validity of such models is enhanced when the empirical constants are shown to be valid over as large a Reynolds number range as possible.

In addition, over the last two decades or so, a variety of revisions to the classical understanding of TBL scaling and flow structure have been derived and/or proposed for the mean streamwise velocity profile and the Reynolds stresses. Given that the intent of this manuscript is to dispassionately and concisely report new high-Reynolds-number TBL results, these new experimental data are tabulated in dimensional form in the appendix, and plotted with traditional inner (law of the wall) scaling along with a few simple scaling-law tests. For conciseness and clarity, detailed tests and comparisons involving: *i*) revised scaling laws (George and Castillo 1997, Marusic et al. 1997, DeGraaff and Eaton 2000, Marusic and Kunkel 2003, Lindgren et al. 2004), *ii*) recently proposed revisions to the layer structure of TBLs (Wei et al. 2005, Fife et al. 2005), and *iii*) log-law and power-law scaling of the mean streamwise velocity profile (Österlund et al. 2000a, Barenblatt et al. 2000, Österlund et al. 2000b, Afzal 2001, Panton 2002, Buschmann and Gad-el-Hak 2003), while clearly possible, are beyond the scope of this manuscript.

The experimental results presented here were collected during three multi-month experimental campaigns conducted between the fall of 2001 and the spring of 2005. The experiments involved free stream flow speeds from 3 to 20 m/s, a flat plate test model with a hydraulically-smooth test surface 11 m in length, and the world's largest low-turbulence water tunnel, the US Navy's William B. Morgan Large Cavitation Channel (LCC). Measurements are reported from static pressure taps, average skin friction force balances, two-component laser Doppler velocimetry (LDV), and near-wall particle tracking velocimetry (PTV). In particular, the static pressure measurements show a mild favorable pressure gradient that is consistent with boundary layer growth in the test section of the LCC. But more importantly, the wall shear stress determined from the average skin friction force balances, the LDV Reynolds stress profiles, and measured mean flow in the viscous sublayer all agree, and are consistent with the Von Karman boundary-layer momentum integral equation, to within experimental error.

The published literature on the topic of turbulent boundary layers is extensive. However, review articles (Sreenivasan 1989, Gad-el-Hak and Bandyopadhyay 1994, Fernholz and Findley 1996) and recent texts (Pope 2000, White 2006) provide a starting place for sorting and assimilating this material. The prior studies most relevant to the one reported here fall into two groups: smooth-wall laboratory investigations (Fernholz et al. 1995, Österlund et al. 1999, DeGraaff and Eaton 2000) where Re_θ reaches $\sim 10^4$ (or Re_x reaches $\sim 10^7$) and the rough-wall atmospheric and wind-tunnel-sidewall boundary layer experiments (Saddoughi and Veeravalli 1994, Metzger and Klewicki 2001, and Metzger et al. 2001) conducted at much higher Reynolds numbers. The experimental results from the present study extend the Reynolds number range of the laboratory results to partially close the Reynolds number gap between the two groups of prior studies.

The remainder of this manuscript is organized into four sections. The next section describes the experimental setup, measurement techniques, and data processing methods. The third and fourth sections present the average flow characteristics and turbulence statistics, respectively. This research effort is summarized and conclusions are stated in the final section. The appendix provides tabulations of the experimental data.

2.0 Experimental Techniques

The experiments were conducted in the U. S. Navy's William B. Morgan Large Cavitation Channel (LCC). This closed-circuit water tunnel is the largest facility of its kind in the world (Etter et al. 2005). The LCC's test section has a nominal length of 13 meters and a cross-section of 3.05 m x 3.05 m. The LCC may be operated at steady empty-test-section flow speeds from 0.5 m/s to more than 18 m/s and at absolute test section pressures from 3.4 kPa to 414 kPa. At the flow speeds of these tests, the LCC's test-section centerline turbulence level was 0.2% to 0.4%.

The test model was the same one utilized by Sanders et al. (2006), a flat plate 12.9 m long and 18.4 cm thick that horizontally spanned the LCC test section (see Fig. 1). With these dimensions, test section blockage lead to flow speeds above the developing boundary layer as high as 20.2 m/s. The 17-metric-ton model was composed of three sections fitted together with precision-machined slot-and-key mechanisms that allowed repeatable and seamless assembly. The edges of the model were mated to the test section walls with an inflatable seal to prevent bypass flow between the top and bottom sides of the model. In addition, 45° triangular-wedge fillet edge-fairings (75 mm maximum height and width) were installed at the model-sidewall junction to control and minimize cavitation, and streamwise corner and junction vortices. The leading edge of the model was a 4-to-1 ellipse while the trailing edge was a 15°-full-angle triangular wedge of 0.6-m length that was terminated at 25 mm thickness with 40° bevel angle. This asymmetric trailing edge design was intended to prevent near-wake vortex shedding and its propensity for flow-induced model vibration. The Cartesian coordinate system used throughout this manuscript is shown in Fig. 1; x is zero at the model's leading edge and runs parallel to the flow direction, y is zero on the test surface and increases perpendicular to it (and to the x axis) while z runs in the spanwise direction and completes a right-handed coordinate system.

During testing, surface normal acceleration was measured with six internally mounted Wilcoxin 754-1 accelerometers. When integrated, these signals produced a maximum measured root-mean-square (rms) surface-normal vibration velocity of ~2 mm/s at the highest test speed. This vibration fluctuation level was far smaller than the velocity resolution of the LDV system (see below) and was also well below the rms free stream velocity fluctuation. Thus, model vibration was negligible in these experiments.

A distributed-roughness boundary layer trip was used. Otherwise, the model was hydraulically smooth from its leading edge back to the beginning of the trailing edge wedge. The test surface was 304 stainless steel polished to a nominal surface roughness of 0.4 μm or less. The roughness parameter, $k^+ = k/l_v$, where k is the average roughness height and l_v is the viscous length ($l_v = \nu\sqrt{\tau_w/\rho}$ for kinematic viscosity ν, wall shear stress τ_w, and fluid density ρ), was less than or equal to 0.2 over the entire flat test surface for all flow conditions. The boundary layer was tripped by an intentional spanwise strip of distributed roughness applied to the elliptical portion of the model starting 25 mm from the model's leading edge and extending 250 mm downstream. The distributed roughness was composed of nominally-0.25-mm (100 grit) sand grains embedded in a film of epoxy and spaced randomly 2 to 5 mm apart. The design of this distributed roughness trip was based on guidelines provided by Prof. H. Nagib (private communication).

Static pressure, skin friction, and fluid velocity measurements were made at three primary free stream flow speeds, $U_\infty = 6.65$ m/s, 13.2 m/s, and 19.9 m/s. These values are correct for the center of the test plate; however – as discussed in the next section – U_e varied from ~1% lower (upstream) to ~1% higher (downstream) over the plate's streamwise extent. In addition, a subset of the flow measurements were made at $U_\infty = 3.3$ m/s.

Static pressure, $P(x)$, was measured at 11 downstream (x) locations with a Rosemount 3051P transducer and 1.6-mm-diameter taps located 48.3 cm above the plate on the sidewalls of the LCC test section. Calibration of the Rosemount transducer was performed using a Druck DP601 pressure source and a Paroscientific DigiQuartz Model 740 pressure transducer. The static pressure measurements were corrected for zero-bias (or drift) error via no-flow pressure measurements performed before and after TBL data acquisition. In the next section, these static pressure measurements are reported in terms of the pressure coefficient, $C_P(x) = \left(P(x) - P_1\right)/\frac{1}{2}\rho U_\infty^2$ where P_1 in the pressure measured at the first tap at $x = 1.96$ m and U_e is the free stream flow speed over the center of the test plate. Test-section side-wall and model-surface boundary-layer growth caused $U_e(x)$ to increase by ~2.5% between the first and last pressure taps. At the flow speeds of these tests, hole error (see Benedict 1984) was the dominant source of uncertainty, leading to an overall uncertainty of ±0.0005 in pressure coefficient units.

Average skin friction, $\tau_w(x)$, on the test surface was measured with six floating-element strain-gage force balances located at ~1/3 span and at $x = 1.96$ m, 3.41 m, 5.94 m, 7.43 m, 9.23 m, and 10.68 m. The round sensitive surfaces of these balances had a diameter of 15.24 cm (6 inches) were adjusted to be flush with test surface of the model. The gap around the circumference of the sensing surface had a maximum value of ~75 μm. This gap was checked for uniformity (and minimum clearance) using a 51 μm (0.002 inch) stainless steel shim. At the highest flow speeds, l^+ is approximately 1.7 microns in these experiments, so the worst-case average and maximum surface gaps were $30\,l^+$ and $44\,l^+$ respectively.

Strain gauge amplifiers (Vishay 2310) were employed for excitation, nulling, and amplification of the skin friction signals. Data were collected at a rate of 50 Hz for variable lengths of time, but measured skin friction forces were primarily determined from 10-second averages. The force balances were individually calibrated at least once per test day using a suction cup attached via a metal cord to a second precision load cell (Omega LCEB-5) that was mounted on a finely-adjustable translation stage. Calibration measurements were made by temporarily fixing the base of the translation stage and then adjusting the tension in the metal cord with horizontal movement of the precision load cell to produce known and repeatable horizontal loads on each force balance. A linear fit to the calibration data was used to convert the measured voltage signals to friction force; the root-mean-square deviation of the calibration points from a linear fit corresponded to at most ±0.02 N. In the next section, these static pressure measurements are reported in terms of the skin friction coefficient, $C_f(x) = \tau_w(x) / \frac{1}{2}\rho U_e^2(x)$.

For the skin friction measurements, the significant sources of uncertainty include drift and calibration errors. As is common for strain gauge equipment, the force-balance outputs tended to drift mildly over periods of several hours. Thus, the strain-gage bridges were nulled during a no-flow condition every one or two hours during a test day. The error associated with drift was approximately ±0.05 N. To account for drift, the average of at least 12 independent 10-second measurements is reported and the drift uncertainty, σ_{drift}, is taken to be twice the standard deviation of the mean of these 12+ measurements. The uncertainty associated with calibration, σ_{cal}, was taken to be twice the standard deviation of the mean of multiple calibrations (typically 1 to 2%) taken over a period of several days or more. The combined experimental uncertainty, $\sigma = \sqrt{\sigma_{drift}^2 + \sigma_{cal}^2}$, varied somewhat between force balances, but were generally less than ±3% of the final skin friction measurement from any force balance.

Fluid velocity measurements were made with two LDV systems. The first, a single component system, was fixed in place and used to monitor the test-section-inlet streamwise velocity at $x = -6.2$ cm and $y = 14.1$ cm. It operated with a 2.775x beam expander, 115 mm beam spacing, and 88 cm focal length. The second, a two component system, was mounted on a vertical traverse and used for measuring the mean velocity

(U,V) and the second-order statistics of the velocity fluctuations (u',v') in pairs of vertical columns (0.1 mm < y < 300 mm) near x = 5.9 m and 10.7 m. This two-component system consisted of Dantec BSA 57N11 signal processors, fiber optic probes, Spectra Physics 6 Watt Argon-Ion lasers (model 2017), Dantec three-dimensional traverse, and Dantec Flow software. This system was operated at 514.5 nm and 488 nm wavelengths with a 1.5x beam expander, 112 mm beam spacing, and 1,600 mm focal length. The burst-processor parameters included transit-time weighted averages for velocity bias correction, low and high-pass filtering dependent on free stream velocity, and particle size rejection for the elimination of erroneous measurements from reflections off the polished surface. The y-coordinate origin for the second LDV was determined within ±0.1 mm by measuring the near wall fluid velocity with the LDV beams above, touching, and reflecting from the model's working surface, and setting y = 0 at the location of minimum average streamwise velocity.

For the LDV measurements, the water channel was flood-seeded with silicon carbide particles with a nominal diameter of 3 microns. The downstream LDV had a prolate focal volume with a diameter of 170 μm and a length of 6.5 mm that was oriented with its long axis perpendicular to the flow direction but nearly parallel to the plate surface. To make measurements near the test surface, the downstream LDV optical head was tilted 2.2°; this increased the projected vertical dimension of the downstream LDV focal volume to 250 μm. This increase in the focal-volume vertical dimension becomes a dominant factor near the wall. Here, the larger dimension translates to an increased range of instantaneous velocity measurements due to the steep gradient of the velocity profile near the wall and this can lead to elevated $\overline{u'^2}$ values (the overbar denotes a time or ensemble average). In addition, the LDV-head tilt lead to non-normal optical transmission at the vertical LCC sidewall windows. The resulting optical distortion and reduction in coincident bursts limited the LDV focal volume's distance from the LCC sidewall to 0.65 m. However, this spanwise location is well beyond the furthest influence of the model-side-wall-junction flow (~0.20 m from the LCC sidewall).

Both LDV systems were calibrated with a spinning disk covered with 60-grit emery paper that was driven by a CompuMotor Model SM233BE-NTQN and CompuMotor TQ10X Servo-Controller. The major contributor to the uncertainty of the calibration is the ±0.4 rps accuracy of the motor as listed by its manufacturer. The scatter of this LDV calibration data about a linear fit was less than ±0.005 m/s. The overall velocity uncertainty was ±0.025 m/s at the 95% confidence level (Park et al. 2003).

The measurements reported here are primarily drawn from the third phase of experiments where 10,000 LDV bursts were collected at two pairs of measurement locations at the three primary flow speeds (6.65, 13.2, and 19.9 m/s). The burst processors gain and photomultiplier tube (PMT) voltage were adjusted for each measurement location so that the burst rate remained relatively constant with respect to the distance from the plate for each free stream velocity. The coincident burst rates varied from 100 Hz at 6.65 m/s to 170 Hz at 19.9 m/s. The coincidence window varied from 0.02 ms at 6.65 m/s to 0.01 ms at 19.9 m/s, roughly translating to the ratio of probe volume diameter to free stream velocity. Table 1 provides a listing of flow parameters at the downstream (x) locations of the LDV profiles were measured. The minor differences between free stream speeds at the nearby LDV measurement locations arise from the finite precision of the downstream LDV system and the repeatability of the LCC flow speed on different days. In the next section, LDV results are provided for the average streamwise velocity, U, the streamwise and wall-normal velocity variances, $\overline{u'^2}$ and $\overline{v'^2}$, and the Reynolds shear stress, $-\overline{u'v'}$. The water temperature varied between 18 and 24 °C during these tests; its average was 21.2°C. The density (ρ), and dynamic (μ) and kinematic (ν) viscosities of water at this temperature are $\rho = 998$ km^{-3}, $\mu = 0.993\text{x}10^{-3}$ kgm^{-1}s^{-1}, and $\nu = 9.95\text{x}10^{-7}$ m^{2}s^{-1}.

Unfortunately, the size of the two-component LDV focal volume prevented its use for near-wall velocimetry measurements (i.e. for $y^+ = y/l_v$ less than 100 or so). Thus, to complete the flow profile measurements, three custom-designed near-wall particle-tracking-velocimetry (PTV) systems were assembled in water-tight boxes and built into the test model at x = 1.96 m, 5.94 m, and 10.68 m. The three PTV systems had the same design, though there were slight variations among the three systems during actual implementation. A design schematic for one of these systems is shown in Fig. 2 delineating the illuminating laser source, visualization camera, and optical pathways. Here, the near-wall flow was imaged through a periscope prism that protruded into the flow. The imaged region was preferentially (anisotropically) magnified in the wall-normal direction a using a cylindrical lens combination that produced a 2-mm-vertical field of view. The geometrical and hydrodynamic design choices of the prism were modeled after the periscope-mirror LDV work of Compton and Eaton (1996, 1997). An advantage of imaging through this prism design, in addition to eliminating the need for large focal length optics, was the formation of a reflection of the PTV particle images from the polished test surface that could be used to accurately locate the wall in the PTV images. The three dual-cavity, double-pulsed Nd-YAG lasers (Big Sky 120 mJ, New Wave Solo 200 mJ, and New Wave Solo 50 mJ) were tightly bolted to the exterior side of the LCC to minimize relative motion between the lasers and the illumination-path optics. Each laser's green beam (532 nm) was relayed from the exterior of the tunnel through a straight 40-mm-diameter water-tight conduit to the sheet-making optics in the test-model-interior water-tight box and then reflected into the flow via a 45° laser mirror to form a light sheet lying in constant-z planes having a thickness of 75 ± 25 μm. The sheet thickness was measured directly by passing the beam at the measurement location through the objective lens of a graded microscope and expanded upon exiting from the eyepiece onto a white screen. Titanium dioxide seed particles with a nominal size of 1 μm and specific gravity 4.26 from J.T. Baker Industries were flood seeded in the LCC water to scatter the laser light. Adding seven to ten kg of TiO_2 powder to unseeded tunnel water resulted in roughly 5 particles in a 32 pixel by 32 pixel region of the image. For each PTV system, the receiving optical train began with a periscope prism that collected the particle-scattered laser light and directed it towards the recording camera with the aid of an additional 75-mm-diameter mirror. Converging (focal length = +75 mm) and diverging (focal length = –300 mm) cylindrical lenses were placed in front of the cross-correlation CCD camera to provide a nominal 1-to-3 stretching of the camera's field of view in the vertical direction to increase the sensitivity of the PTV systems to vertical velocity fluctuations. The PTV camera was fitted with a Nikon 105 mm/f2.8 micro-Nikkor lens attached to two Nikon TC-201 teleconverters (2X each). Spatial calibration of the resulting images was made possible through imaging of a precision test target placed in the PTV interrogation plane that was composed of a square array of 20 μm round dots with center-to-center spacing of 50±0.02 μm. For the systems at x = 1.96 and

5.94, the resolution of the cross-correlation CCD cameras was 1200 by 1600 pixels (LaVision Imager Pro), while that at x = 10.68 was 1024 by 1280 pixels (LaVision FlowMaster CCD camera); in all cases the cameras were oriented to utilize their higher resolution in the wall-normal direction. The final x,y-frame-sizes were 5.03 mm by 2.7 mm at x = 1.96 m, 4.88 mm by 1.97 mm at x = 5.94 m, and 4.78 mm by 2.01 mm at x = 10.68 mm. Thus, each camera pixel nominally corresponded to a rectangle 4.4 μm in the x-direction and 1.5 μm in the y-direction so that a single particle's image was typically an ellipse covering an area of 5 pixels by 13 pixels. The lasers, cameras, and data recording were controlled by PC-type computers running DaVis 7.1 software by LaVision Inc. For the range of investigated free stream speeds, the time separation between laser pulses, Δt, varied from 5.5 μs to 35 μs with accuracy better than 50 ns so that average particle displacements were typically 12 to 16 pixels in the mean flow direction. Although dual-frame acquisition rates from 4 to 12 per second were achieved, the image sizes and flow speeds ensured that any frame pair was temporally uncorrelated from the preceding or following pair. At each flow condition 3500 image pairs were recorded, and the vectors extracted.

The PTV processing was conducted as a series of steps that converted elongated (elliptical) particle images to velocity field averages and variances. The processing began by using the reflection from the test surface to determine the wall location within each instantaneous PTV image with an accuracy of better than ± 1 pixel. This was done via a two-dimensional cross correlation computation between the imaged particles and their reflection pattern. This step was followed by identifying and accurately locating the x,y-pixel-location centroid of individual particle images to better than ±0.1 pixel with a two-dimensional spatial matched-filter search of each image frame. Fortunately, particles very near the wall typically produced images that merely overlapped the wall location and particle-image centers could be reliably located within a pixel or two of the wall. Thus, the overall resolution of the PTV processing scheme was more than an order of magnitude better than the 5-pixel-by-13-pixel average particle-image size for particles with image centers more than one pixel above the wall. The matched-filter-determined particle-image-center locations were converted back to physical x,y-coordinates using the information from the calibration image.

The primary challenge in PTV is to correctly identify the image from the same particle in both frames. Here, this task was accomplished by selecting a particle image in the first frame and then searching a spatial window in the second illumination frame where this particle's second image was expected to appear. If no particles were found in the second-frame search window, that particle was discarded. If one or more particle images were found in the second-frame search window, then two concurrent tests were conducted to determine the highest probability match. First, a two-dimensional cross correlation value was computed between the particle intensity distribution in the first frame and all possible particle images in the second frame. The correlation window was 24 pixels x 24 pixels centered at the particle images' centroidal pixels. The second-frame image with the highest cross-correlation value was most likely to be the correct match to the first-frame particle. The second test involved checking whether the highest computed correlation value was an actual correlation peak, by repeating the correlation calculation eight times corresponding to eight different shifts of the first 24^2-pixel box around the second-frame particle image centroid. If the correlation value at zero shift was the highest, then the image was considered the correct match for the particle in the first frame. The local particle velocity (u,v) was then simply determined from the particle's centroid displacement divided by time between frames, Δt. The data processing then moved to the next first-frame particle image and the above process was repeated for all possible first-frame particles. At the end of this process, each frame pair produced an instantaneous velocity field that was randomly sampled in space.

Next, a vector post-processing filter was passed over each instantaneous field to eliminate spurious vectors. The filter compared the vertical and horizontal components of the vector under consideration with the mean and root mean square components of all the vectors within a radius of 80 pixels. For the measurements at x = 1.96 m and 10.68 m, the spurious vector percentage ranged between 4% and 7%. At x = 5.94 m, the spurious vector percentage was higher, 10% to 15%, because of non-smooth particle images possibly caused by optical distortion. These instantaneous velocity field results were then collapsed in the streamwise direction and across all frame pairs from the same experimental run by sorting the instantaneous velocity vectors into vertical bins. Small bins were chosen close to the wall (ranging in size from 1.5 to 4 pixels depending on the flow speed) to resolve the near wall flow, while far away from the wall $y^+ > 50$, larger bins of 16 pixels were used. Once compiled, there were typically 10 thousand vector samples in the small bins nearest the wall, and 50 thousand vector samples in the larger bins farther from the wall. Averages and variances for each bin were computed directly from the vector samples in that bin and reported at the bin-center vertical location.

For PTV to be successful, the second-frame search window size and shape needs to be optimized. When the second-frame search window is too small or poorly placed, correct second-frame particle images are less likely to be found and potentially useful flow information is lost. However, when the second-frame search window is too large, the likelihood of two or more ambiguous second frame images increases, and the probability of including spurious vectors increases. In both cases, averages and variances may be statistically under-resolved or even biased by a poor choice of the second-frame search window. For the PTV results presented here, the shape of second-frame window is a based on a power law of the form $(y - y_o)/Y = \pm((x - x_o)/X)^{1/6}$ where (x_o, y_o) is the first-frame particle-image-centroid coordinate, distances are measured in pixel units, and $0 \leq x - x_o \leq X$ and $|y - y_o| \leq Y$. Figure 3a) shows this search-window shape. The size of the search envelope was allowed to vary with wall-normal distance to account for the strong velocity gradient of the flow. Near the wall, $y^+ < 15$, the values of X and Y increased linearly and quadratically with y, respectively; according to $X = a_1 + a_2 y(\tau_w/\mu)\Delta t$ and $Y = a_3 + a_4 y^2(\tau_w/\mu)\Delta t$, where the a's are empirical constants: a_1 and a_3 have units of pixels, a_2 is unitless, and a_4 has the units of inverse pixels. The other parameters (τ_w, μ, and Δt) have SI units and, in the near-wall region, the grouping of parameters, $y(\tau_w/\mu)\Delta t \cong y(\partial U/\partial y)\Delta t \cong U\Delta t$, represents the average downstream particle displacement in the time interval Δt. A slight distance above the wall ($y^+ \sim 15$) X and Y reach constant values of X_{max} (= 23 pixels) and Y_{max} (= 13 pixels), respectively. These maximum values were determined to ensure that $X \geq \left(U + 3\sqrt{\overline{u'^2}}\right)\Delta t$ and $Y \geq \left(V + 3\sqrt{\overline{v'^2}}\right)\Delta t$ throughout the measurement domain. Here, $a_1 = X$ and $a_3 = Y$ at the wall ($y = 0$). The factor a_2 controls how fast the envelope's streamwise extent grows with increasing y (optimal: 0.50 to 0.56); and a_4 controls how fast the envelope's vertical extent grows with increasing y (optimal: 0.006 to 0.009). Figure 3b) shows how X and Y were varied for increasing y^+.

Figure 4 illustrates the PTV processing method. Figure 4a) shows first-frame particle images, with the matched-filter-identified particle images marked at their centroids. The diagonal extent of the particle images is a remnant of minor misalignment in the PTV-system collection optics. Figure 4b) shows the identified first-frame particles centroids from Fig. 4a) along with the search window where second frame particles are expected to be found. The identified second-frame particles are also shown. The choice of the search window parameters for this case ($a_1 = 1.5$ pixel, $a_2 = 0.50$, $a_3 = 1.25$ pixel, $a_4 = 0.0075$ pixel^{-1}) places second-frame particles well inside the search envelope. Some of the first-frame particles have no matching second frame particles and vice versa because spanwise particle motion may remove particles from the laser sheet between laser pulses, and thresholding of the matched-filter output causes some weak particle images to be discarded. For the PTV results reported here, the typical selection of the a's was the same as above for a_1, a_2 and a_3, with $a_4 = 0.006$ pixel^{-1}.

To assess the sensitivity of the PTV measurements to the a's, a case study is presented in Fig. 5, where six different search parameter variations are used determine the profiles of $\overline{u'^2}$ and $\overline{v'^2}$, the turbulence quantities found to be most sensitive to choice of the a's. The factor a_2 that controls how fast the window's streamwise extent grows with vertical distance is varied from a value of 0.41 (×) to 0.66 (o); and a_4 that controls how fast the window's vertical extent grows is varied from a value of 0.0045 (+) to 0.012 (o). When the a's are significantly smaller than the typical values specified above, some of the particle-image data can be filtered out resulting in lowered turbulence quantities (+, ×), and the opposite is true (o) due to an increased probability of the occurrence of outliers with oversized envelopes. For the other three cases (*, ∇, •) [$0.50 \leq a_2 \leq 0.56$; $0.0075 \leq a_4 \leq 0.012$] the measured structure of the boundary layer is nearly insensitive to the processing parameters. Overall, for these six cases that cover a wide variation in search parameters, the processing-parameter-induced changes in the measured profiles are mild and are of the same size as the experimental uncertainty. Thus, the dependence of the PTV measurements on the PTV processing parameters was not considered significant, and all PTV results presented are determined from the typical a-values.

3.0 Average Flow Results ***(plot composite PTV-LDV profiles where possible)***

3.1 Static Pressure

The dependence of the average static pressure in the LCC test section on the streamwise coordinate x is shown in Fig. 5 in terms of the pressure coefficient, $C_P(x)$. Downstream of the test model's elliptical leading edge, the tunnel and test-model hardware cross sections were geometrically constant for more 11 m. Thus, boundary layer growth on the test model and the LCC-test-section sidewalls is the primary cause of the slightly favorable pressure gradient that is observed at all three primary test speeds.

Although easily measured and non-zero, the observed pressure gradient is small enough so the measured boundary layer characteristics should approach those of a truly zero pressure gradient flow. At the three primary test speeds, the acceleration parameter, $K=\left(\nu/U_e^2\right)\left(dU_e/dx\right)$, is less than 10^{-9}; a substantial deviation from the classical log-law only occurs for $K>1.6\times10^{-6}$ (Patel 1965). Furthermore, when the Reynolds-averaged streamwise boundary layer equation is rendered dimensionless, the near-wall region where the momentum flux terms are small ($y^+ \lesssim 30$) will not be influenced by a streamwise pressure gradient when $\Lambda y^+ << 1$ where $\Lambda=\left(\nu/\rho u^{*3}\right)\left(dP/dx\right)$ and $u^*=\sqrt{\tau_w/\rho}$ (see Afzal, 2001). For these experiments, Λ was of order 10^{-5} or smaller. Similar considerations suggest that the outer region where the viscous stress is small ($y^+ \gtrsim 100$) will not be influenced by the streamwise pressure gradient when $\Omega=\left(\delta_{99}/\tau_w\right)\left(dP/dx\right)<<1$. However, in these experiments, Ω ranged from 0.1 to 0.2, so some differences are expected between the measured outer layer flow and a truly zero-pressure-gradient TBL at the same Reynolds number.

3.2 Average Skin Friction

The variation of the time-average skin friction on the test surface is shown in Fig. 6 in terms of the skin friction coefficient, C_f, and the downstream-distance-based Reynolds number, $Re_x = U_e x/\nu$, calculated from the local value of U_e. Results from 1.96 m $\leq x \leq$ 10.68 m, and U_e = 3.3, 6.65, 13.2, and 19.9 m/s are plotted on this figure with error bars representing the 95% confidence interval. Three separate techniques were used to determine C_f and these are represented by different symbols in Fig. 6. The *open* symbols (○, □, △) signify direct measurements of τ_w made with the force balances. The *closed* symbols (●, ■, ▲) represent measurements of $\tau_w = \mu(\partial U/\partial y)_{y=0}$ determined from the near-wall PTV measurements of $U(y)$ via a linear least-square fit for $0.5 \lesssim y^+ \lesssim 5.5$ using $U = 0$ at $y = 0$, and the *line-only* symbols (+, ×, ∨) symbols represent measurements of the total stress $\tau_w \approx \mu(\partial U/\partial y) - \rho\overline{u'v'}$ as determined from the LDV measurements in the TBL's constant-stress region, $100 \lesssim y^+ \lesssim 2000$. The solid line is a simple least-squares power-law fit to the force-balance measurements.

As is readily apparent, the three separate techniques for determining τ_w all agree to within experimental accuracy and they are all well represented by the power law fit,

$$C_f = (0.0170 \pm 0.0004) \cdot Re_x^{-(0.1237 \pm 0.0067)}. \tag{3.1}$$

Here it must be noted that the empirical constants in this law may implicitly include the influence of flow artifacts arising from the boundary layer trip and the test model's elliptical leading edge. Yet, such influences should be small. Together the distributed roughness trip and curved portion of the test model's leading edge occupy the first 0.37 m of the test model, only 3.5% of the wetted length (10.68 m) of the experiment. Given the moderate scatter in the measurements and the relative success of the power law fit, the values of C_f (and τ_w) used for all subsequent evaluations and normalizations are determined from Eq (3.1).

3.3 Average Streamwise Velocity Profile

- completeness of measurements; from 0.1 ≤ y+ ≤ 10^5
  - linear, log-law, and wake regions – overlap between instruments
  - good near-wall measurements
  - as much as 2-decades of y+ in the classical "log-law" region

- fitted values of “kappa” and “B” across all the current data are ___±__ and ___±__ and these are in good agreement with prior values for TBLs
- wake component results are consistent with that of prior experiments
    - values for the wake parameter are “close”
    - current values are likely lower because of mild acceleration of the flow
- log-law vs. power-law checks are uncertain, but the current data when analyzed via fractional differences suggests that the log-law is a better fit over the chosen range of y.

3.4 Discrete Evaluation of the Von Karman Boundary Layer Integral Equation

As a final overall check of the LDV measurements, the skin friction on the plate midway between the middle and downstream measurement stations was estimated from a discrete evaluation of the Von Karman boundary layer integral equation,

$$\left(\frac{\tau_w}{\rho}\right)_{x=\bar{x}} \approx \frac{\left(U_2^2\theta_2 - U_1^2\theta_1\right)}{\Delta x} + \frac{\left(\delta_2^* U_2 + \delta_1^* U_1\right)}{2}\frac{\left(U_2 - U_1\right)}{\Delta x}\,, \tag{3.2}$$

where $\bar{x} = (x_1 + x_2)/2$ = 8.31 m, $\Delta x = x_2 - x_1$ = 4.74 m, and the subscripts 1 and 2 refer to average conditions at x_1 = 5.94 m and x_2 = 10.68 m, respectively. The momentum (θ) and displacement (δ^*) thicknesses were calculated from discrete evaluations of their usual definitions, $\theta = \int_o^h (U/U_e)(1 - U/U_e)dy$ and $\delta^* = \int_o^h (1 - U/U_e)dy$, with: i) $U = 0$ at $y = 0$, *ii*) h defined to be the vertical location from the test surface where the LDV-measured Reynolds shear stress dropped to the free-stream background noise level, and *iii*) U_e defined to be the average of U for first three measurement points above $y = h$. Individual values of θ and δ^* are given in Table 1. For evaluation of Eq. (3.2), the values of U_1 were drawn directly from the LDV measurements, while the values of U_2 were consistent with the LDV results but were slightly corrected (a 0 to 0.8% velocity increase) to match the measured C_P drop between x_1 and x_2. Here, the momentum thickness difference in the first term on the right side of Eq. (3.2) provides the dominant contribution because U_1 and U_2 differ by only a percent or so.

The results of this estimation exercise showed that, at the three primary test speeds, the inferred skin friction results from Eq. (3.2) were 35%, 31%, and 32% lower than the power-law fit to the direct skin friction measurements provided by Eq. (3.1). The consistency of the mismatch across test speeds suggests that the mismatch was caused by a bias problem rather than random error. The most likely source for such a bias error is the unintentional optical distortion in the LDV windows used at $x = 5.94$ m and $x = 10.68$ m. Such optical distortion leads to minor variations in the LDV beam foci location and beam-crossing angle, and can cause spatially-varying bias error in LDV average velocities of approximately ±0.5% to ±1%. While such bias errors may be negligible for assessing profile shapes, they can have an order of magnitude greater influence (±5% to ± 10%) on θ (and δ^*). And, when θ (and δ^*) are assigned such uncertainties, the range of possible skin friction values from Eq. (3.2) overlaps the Eq. (3.1) results. Thus, the inferred-vs.-measured skin-friction mismatch was concluded to result from the optical imperfections in the LDV windows, experimental artifacts that (regrettably) were not avoided.

4.0 Second-order Turbulence Statistics (plot composite PTV-LDV profiles where possible)

- $\overline{u'^2}$

    inner variable collapse is imperfect – higher peak $\overline{u'^2}$ as Re increases

    $\overline{u'^2}$ at specific points does follow prior proposed scaling laws

    D&E's mixed scaling of $\overline{u'^2}$ appears superior to inner variable scaling

- $\overline{v'^2}$

    inner variable collapse is OK?

    imperfect overlap between

- $-\overline{u'v'}$ + total TBL stress

    shear stress collapses well for the inner layers?

    total stress is consistent with the force-balance shear stress

5.0 Summary and Conclusions

- Unique High Re Data Set – precisely the type of info that should be archived!
- (possibly the last exp. of this type for sometime to come)
- largest possible flat plate model that would fit in the worlds largest water tunnel
- Results fall between prior controlled lab tests and other High RE experiments
- Well-controlled experiment
- low-turbulence water tunnel, small variation in speed & temp.
- polished flat test surface
- four instruments providing measurements that are consistent within error
- (force balances, static pressure, LDV, PTV).
- Tabulated results for the community to use
- the present preliminary analysis suggests the log-law to be better than a power law
- $\overline{u'^2}$ increases according to the proposed scaling relationships
- other turbulence quantities are "well behaved"

References

Barenblatt, G.I., Chorin, A.J., and Prostokishin, V.M. (2000) "A note on the intermediate region in turbulent boundary layers," *Physics of Fluids* Vol. 12, 2159-2161.

Benedict, R.P. (1984) *Fundamentals of Pressure, Temperature, and Flow Measurements* (Wiley New York), pp. 340-349.

Buschmann, M.H., and Gad-el-Hak, M. (2003) "Debate concerning the mean-velocity profile of a turbulent boundary layer," *AIAA Journal* Vol. 41, 565-572.

Compton D.A., and Eaton J.K. (1996) "A high resolution laser Doppler anemometer for three dimensional turbulent boundary layers," *Experiments in Fluids*, **22**, 111-117

Compton D.A., and Eaton J.K. (1997) " Near-wall measurements in a three-dimensional turbulent boundary layer," *J. Fluid Mech.*, **350**, 189-208.

DeGraaff, D.B., and Eaton J.K. (2000) "Reynolds-number scaling of the flat-plate turbulent boundary layer," *J. Fluid Mech.* Vol. 422, 319-346.

Etter, R.J., Cutbirth, J.M., Ceccio, S.L., Dowling, D.R., and Perlin, M. (2005) "High Reynolds number experimentation in the U. S. Navy's William B. Morgan Large Cavitation Channel," *Measurement Science and Technology*, Vol. 16, 1701-1709.

Fernholtz, H.H., Krause, E., Nockermann, M, and Schober. M. (1995) "Comparative measurements of the canonical boundary layer at $\mathrm{Re}_{\delta_2} \leq 6\times10^4$ on the wall of the German-Dutch windtunnel," *Physics of Fluids* Vol. 7, 1275-1281.

Fernholtz, H.H., Finley, P.J. (1996) "The incompressible zero-pressure-gradient turbulent boundary layer: An assessment of the data," *Prog. Aerospace Sci.* Vol. 32, 245-311.

Fife, P., Wei, T., Klewicki, J., and McMurtry, P. (2005) "Stress gradient balance layers and scale hierarchies in wall-bounded turbulent flows," *J. Fluid Mech.* Vol. 532, 165-189.

Gad-el-Hak, M., and Bandyopadhyay. P.R. (1994) "Reynolds number effects in wall-bounded turbulent flows," *Appl. Mech. Rev.* Vol. 47, 307-365.

George, W.K., and Castillo, L. (1997) "Zero-pressure-gradient turbulent boundary layer," *Appl. Mech. Rev.* Vol. 50, 689-729.

Launder, B.E. and Spalding, D.B. (1972) *Mathematical Models of Turbulence* (Academic Press, London).

Lindgren, B., Österlund, J.M., and Johansson, A.V. (2004) "Evaluation of scaling laws derived from Lie group symmetry methods in zero-pressure-gradient turbulent boundary layers," *J. Fluid Mech.* Vol. 502, 127-152.

Marusic, I., and Kunkel, G.J. (2003) "Streamwise turbulence intensity formulation for flat-plate boundary layers," *Physics of Fluids* Vol. 15, 2461-2464.

Marusic, I., Uddin, A.K.M., and Perry, A.E. (1997) "Similarity law for the streamwise turbulence intensity in zero-pressure-gradient turbulent boundary layers," *Physics of Fluids* Vol. 9, 3718-3726.

Metzger, M.M., and Klewicki, J.C. (2001) "A comparative study of near-wall turbulence in high and low Reynolds number boundary layers," *Physics of Fluids* Vol. 13, 692-701.

Metzger, M.M., Klewicki, J.C., Bradshaw, K.L., and Sadr, R. (2001) "Scaling the near-wall axial turbulent stress in the zero pressure gradient boundary layer," *Physics of Fluids* Vol. 13, 1819-1821.

Nagib, H., Christophorou, C., Reidi, J.-D., Monkewitz, P., Österlund, J. and Gravante, S. (2004) "Can we ever rely on results from wall-bounded turbulent flows without direct measurements of wall shear stress?" AIAA Paper no. 2004-2392.

Österlund, J.M., Johansson, A.V., Hagib, H.M., and Hites, M.H. (1999) "Wall shear stress measurements in high Reynolds number boundary layers from two facilities," 30th AIAA Fluid Dynamics Conference, Norfolk, Virginia (AIAA paper no. 99-3814).

Österlund, J.M., Johansson, A.V., and Nagib, H. (2000a) "A note on the overlap region in turbulent boundary layers", *Physics of Fluids* Vol. 12, 1-4.

Österlund, J.M., Johansson, A.V., Nagib, H., and Hites, M.H. (2000b) "Comment on 'A note on the intermediate region in turbulent boundary layers [*Phys. Fluids* 12, 2159]'", *Physics of Fluids* Vol. 12, 2360-2363.

Panton, R.C. (2002) "Evaluation of the Barenblatt-Chorin-Prostokishin power law for turbulent boundary layers," *Physics of Fluids* Vol. 14, 180-1808.

Patel, V.C. (1965) "Calibration of the Preston tube and limitations on its use in pressure gradients," *J. Fluid Mech.* Vol. 23, 185-208.

Park, J.T., Cutbirth, J.M., and Brewer, W.H., (2003) "Hydrodynamic Performance of the Large Cavitation Channel (LCC)," *Proc. 4th ASME_JSME Joint Fluids Engineering Conference*, Honolulu, Hawaii.

Pope, S.B. (2000) Turbulent Flows (Cambridge University Press, UK), pp. 298-332, 442-445.

Saddoughi, S. G. and Veeravalli, S. V. (1994) "Local isotropy in turbulent boundary layers at high Reynolds numbers," *J. Fluid Mech.* Vol. 268, 333-372.

Sanders, W.C., Winkel, E.S., Dowling, D.R., Perlin, M., Ceccio, S.L. 2006 "Bubble friction drag reduction in a high Reynolds number flat plate turbulent boundary layer," *J. Fluid Mech.* Vol. 552, 353-380.

Sreenivasan, K.R. (1989) "The turbulent boundary layer," *Frontiers in Experimental Fluid Mechanics* Vol. 46, 159-209.

Wei, T., Fife, P., Klewicki, J., and McMurtry, P. (2005) "Properties of the mean momentum balance in turbulent boundary layer, pipe, and channel flows," *J. Fluid Mech.* Vol. 522, 303-327.

White, F.M. (2006) Viscous Fluid Flow, 3rd Ed. (McGraw-Hill, New York), pp. 411-425, 433-437.

IV. TABLES

Table 1: TBL Characteristics for the LDV profile measurement conditions.

x	U_e	δ_{99}	δ^*	θ	τ_w	u^*	l_v	$Re_x = U_e x/\nu$	$Re_\theta = U_e \theta/\nu$	δ_{99}/l_v
m	m/s	mm	mm	mm	Pa	m/s	µm	$\times 10^{-6}$	$\times 10^{-3}$	$\times 10^{-3}$
5.815	6.65	57	7.13	5.65	43.7	0.209	4.76	38.9	37.8	11.9
6.055	6.65	58	7.17	5.67	43.7	0.209	4.76	40.5	37.9	12.2
10.555	6.69	85	9.96	7.99	42.2	0.207	4.85	71.0	53.7	17.5
10.795	6.71	95	10.44	8.40	42.2	0.207	4.85	73.0	56.6	19.6
5.815	13.23	55	6.67	5.27	159	0.399	2.50	77.3	70.1	22.0
6.055	13.27	54	6.65	5.24	159	0.399	2.50	80.8	69.9	21.6
10.555	13.36	82	9.35	7.59	152	0.390	2.56	142	102	32.0
10.795	13.42	91	9.81	8.00	152	0.390	2.56	146	108	35.5
5.815	19.92	53	6.38	5.15	344	0.587	1.70	116	103	31.1
6.055	19.94	55	6.49	5.23	344	0.587	1.70	121	105	32.4
10.555	20.18	81	8.93	7.28	323	0.569	1.75	214	154	46.3
10.795	20.25	95	9.52	7.81	323	0.569	1.75	220	159	54.3

FIGURE CAPTIONS

Fig. 1. Schematic of the test model showing the test surface (a) and the instrumentation access side (b). (ESWT Fig. 3)

Fig. 2. Schematic of the near wall particle tracking velocimetry setup. The illumination light pulses originate in a double-cavity Nd-YAG PIV laser head that is mounted to the outside wall of the water tunnel. Sheet-forming optics and a 45° mirror inside a water-proof optics box relay the fan the light into a sheet that is parallel the flow direction and perpendicular to the test surface. Side-scattered light from the sheet is directed via another 45° mirror to a digital camera after passing through two cylindrical lenses (focal lengths: +75 mm, and –300 mm) to provide anisotropic, preferential magnification in the *y*-direction.

Fig. 3. PTV second-frame search window shape (a), and size specifications as a function of y^+ (b). The search window is *X*-pixels (solid line) long with a vertical extent of $\pm Y$ pixels (dash-dotted line). Here, *X* and *Y* increase with the distance from the wall until $y^+ \sim 15$ where they become constant.

Fig. 4. Sample PTV processing images. (a) First-frame particle images with the matched-filter-identified particle centroids marked with a white cross in a black circle. The wall is located at $y^+ = 0$ and the flow is from left to right. The frame is 125 pixels in the *x*-direction by 100 pixels in the *y*-direction). (b) A composite drawing superimposing the second-frame matched-filter-identified particle-image centers (black dots), the particle image locations from the first frame (white cross in a black circle), and search envelopes. (c) The vectors resulting from matching the particles in the dual-frame exposures.

Fig. 5. PTV-determined values of the normalized velocity variances: $\rho\overline{u'^2}/\tau_w = \overline{u'^2}^+$ (a), and $\rho\overline{v'^2}/\tau_w = \overline{v'^2}^+$ (b) for six different combinations of the second-frame search window size parameters for $U_e = 13.2$ m/s and $x = 10.68$ m: (×) $a_1 = 1.4$, $a_2 = 0.41$, $a_3 = 1.25$, $a_4 = 0.006$; (+) $a_1 = 1.5$, $a_2 = 0.46$, $a_3 = 1.4$, $a_4 = 0.0045$; (*) $a_1 = 1.65$, $a_2 = 0.50$, $a_3 = 1.5$, $a_4 = 0.0075$; (∇) $a_1 = 1.9$, $a_2 = 0.53$, $a_3 = 1.6$, $a_4 = 0.011$; (•) $a_1 = 1.8$, $a_2 = 0.56$, $a_3 = 1.6$, $a_4 = 0.009$; (o) $a_1 = 2.2$, $a_2 = 0.66$, $a_3 = 1.9$, $a_4 = 0.012$. The search envelope maximum sizes (X_{max}, Y_{max}) in pixels are (21, 11) for (×) and (+), (22, 12) for (*) and (•), and (23, 13) for (∇) and (o).

Fig. 6. Static pressure coefficient, $C_P(x) = \left(P(x) - P_1\right)/\frac{1}{2}\rho U_\infty^2$, vs. distance from the leading edge of the test model, *x* (in m), for the three primary test speeds: $U_\infty =$ 6.65 m/s □ [open square], 13.2 m/s O [open circle], and 19.9 m/s △ [open triangle]. Here, P_1 is the static pressure measured at the first tap at $x = 1.96$ m. Boundary layer growth on the model and the LCC test section sidewalls lead to a mildly favorable pressure gradient. (ESWT Fig. 6)

Fig. 7. Friction Coefficient vs. Re_x. Summary plot of all shear stress measurements: force balances, near-wall PTV, LDV total stress.
(ESWT Fig. 32)

Fig. 8. U vs. y – inner variables, $0.1 \leq y+ < 10^5$. Show linear fit for $y+ < 10$, and log-law fit for $y+ > 10$ shown. (ESWT Fig. 8) This figure should be big and plotted in the landscape orientation.

Fig. 9. Wake parameter, $\Delta U/u_\tau$, vs. $Re_\theta = U_e\theta/\nu$, from the LDV measurements at x = 5.94 m △ [open triangle] and x = 10.68 m ◇ [open diamond]. Also shown are the results of DeGraaff and Eaton (2000) ☐ [open square] for log-law constants of $\kappa = 0.41$ and $B = 5.0$. The solid curve is the correlation from Coles (1962) which asymptotes to approximately $\Delta U/u_\tau \cong 2.7$ at high Reynolds number. The current data likely fall below 2.7 because of the mild favorable pressure gradient in the LCC test section. (ESWT Fig. 14)

Fig. 10. Comparison of the diagnostic mean-profile fitting functions from Osterlund (2000) for the log-law, $\Psi = \left(y^+ \, dU^+/dy^+\right)^{-1}$ shown in open symbols, and power-law, $\Gamma = \left(y^+/U^+\right)\left(dU^+/dy^+\right)$ shown in solid symbols. Part a) shows Ψ and Γ vs. y^+ for x = 5.94 m and U_∞ = 13.2 m/s (squares), x = 5.94 m and U_∞ = 19.9 m/s (triangles), x = 10.68 m and U_∞ = 13.2 m/s (circles), and x = 10.68 m and U_∞ = 19.9 m/s (diamonds). Part b) shows the mean fractional difference of Ψ and Γ vs. $Re_\theta = U_e\theta/\nu$ for $y^+ > 150$ and $y < 0.15\delta_{99}$. The lower mean fractional difference for the log law (open symbols) suggests that it is a better fit to the experimental data than a power law (solid symbols) in the stated range for *y*. (ESWT Fig. 15 a) and b)), and (ESWT Fig. 17)

Fig. 11. u'^2 vs. y, inner variables. (ESWT Fig. 18)

Fig. 12. part a) $(u'^\wedge 2)_{max}$ vs. Re_τ. (ESWT Fig. 19)
part b) u'^2 at y+ = 200 vs. Re_τ. (ESWT Fig. 20)

Fig. 13. "Eaton scaling" of u'^2 vs. y, inner variables. (ESWT Fig. 21)

Fig. 14. v'^2 vs. y, inner variables. (ESWT Fig. 22 & 23)

Fig. 15. u'v' vs. y, inner variables. (ESWT Fig. 24 & 25)

Fig. 16. Normalized total TBL shear stress vs. y, inner variables. log horizontal axis
part a) 6.65 m/s (all three measuring stations ?)
part b) 13.2 m/s (all three measuring stations ?)
part c) 19.9 m/s (all three measuring stations ?)
(composite or summary of ESWT Figs. 26-31)

Fig. 1

Fig. 2

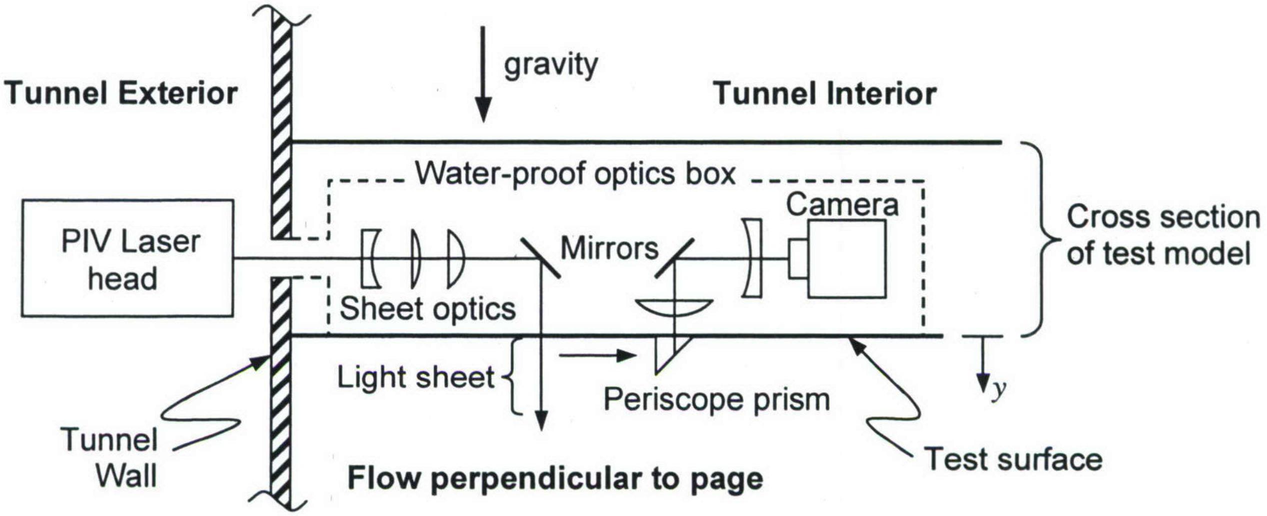
gravity
Tunnel Exterior
Tunnel Interior
Water-proof optics box
Camera
Cross section of test model
PIV Laser head
Mirrors
Sheet optics
Light sheet
Periscope prism
y
Tunnel Wall
Flow perpendicular to page
Test surface

Fig. 3a)

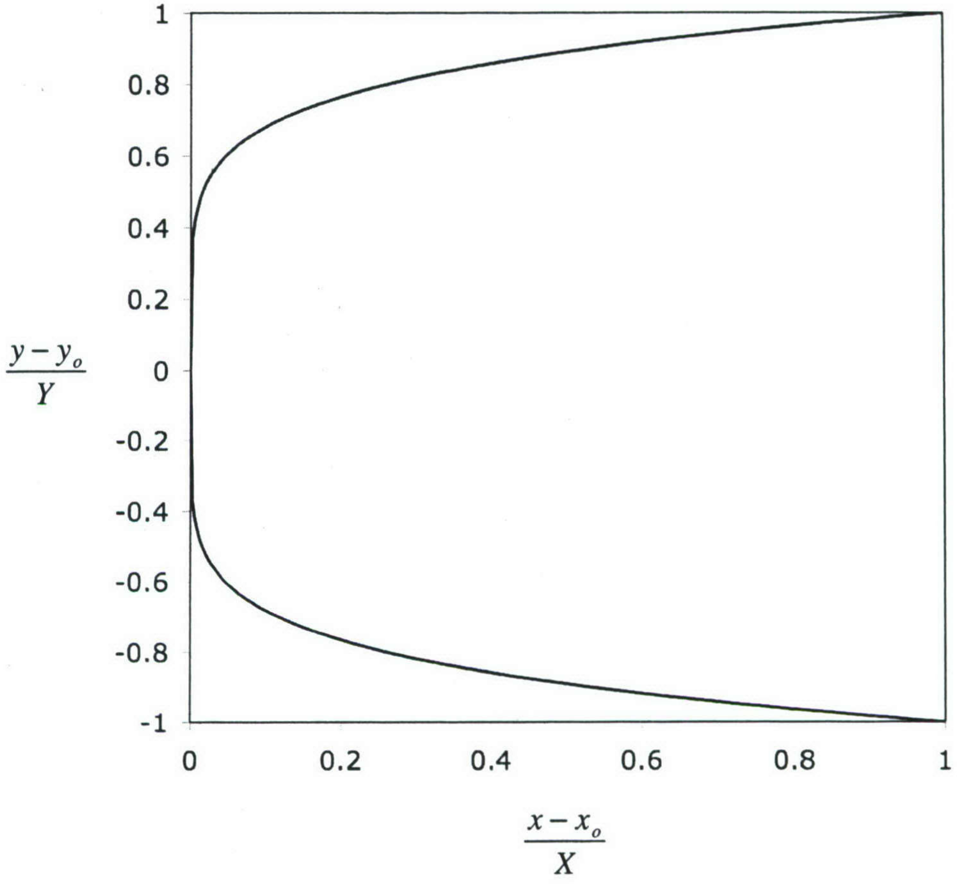

1
0.8
0.6
0.4
0.2
$\frac{y-y_o}{Y}$
0
-0.2
-0.4
-0.6
-0.8
-1
0
0.2
0.4
0.6
0.8
1
$\frac{x-x_o}{X}$

Fig. 3b)

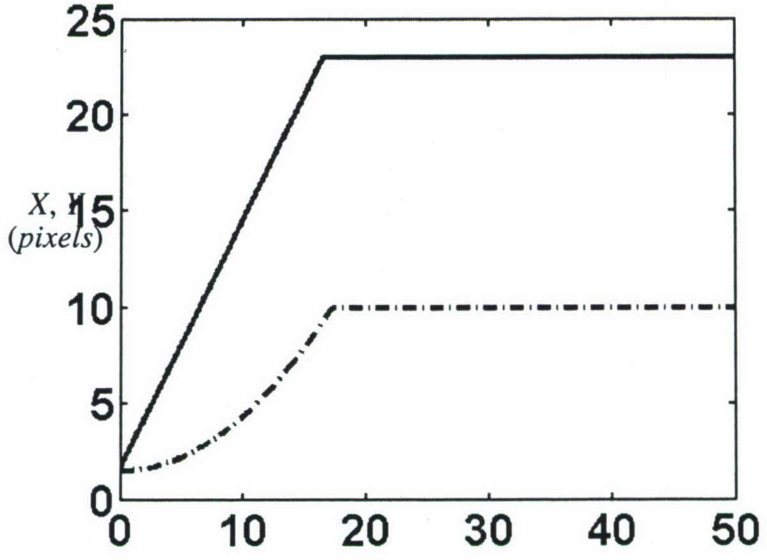

25
20
X, Y
(pixels)
15
10
5
0
0
10
20
30
40
50

Fig. 4

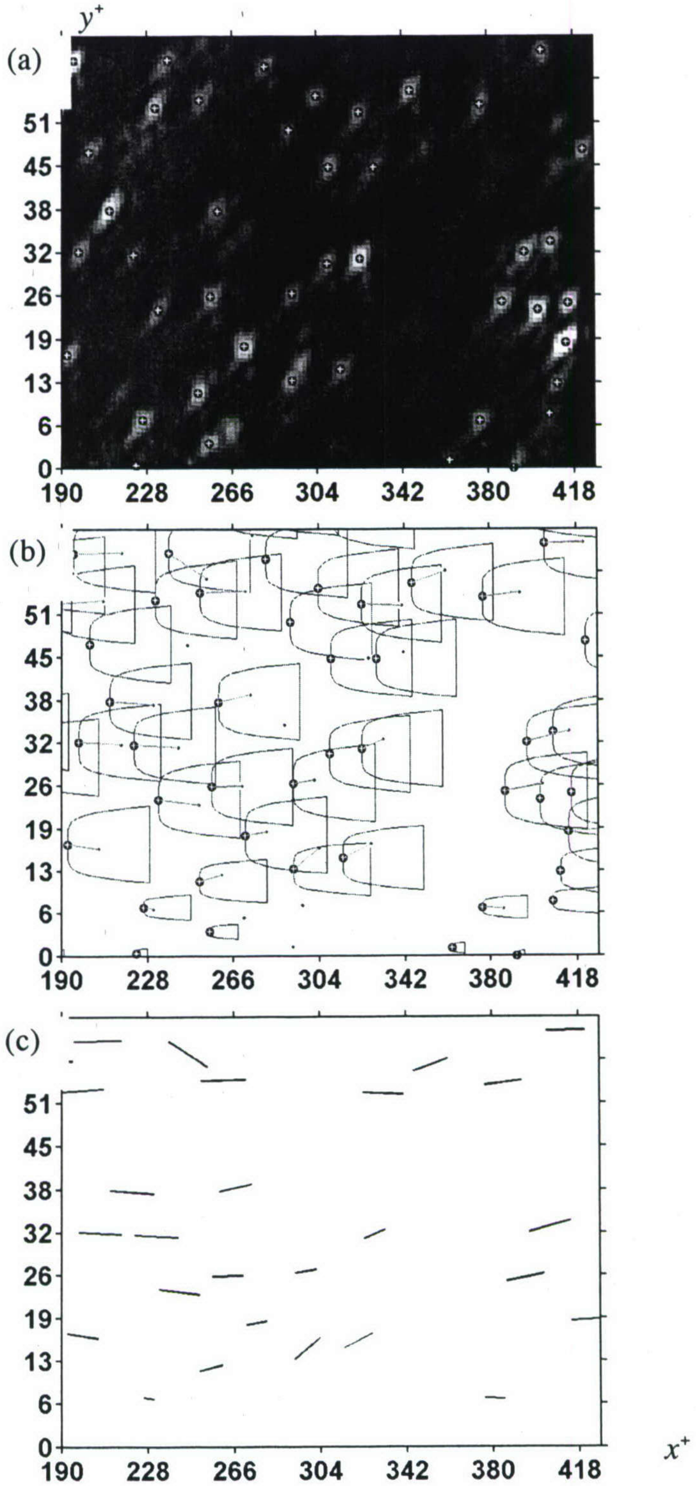

Fig. 5

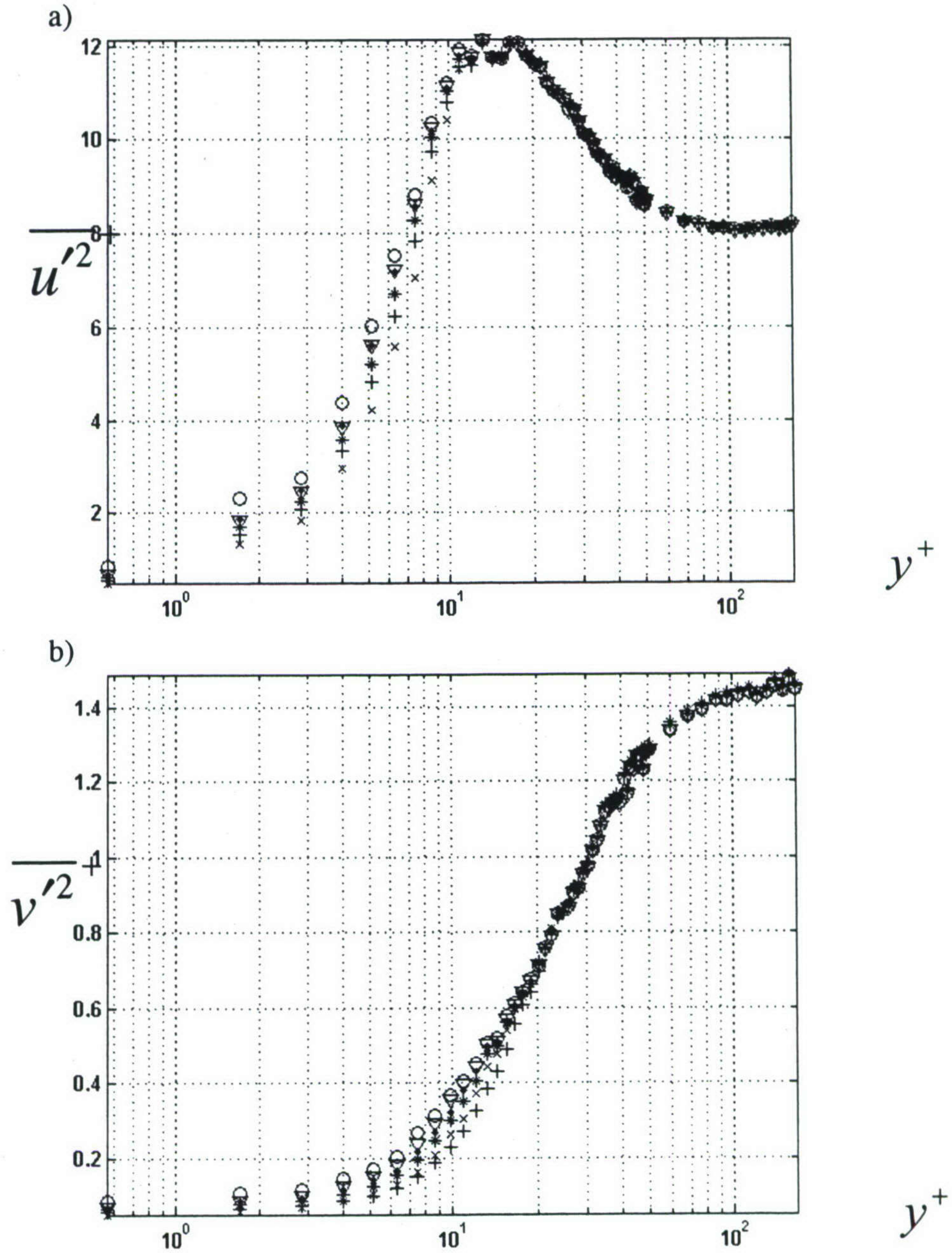
a)
12
10
8
6
4
2
$\overline{u'^2}^+$
y^+
10^0
10^1
10^2
b)
1.4
1.2
1
0.8
0.6
0.4
0.2
$\overline{v'^2}^+$
y^+
10^0
10^1
10^2

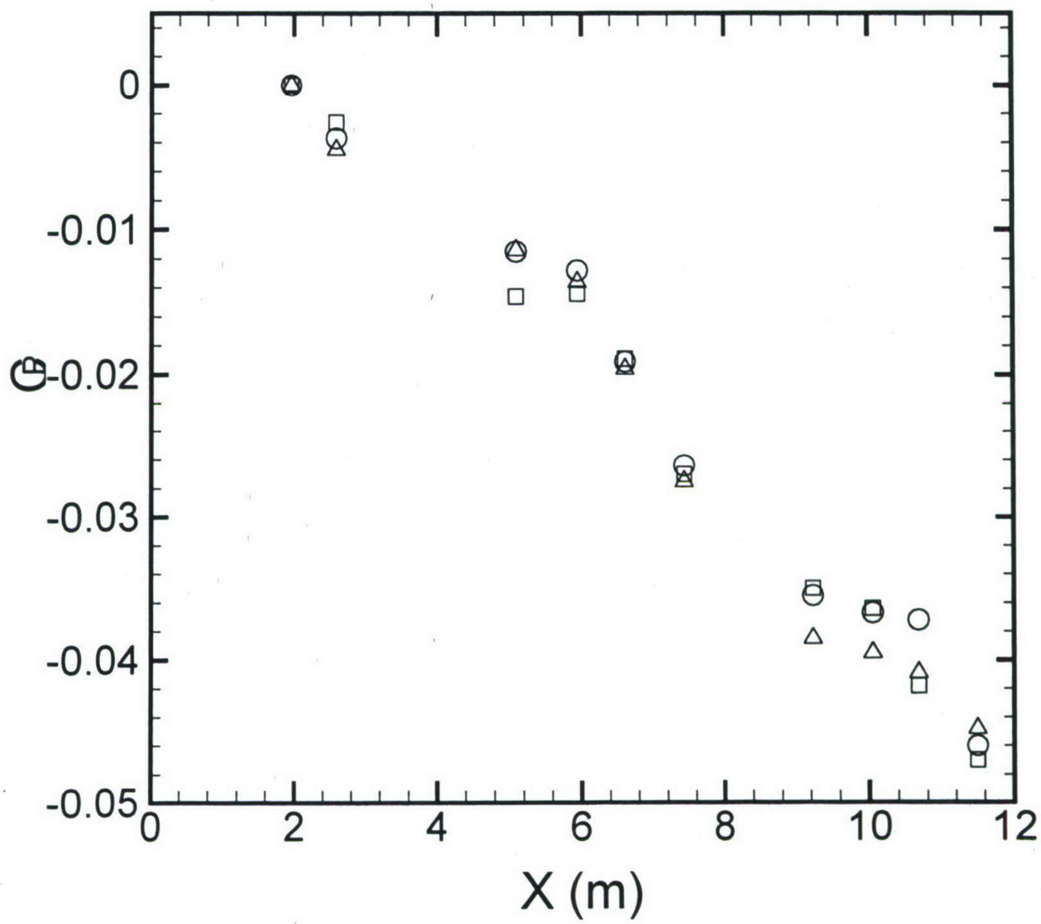

Fig. 5. Coefficient of pressure vs. downstream distance (ESWT Fig. 6)

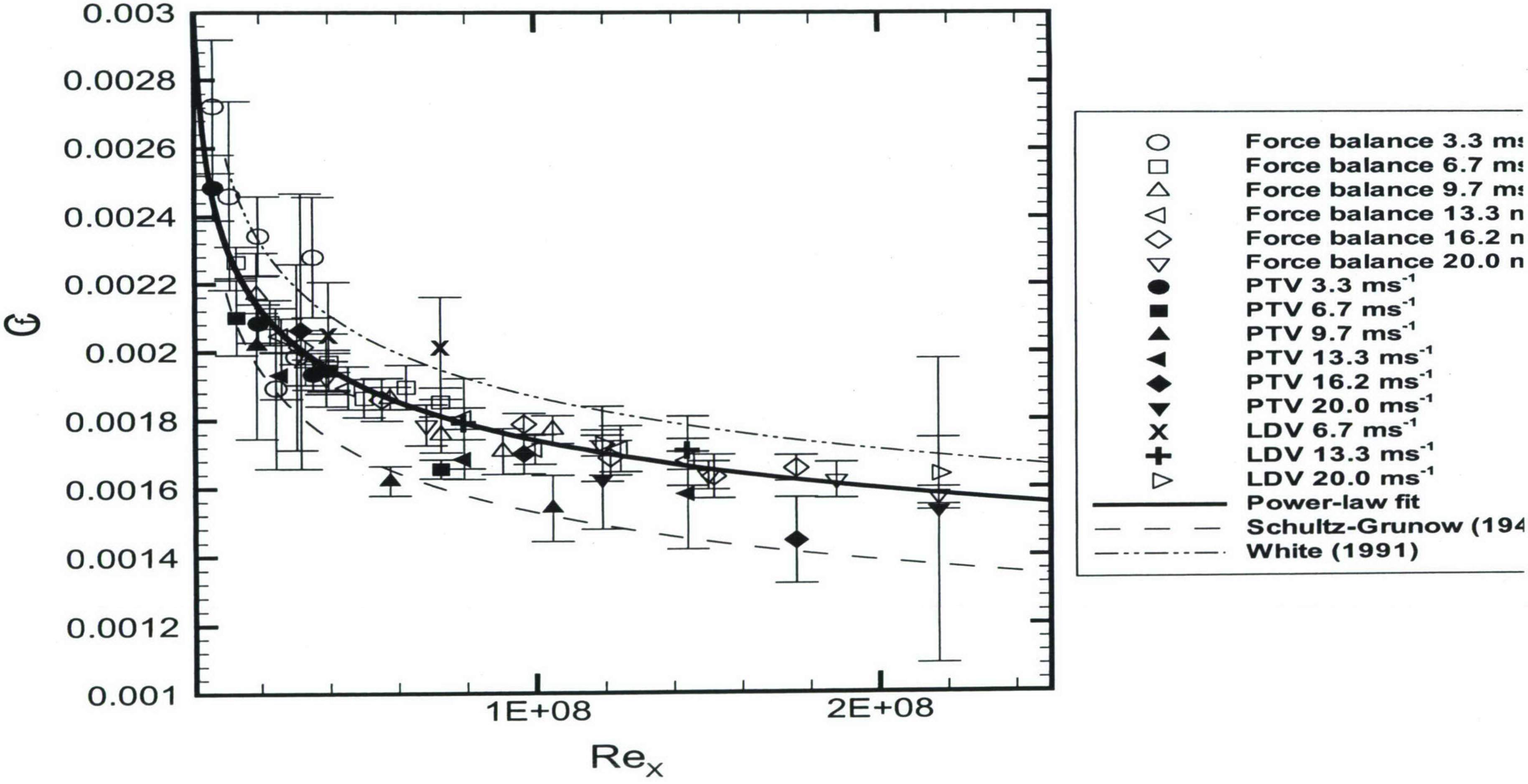

Fig. 6. Friction Coefficient vs. Re_x. Summary plot of all shear stress measurements: force balances, near-wall PTV, LDV total stress. (ESWT Fig. 32)

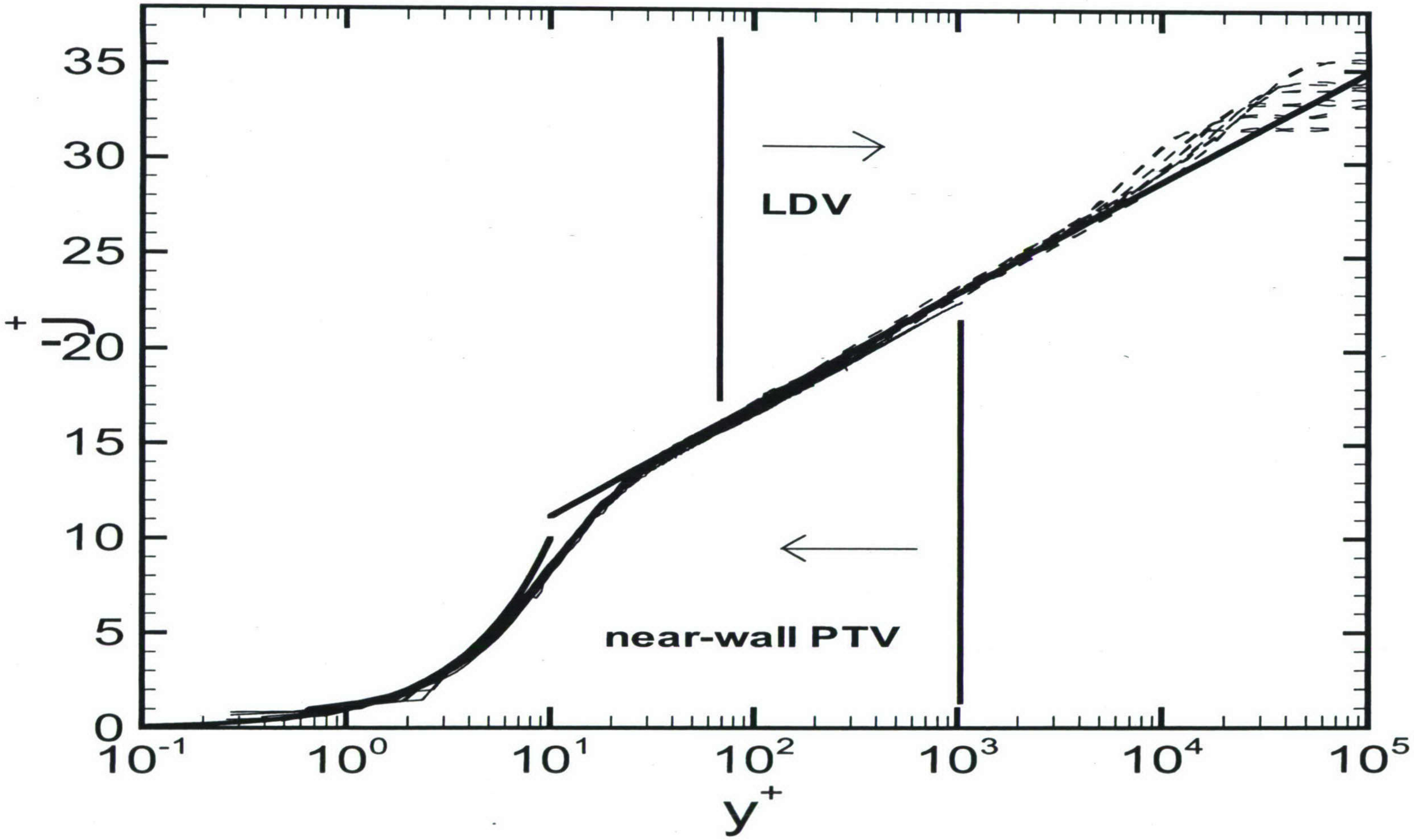

Fig. 7. U vs. y – inner variables, $0.1 \le y+ < 10^5$. Show linear fit for $y+ < 10$, and log-law fit for $y+ > 10$ shown. (ESWT Fig. 8) This figure should be big and plotted in the landscape orientation.

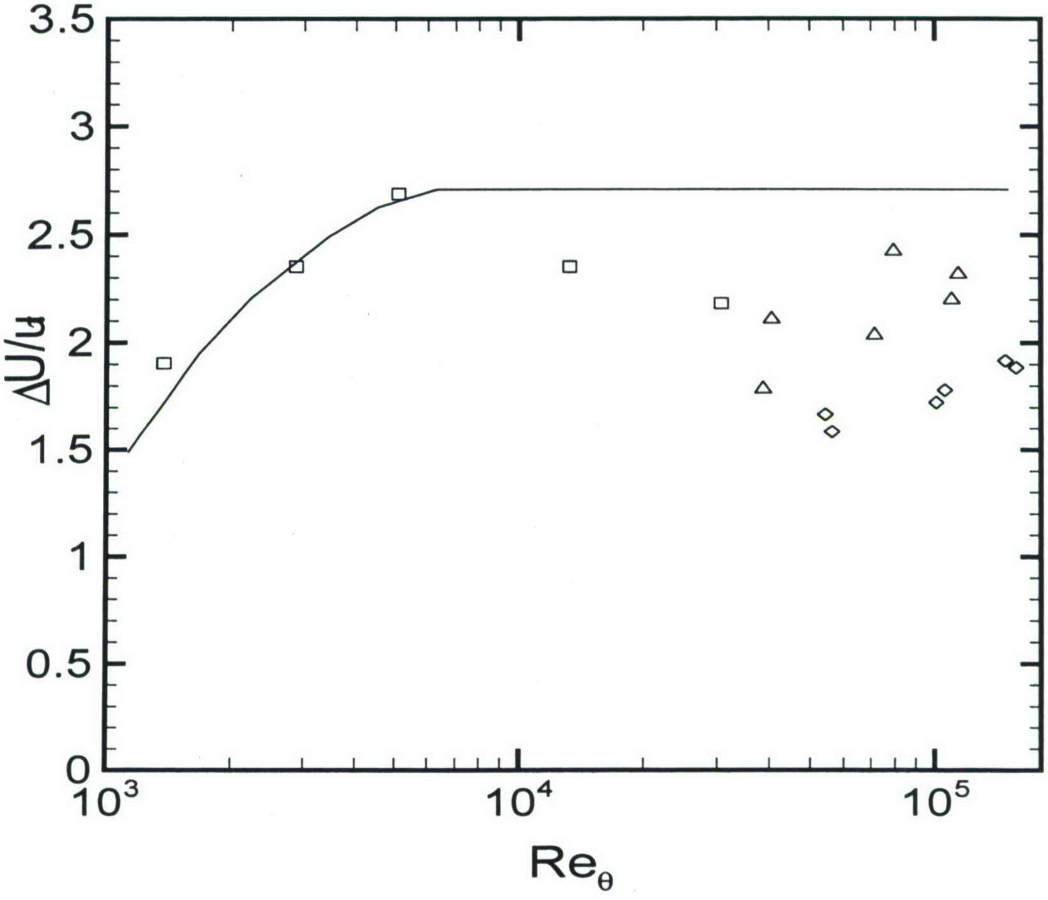

Fig. 8. Wake parameter, $\Delta U/u_\tau$, vs. $Re_\theta = U_e\theta/\nu$, from the LDV measurements at x = 5.94 m △ [open triangle] and x = 10.68 m ◇ [open diamond]. Also shown are the results of DeGraaff and Eaton (2000) □ [open square] for log-law constants of $\kappa = 0.41$ and $B = 5.0$. The solid curve is the correlation from Coles (1962) which asymptotes to approximately $\Delta U/u_\tau \cong 2.7$ at high Reynolds number. The current data likely fall below 2.7 because of the mild favorable pressure gradient in the LCC test section.

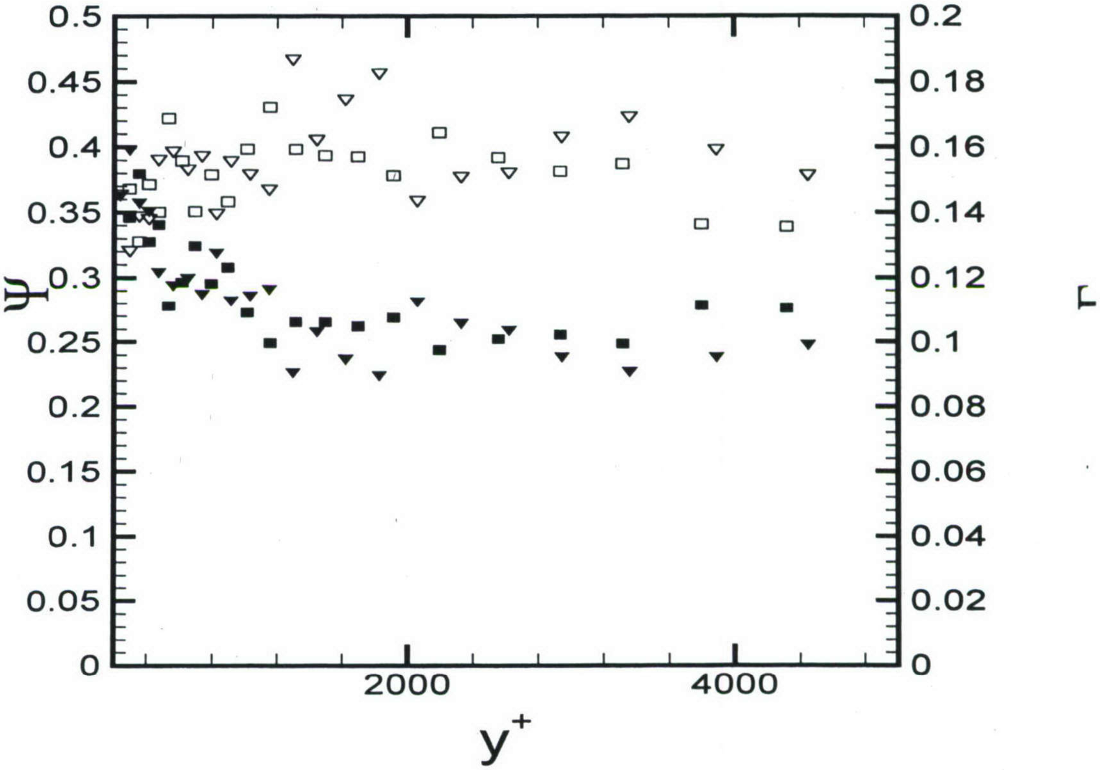
0.5
0.45
0.4
0.35
0.3
0.25
0.2
0.15
0.1
0.05
0
Ψ
0.2
0.18
0.16
0.14
0.12
0.1
0.08
0.06
0.04
0.02
0
Γ
2000
4000
y^+

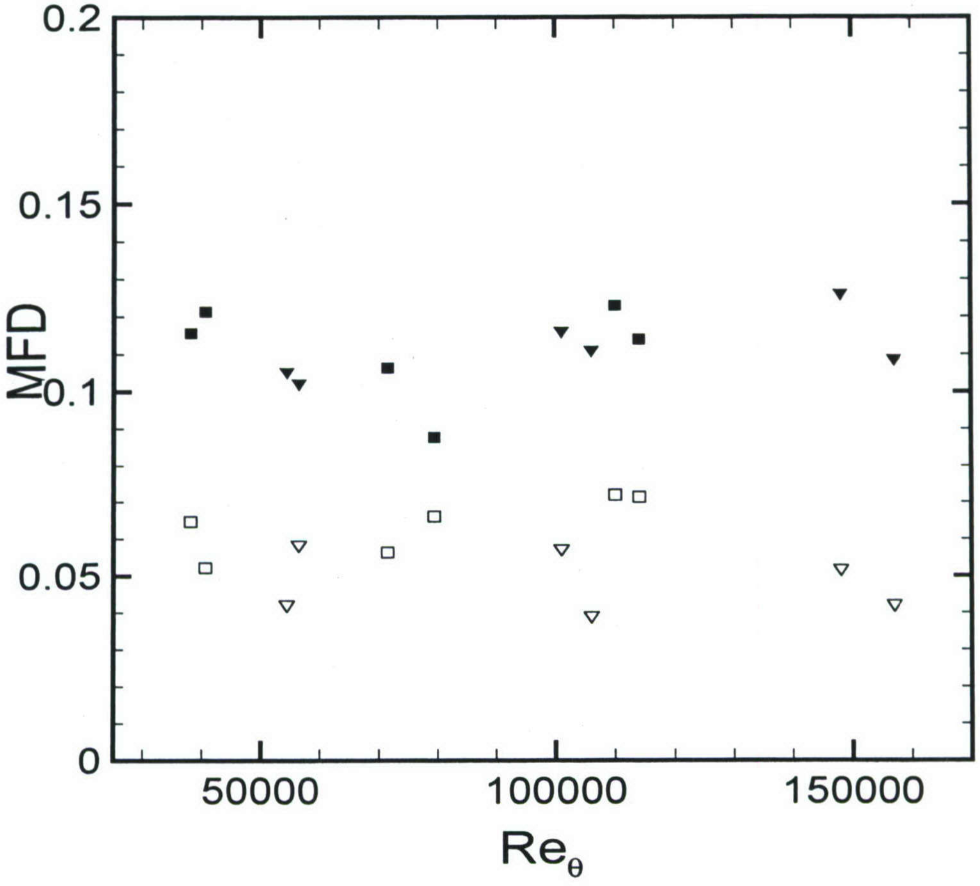

Fig. 9. Comparison of the diagnostic mean-profile fitting functions from Osterlund (2000) for the log-law, $\Psi = \left(y^+ \, dU^+/dy^+\right)^{-1}$ shown in open symbols, and power-law, $\Gamma = \left(y^+/U^+\right)\left(dU^+/dy^+\right)$ shown in solid symbols. Part a) shows Ψ and Γ vs. y^+ for $x = 5.94$ m and $U_\infty = 13.2$ m/s (squares), $x = 5.94$ m and $U_\infty = 19.9$ m/s (triangles), $x = 10.68$ m and $U_\infty = 13.2$ m/s (circles), and $x = 10.68$ m and $U_\infty =$ 19.9 m/s (diamonds). Part b) shows the mean fractional difference of Ψ and Γ vs. $Re_\theta = U_e\theta/\nu$ for $y^+ > 150$ and $y < 0.15\delta_{99}$. The lower mean fractional difference for the log law (open symbols) suggests that it is a better fit to the experimental data than a power law (solid symbols) in the stated range for y. (ESWT Fig. 15 a) and b)), and (ESWT Fig. 17)

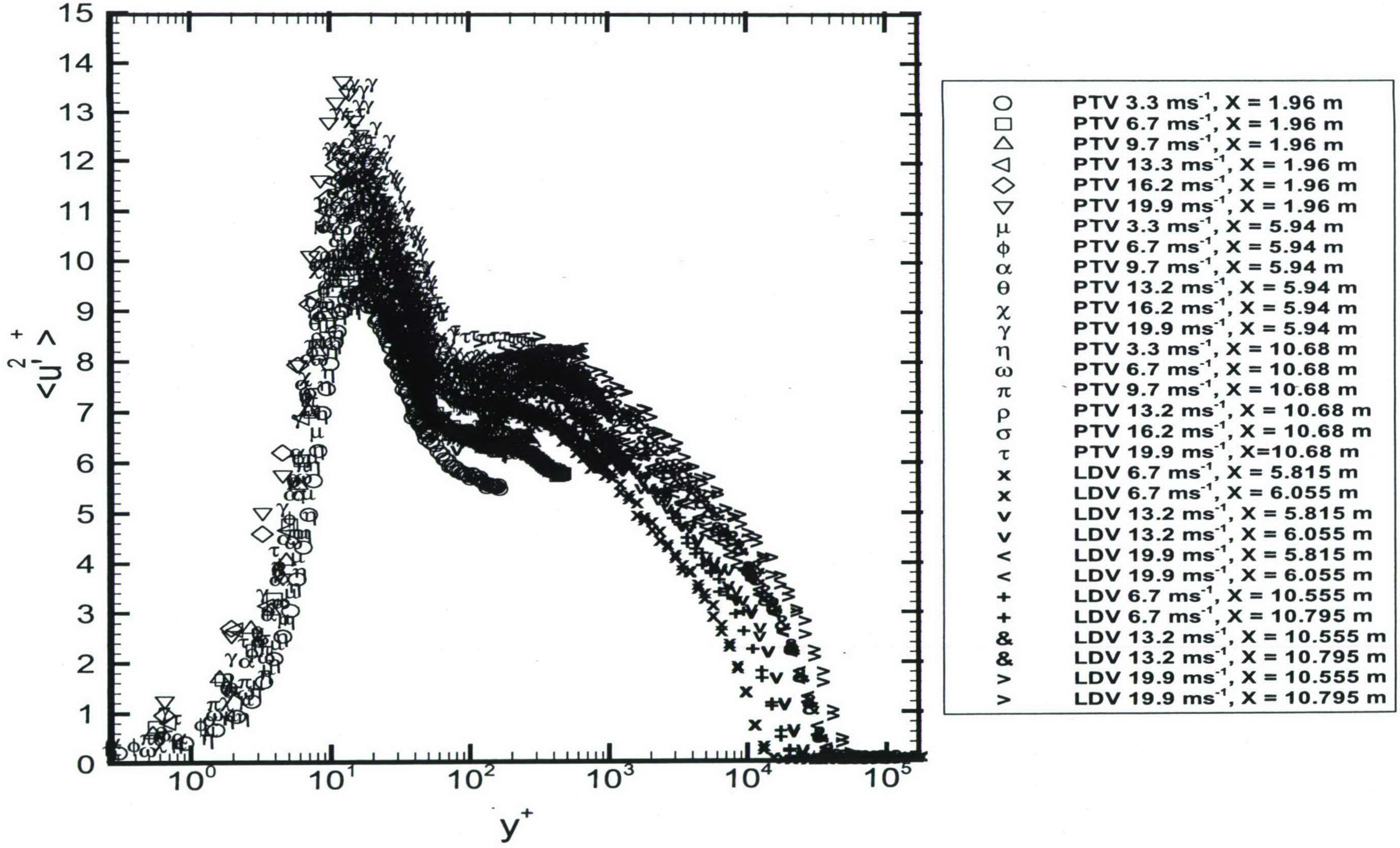

Fig. 10. u'^2 vs. y, inner variables. (ESWT Fig. 18)

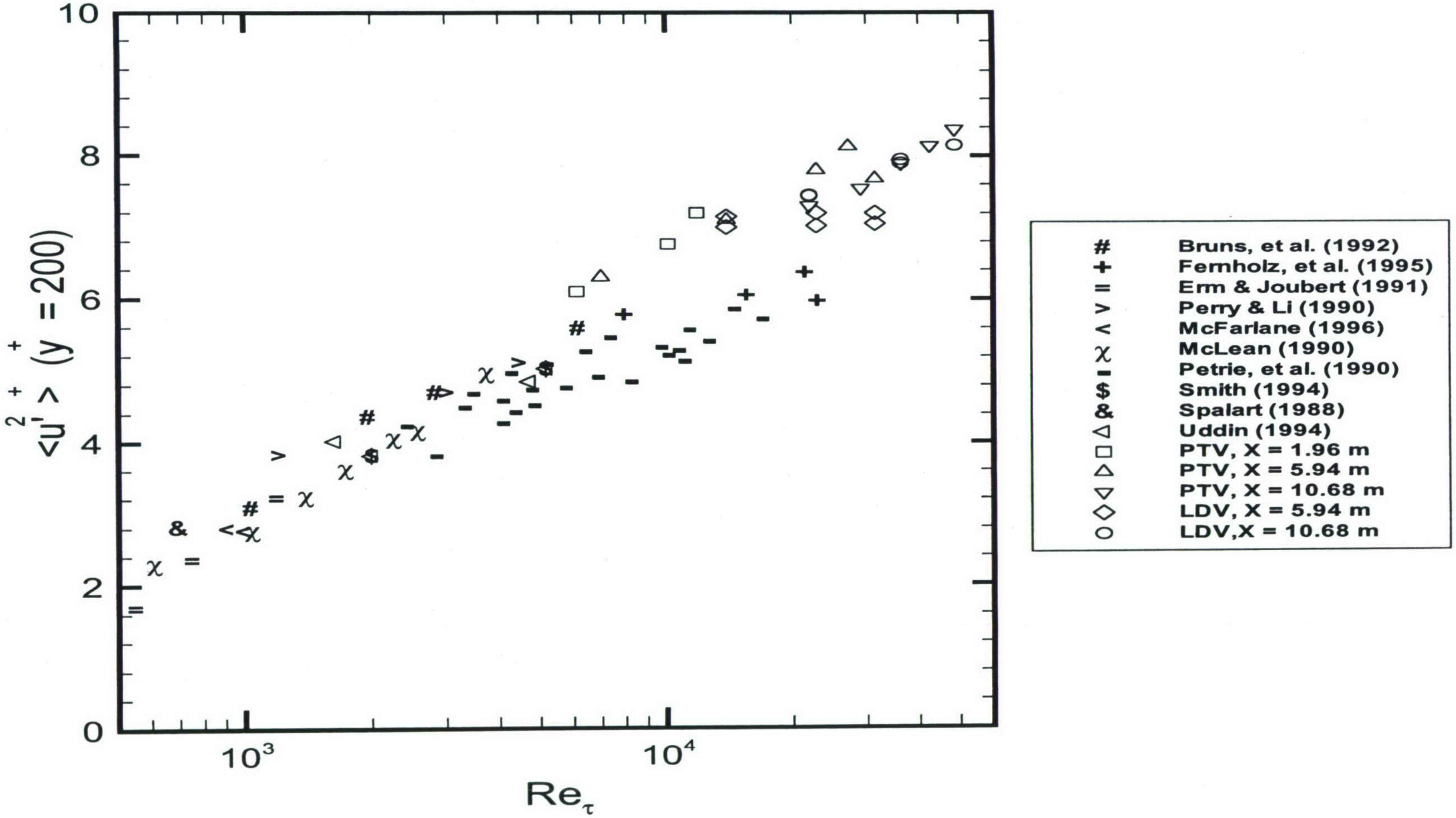

10
8
6
4
2
0
$\langle u'^{2+} \rangle$ (y^+ = 200)
10^3
10^4
Re_τ
Bruns, et al. (1992)
+ Fernholz, et al. (1995)
= Erm & Joubert (1991)
> Perry & Li (1990)
< McFarlane (1996)
χ McLean (1990)
▬ Petrie, et al. (1990)
$ Smith (1994)
& Spalart (1988)
◁ Uddin (1994)
□ PTV, X = 1.96 m
△ PTV, X = 5.94 m
▽ PTV, X = 10.68 m
◇ LDV, X = 5.94 m
○ LDV,X = 10.68 m

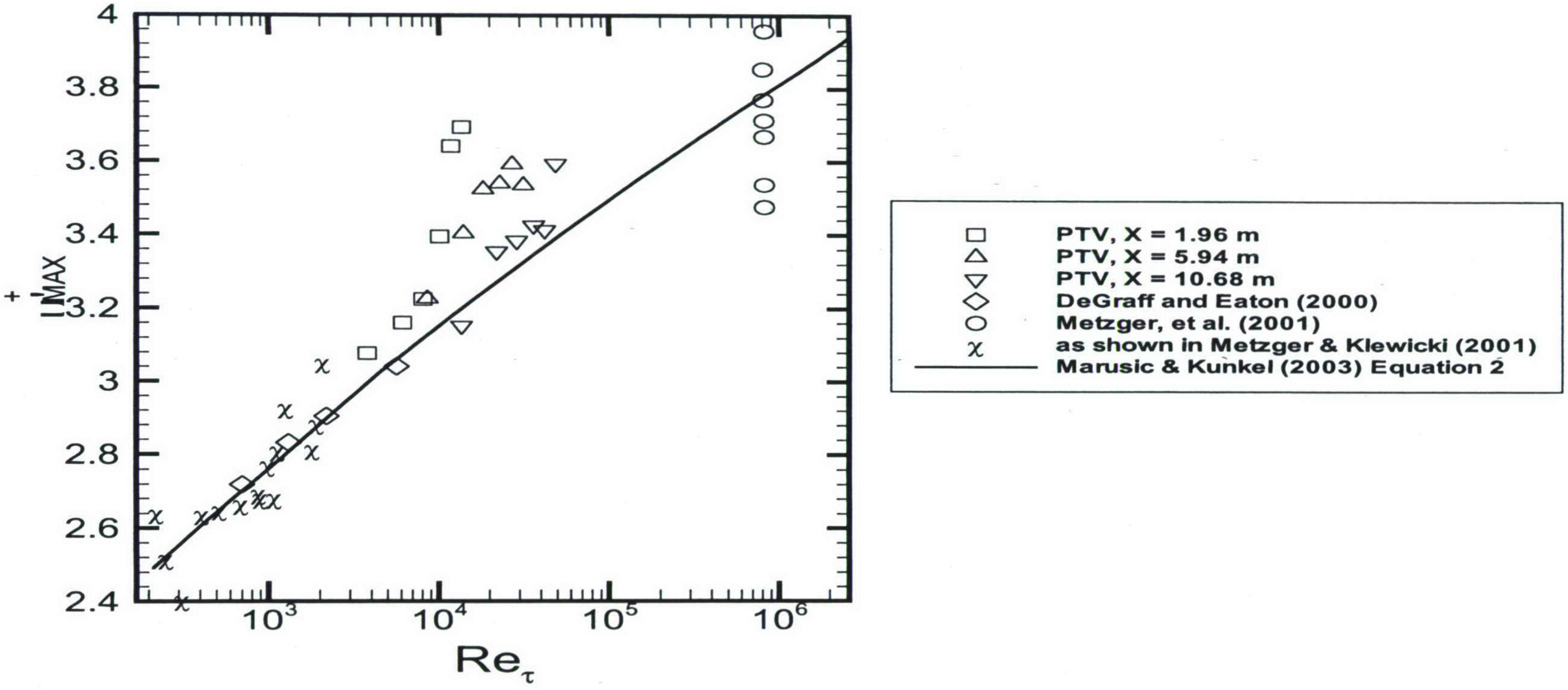

Fig. 11. part a) $(u'^2)_{max}$ vs. Re_τ. (ESWT Fig. 19)
part b) u'^2 at y+ = 200 vs. Re_τ. (ESWT Fig. 20)

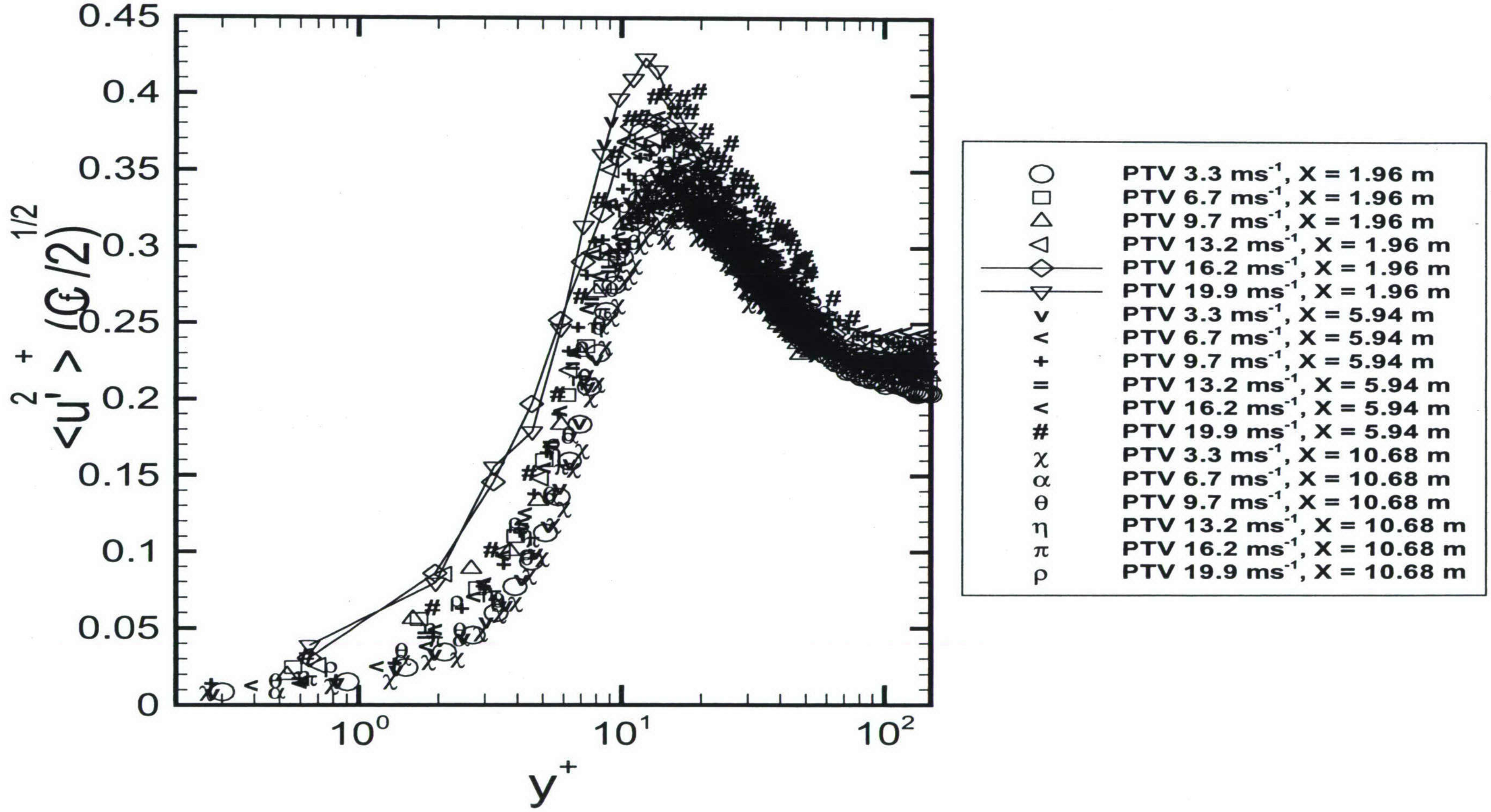

Fig. 12. "Eaton scaling" of u'^2 vs. y, inner variables. (ESWT Fig. 21)

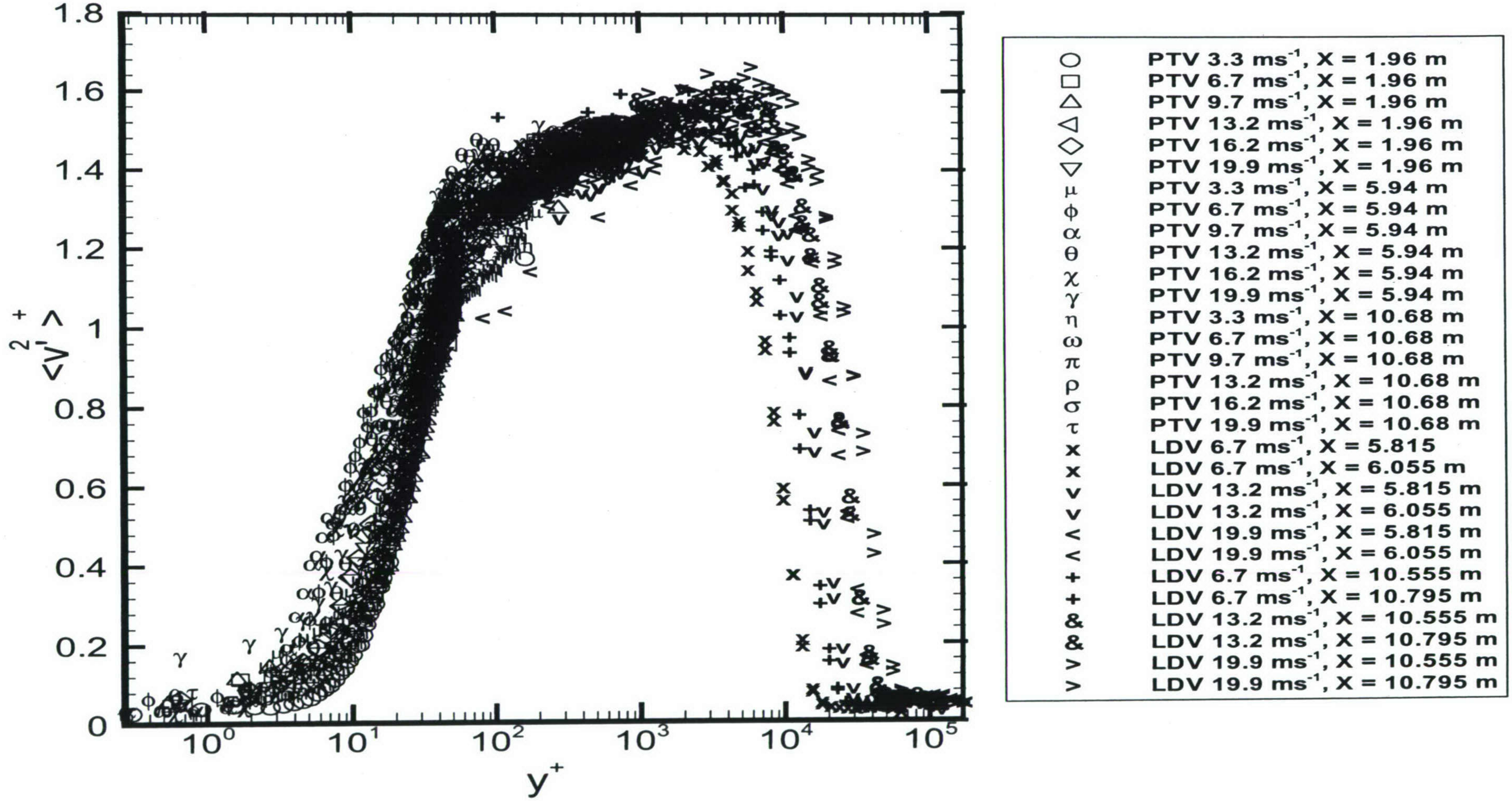

Fig. 13. v'^2 vs. y, inner variables. (ESWT Fig. 22 & 23)

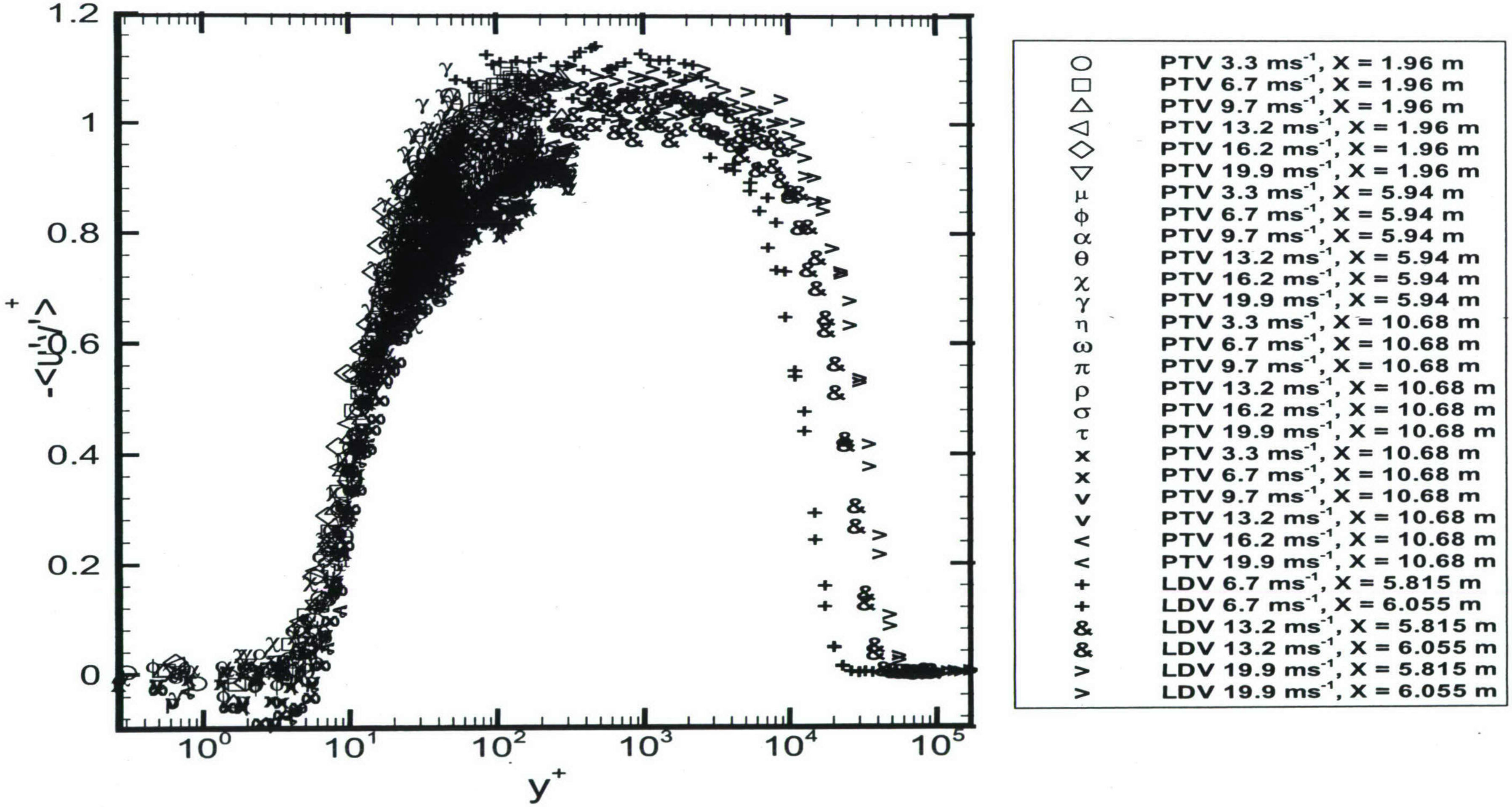

Fig. 14. u'v' vs. y, inner variables. (ESWT Fig. 24 & 25)

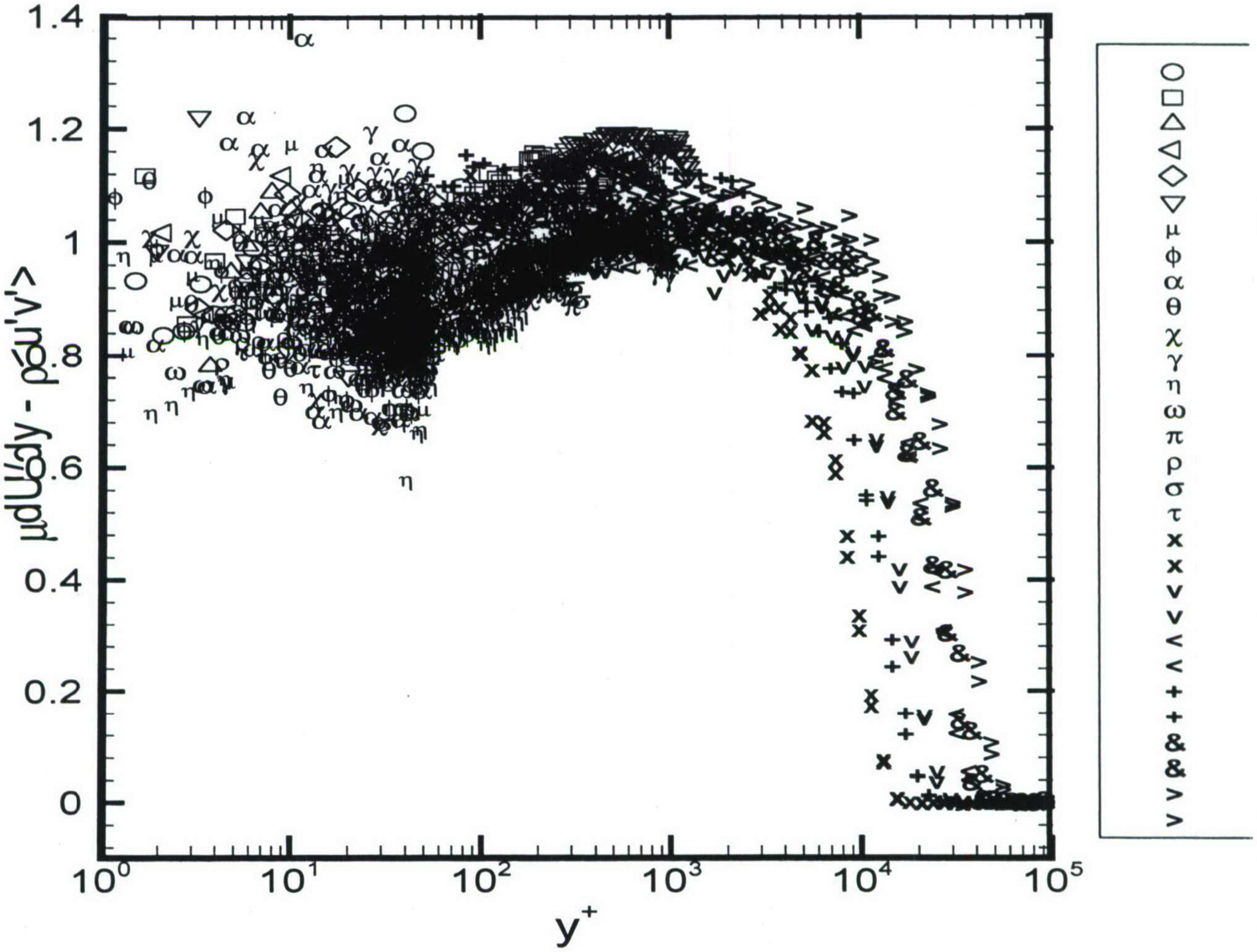

Fig. 15. Normalized total TBL shear stress vs. y, inner variables. (composite or summary of ESWT Figs. 26-31)

Appendix B:

High Reynolds number turbulent boundary layer friction drag reduction from wall-injected polymer solutions

E. S. WINKEL, G. OWEIS*, S.A., VANAPALLI,**
D. R. DOWLING, M. PERLIN, M. J. SOLOMON, AND S. L. CECCIO

University of Michigan, Ann Arbor
American University in Beirut*
University of Twente, The Netherlands**

Submitted for publication in the Journal of Fluid Mechanics

A set of experiments has been conducted at the William B. Morgan Large Cavitation Channel (LCC) in Memphis, Tennessee to investigate the phenomena of friction drag reduction at large scales and high Reynolds numbers in a controlled test environment. Drag reduction was achieved by injecting aqueous poly(ethylene oxide) (PEO) solutions at three different mean molecular weights into a near-zero-pressure-gradient turbulent boundary layer formed on a smooth flat test surface having a length of nearly 11 *m*. The test model had an overall length of 12.9 *m*, and spanned the 3.05 *m* width of the LCC test section. Friction drag was measured with six floating-plate force balances at downstream-distance-based Reynolds numbers up to 220 million and free stream speeds up to 20 ms^{-1}. For a given polymer type, the level of drag reduction was measured for a range of free stream speeds, polymer injection rates, and concentrations of the injected solution. Polymer concentration fields in the near-wall region ($0 < y < 2$ *mm*) were examined at three locations downstream of the injector using near-wall pulsed laser-induced-fluorescence imaging. Comparisons of the development and extent of friction drag reduction are drawn between the various test results from the current study, and between the current and prior PEO-solution-based friction drag reduction experiments. The evolution of near wall polymer concentration is divided into three regimes: the development region near the injector, where the injected polymer is highly stratified, forming filaments in the near-wall flow; the transitional mixing region, where the polymer begins to mix across the boundary layer; and the final region, where the polymer mixing occurs at the rate of boundary layer growth. The observed drag reduction and mixing processes are compared to previously reported results, using the standard K-Factor scaling, the physical basis and usefulness of this scaling is discussed. Finally, the near wall polymer concentration is correlated to the drag reduction achieved for the three polymer molecular weights employed. These data are related to the polymer solution rheology the local Weissenberg number, and the Weissenberg numbers for drag-reduction onset and shear based degradation. The data are shown to correlate to the universal drag reduction curves first proposed by Virk *et al.* (1967) for pipe flows. However, a scaling which would relate the differences in the intrinsic drag reduction and concentration with changes in the molecular weight was not found, possibly de to the presence of significant flow induced polymer degradation.

1. Introduction

Reduction of turbulent boundary layer skin friction in external flows is an enduring priority for fuel savings in marine transportation systems. Researchers have known for more than fifty years that the presence of high molecular weight polymers in the near-wall region of a turbulent boundary layer (TBL) flow can lead to reduction of the friction drag by as much as 70% compared to the friction produced by a corresponding flow of pure water, even when the polymer concentration is on the order of a few tens of weight parts per million (*wppm*). The mechanism underlying this polymer drag reduction has been under investigation for several decades, and an overall picture of the interaction of the long-chain polymers with the underlying turbulent flow has emerged through analytical, experimental, and numerical studies. Dubief *et al.* (2004) discusses in detail how the stretching and recoiling of polymer molecules in the near wall flow can modify the self-sustained near-wall turbulence regeneration cycle. Near wall turbulence in Newtonian flow is sustained through the production of near wall vortices in the buffer region and streaks in the viscous sub-layer (Jimenez and Pinelli, 1999). The presence of the polymer molecules modifies the non-linear interactions by extracting energy from the buffer layer vortices and releasing it in the near wall streaks. This leads to enhanced stream-wise velocity fluctuations, reduced wall-normal velocity fluctuations, and increased spacing between stream-wise vortices in the near-wall region. The balance of stresses in the flow near the wall are then composed of a combination of viscous, Reynolds, and (non-trivial) polymer stresses. Finally, the state of maximum drag reduction (MDR) is achieved when there is a sufficient concentration of polymer molecules in the near-wall region to produce a new, self-sustained regeneration cycle. Once MDR is achieved, further increases in polymer concentration will no longer directly result in turbulence modification and further reduction in friction drag. Instead, increasing polymer concentration in an MDR flow may increase skin friction through an increase in the bulk shear viscosity. The detailed interactions of the polymer with the underlying turbulent flow is still the object of study, but this phenomenological description is consistent with experimental observations of drag reduction, including the recent work of Warholic *et al.* (1999), Ptasinski *et al.* (2003), and White *et al.* (2004).

Polymer additives are used commercially to reduce the friction developed by flows in pipes and other conduits (Sellin, 1982). In most internal flow applications, the polymer is introduced and mixed into the flow to produce a relatively uniform and sustained polymer distribution in the flow (in the absence of polymer degradation). However, application of polymer drag-reduction to external flows is complicated by the need to inject the polymer solution and allow it to be mixed with free-stream fluid in the TBL flow. Even at MDR, mixing in the TBL continues. Without continual addition of polymer, the near-wall polymer concentration decreases as the TBL entrains free-stream fluid. Once the near-wall polymer concentration is sufficiently reduced, skin-friction drag reduction is diminished and then lost. Therefore, practical application of polymer drag reduction to external flows requires a careful balance between the cost of carrying, mixing, and injecting the polymer, and the benefit of the resulting drag reduction.

Experimental investigations of external TBL drag-reduction by polymer additives have been conducted at a number of scales and flow speeds. A variety of polymers having different mean molecular weighs, M_w, have been used for TBL drag reduction studies, with poly(ethylene oxide) (PEO) and polyacrylamide (PAM) being the two most commonly reported. Polymer skin-friction drag reduction has been examined on flat plate TBL at downstream-distance-based Reynolds numbers up to 45 million (Vdovin and Smol'yakov, 1981) and speeds up to 16.8 ms^{-1} (Petrie, *et al.*, 1996a). In general, a polymer solution is injected into a developed TBL *via* a span-wise slot or line source on the wall. The solution concentration,

C_i, and flux per unit span, Q_i, are varied to determine their influence on the magnitude and extent of friction drag reduction that is achieved. With the injection of high concentration polymer solutions (> 500 *wppm*), the drag-reduction peaks down-stream of injection and then decreases with distance from the injector. The decrease in drag reduction with downstream distance results from dilution in the TBL and possibly from flow-induced polymer degradation.

Transport and dilution of the injected polymer solution in a TBL have been measured experimentally by adding a dye tracer to the injected polymer and extracting samples of near-wall fluid downstream from the injection location (Fruman and Tulin, 1976; Vdovin and Smol'yakov, 1978 and 1981) or by using laser-induced fluorescence of a dye mixed into the polymer solution (LIF) (Fontaine *et al.*, 1992). Turbulent mixing of polymers injected into the near-wall region of a TBL (Poreh and Hsu, 1972) is reduced when compared to mixing of a passive scalar (Poreh and Cermak, 1964), and this is consistent with the observed reduction in skin friction in the polymer-injected flow.

Degradation (chain-scission) of long-chain polymer molecules in the turbulent flow is also of practical concern. Investigations of polymer degradation have been conducted primarily in pipe flows and rotational Taylor-Couette flow devices. Currently no measurements of polymer degradation in TBL flows have been reported. In pipe flows, Horn and Merrill (1984) have shown that the polymer chains break near the mid-point, effectively reducing the polymer molecular weight by 50%. Vanapalli *et al.* (2005) and Vanapalli *et al.* (2006) developed relationships relating the near-wall shear to the degradation of PEO with various molecular weights, and their results indicate that chain-scission occurs in PEO solutions at shear rates much lower than those of previous TBL studies and the present experiments.

Application of polymer drag reduction to large-scale external flows necessitates an understanding of how the injected polymer mixes and possibly degrades as it is transported downstream of the injection location. Moreover, it is useful to understand how experimental results at lower Reynolds numbers compare to similar results at higher speeds and larger length scales. In particular, it is important to determine: (1) the downstream persistence of TBL drag reduction given the aforementioned effects of mixing and polymer degradation; (2) the local near-wall concentration with downstream distance; and (3) the influence of the molecular and rheological properties of the injected polymer solutions on the resulting friction drag reduction and near-wall concentrations.

Presented here are the results of large-scale experiments designed to examine TBL polymer friction drag reduction on a smooth surface. A comprehensive data set was gathered during the experiments, including the local average skin friction, and near-wall velocity and concentration fields measured with micro-Particle Image Velocimetry (PIV) and micro-Planar Laser Induced Fluorescence (PLIF) systems. Here, the relationship between polymer mean molecular weight, injection concentration, injection flux, free-stream speed, and the resulting drag reduction and turbulent polymer diffusion is reported. The relationship between near-wall polymer concentration and the drag reduction is also examined, along with the possibility of TBL-flow-induced polymer degradation.

2. Experimental Methods

2.1. Test facility and model

Experiments were conducted in the William B. Morgan Large Cavitation Channel (LCC), the world's largest low-turbulence (free stream turbulence < 0.5%), re-circulating water tunnel. The dimensions of the test section are 16 m (length) and 3.05 *m* x 3.05 *m* (width and height). Details of the facility and its use can be found in Etter *et al.* (2005). The test model was a 12.9 *m* long, 3.05 *m* wide, and 0.18 *m* thick rigid flat plate, spanning the entire width of the LCC test section. The model and its installation in the LCC is described in Sanders *et al.* (2006), so only a brief summary is provided here. The model's leading edge was a 4:1 ellipse and its trailing edge was a 15° full-angle truncated wedge. The model was positioned near the vertical centerline of the LCC test section with the test surface facing downward. The boundary layer was tripped via distributed roughness applied to the first 0.30 m of the model. Otherwise, the test surface was polished 304 stainless steel with a root-mean-square surface roughness of $k < 0.4$ μm, small enough for the surface to be considered hydro-dynamically smooth. The test surface was instrumented with a suite of flow measurement devices, as shown in Figure 1.

2.2. Polymer mixing and injection

The polymers used in this experiment were poly(ethylene oxide) (PEO or POLYOX) water-soluble resins manufactured by Dow Chemical Company: WSR-N-60K, WSR-301, and WSR-308. These polymers have manufacturer-supplied mean molecular weights, M_W, of approximately 2, 4, and 8 million, respectively. In the case of WSR-N60K, the manufacturer's mean molecular weight was checked by means of gel permeation chromatography (GPC) with light scattering detection (Vanapalli *et al.*, 2005, provides details of the methods used). The WSR–N60K measured M_w and polydispersity M_w/M_n were 2.3 x 10^6 g $mole^{-1}$ and 2.44 respectively. Attempts to assess the manufacturer-supplied molar mass of WSR-301, and WSR-308 by the same technique failed, the most likely reason being molecular aggregation (Vanapalli, 2006).

The raw polymers were provided as dry powders that must be hydrated before injection into the TBL. Such polymer solutions were prepared by sifting the powder into a jet of water filling a reservoir. An activated carbon filter (Model RT-2260-4, Aquapure Technologies) was used to remove chlorine from the water prior to mixing because of chlorine's potential for chemical degradation of PEO's drag reduction capability (Petrie *et al.*, 2003). After the initial wetting, the polymer solution was stirred in the 4.55 m^3 reservoir (Chem Systems, Inc.) with a 4-blade 0.75 *m* diameter impeller at 30 RPM until homogeneous; this process usually took 1 to 3 days. In addition, two small trolling motors were used near the reservoir surface to break-up and homogenize any remaining agglomerations. The effectiveness and repeatability of the mixing process and the stability of the polymer solutions were verified using a 4.57 *mm* diameter pipe-flow apparatus. The pressure drop along the pipe for a range of flow rates was used to characterize the behavior of the polymer solution. Such pressure-drop test results spanning 115 hours showed that the polymer remained stable over a period at least that long, and this is consistent with the reported observations of Ellis *et al.* (1972).

After hydration and mixing, the polymer was transferred to a smaller 1.140 m^3 tank which fed a low shear-rate, stainless steel progressive cavity pump (Moyno model 2E012G1SSQAAA-158587). This pump delivered the polymer to a manifold with 40 evenly spaced ports along the injector span. Inside the injector manifold, three layers of perforated plates and brass screens generated a pressure drop to ensure span-wise uniformity of the injection flow. The actual injector was a simple tapered slot – wider at its inlet, narrower at its outlet – oriented with mean angle of 25° with respect to the working surface and having an outlet gap of 1 *mm*. This injector is similar to one used in an optimization study by Walker *et al.* (1986).

The mixing, pumping, and flow upstream of the injector exit of the polymer solutions may all degrade the polymer unintentionally before it flows into the TBL. Vanapalli *et al.* (2005) conducted a series of experiments to determine the critical shear rate for degradation required to initiate degradation of the PEO polymer solutions. This relationship, presented in Section 4, is used to determine the critical shear rate for degradation. This degradation strain rate was then used as a constraint for the injection manifold design. In particular, care was taken to design the pumping, piping, and distribution systems such that the maximum shear rates were at least a factor of three below the critical value for degradation initiation. Moreover, samples of the polymers solutions that passed through the pumping, piping, distribution, and injection systems were collected at the injector exit, and their drag reducing potential was characterized from pressure drop measurements using the 4.57-*mm*-diameter pipe-flow apparatus. In all cases, the drag reducing properties of the delivered polymer were found to be unchanged from the polymer drawn from the upstream reservoir.

2.3. Experimental test matrix

A total of four independent parameters were varied throughout the polymer tests. There were three free-stream velocities, 6.65, 13.2, and 19.9 ms^{-1}. Three different PEO polymers having different values of M_W were used, and for each polymer, three solution concentrations were injected: 1000, 2000, and 4000 *wppm*. Lastly, polymer solutions were injected at three flow-rates corresponding to $Q_i = 0.14$, 0.28, and 0.71 $ls^{-1}m^{-1}$. Following established convention, the polymer solution flow-rate is normalized with a standard volume flux per unit span, $Q_s = 67.3\nu$, where ν is the kinematic viscosity of the free stream liquid. This value, established by Wu and Tulin (1972), is obtained by assuming a linear velocity profile and integrating the streamwise velocity over $0 < y^+ < 11.6$, where y^+ is the wall normal distance normalized with the viscous length $l_\nu = \nu\sqrt{\rho/\tau_w}$, ρ is the freestream liquid's kinematic viscosity, and τ_w is the TBL's wall shear stress. The three polymer flow rates in this study represent $Q_i/Q_s = 2, 4, 10$.

2.4. Test procedure

The friction drag reduction resulting from polymer injection was measured using the following procedure. First, a volume of polymer was prepared and staged for injection. The free-stream velocity of the water tunnel was brought to zero, and the skin-friction-drag sensors were electronically balanced and trimmed to zero output at the desired test section static pressure. Next, flow was initiated in the water channel, and when the desired free-stream velocity and static pressure were achieved, the baseline skin friction, τ_w, was measured. At this point polymer injection was initiated, and, after a transient period, the new reduced friction, $\tau_{w,i}$, was measured. When polymer injection was stopped, the baseline friction level returned after a period of time during which the highly viscoelastic polymer solution continued to be drawn from the injector in strands. In general, τ_w was recovered within a few tens of seconds or a few minutes after injection of polymer solution ceased.

The potential buildup of active polymer in the tunnel free-stream flow was monitored carefully. If the baseline shear stress after injection was reduced by more than 2%, a controlled amount of chlorine was added to the tunnel water to degrade the background polymer. The free chlorine is consumed as it reacts with the polymer, so the amount of chlorine added between runs was adjusted to leave only trace amounts of much less than 1 *ppm*. The background chlorine level was continually monitored to insure that an excess of chlorine did not occur. As a second measurement, samples of the tunnel water were removed periodically after large quantities of polymer were injected and tested in the aforementioned 4.57 *mm* diameter pipe flow apparatus to ensure that tunnel water mildly contaminationed with degraded, remnant polymer had the same pipe-flow pressure-drop characteristics as uncontaminated water. In addition, throughout the course of these multi-month tests, the entire LCC (5,300 m^3) was flushed and refilled on weekends when polymer had been used during the prior week.

2.5. Skin Friction Drag Balances

Direct skin-friction measurements were made at six stream-wise locations using floating-plate strain-gauge type friction drag sensors at the locations shown on Figure 1. The floating plate elements of the sensors were polished 17-4PH stainless steel, 15.2 *cm* in diameter, 0.79 *cm* thick. In each sensor, the floating plate was attached to the load-sensing element, a beryllium copper flexure instrumented with a full Wheatstone bridge of semiconductor strain gages. The plate and flexure were mounted within a bowl-shaped housing so that the plate and housing edge were flush with the model's test surface. The gap between the floating plate and housing was measured with feeler gauges to be 60 ± 20 μm, and varied slightly from sensor to sensor. The strain gages were excited at 7 VDC using signal-conditioning amplifiers (Model #2310, Vishay Measurements Group). The sensor outputs were amplified 500 fold and low-pass filtered at 100 Hz with the same Vishay units. The conditioned signals were recorded simultaneously at 50 Hz with a National Instruments NI-DAQ data acquisition board and a LabView virtual instrument. The typical data collection intervals were approximately one to three minutes.

The skin-friction sensors were calibrated using a four-point calibration from zero to two pounds with both increasing and decreasing loads and a second load cell (Model LCEB-5, Omega Engineering) mounted horizontally downstream of the friction balance. This second load cell was calibrated from zero to two pounds using weights. A thin cable tied between the second load cell and a suction cup on the floating plate element of the sensors was used to apply the load. The second load cell was mounted on a linear traverse used to increase or decrease the load on the sensor. This procedure eliminated friction problems associated with pulleys. The error associated with the sensor slope was taken to be twice the standard deviation of multiple calibration slopes (typically five or more) and varied between 0.8% and 2.9%. The zero-level of the load cells in the friction balances drifted with changes in free-stream temperature and pressure, so corrections were built into the calibration and data reduction process. The overall uncertainty in any particular time-averaged measurement of wall shear stress from one sensor was typically ± 5%.

For the present study, skin friction was measured to determine the drag reduction, *%DR*, obtained in polymer-laden flow:

$$\%DR = \frac{\tau_w - \tau_{w,i}}{\tau_w}, \qquad (2.1)$$

Here, sensor drift errors are largely eliminated because $\tau_{w,}$ and the steady shear stress measured during polymer injection, $\tau_{w,i}$, were measured within a few minutes of each other. Thus, the uncertainties for the reported $\%DR$ values are also ± 5% of the reported value.

2.6. Polymer concentration measurements

Planar Laser Induced Flourescence (PLIF) was used to measure the polymer concentration in the near-wall region of the TBL. Measurements were made at three stream-wise locations X-X_i = 0.64, 4.62, and 9.36 *m*, where X is the stream-wise distance downstream of the leading edge of the test model, and X_i is the stream-wise location of the injector slot. A known concentration of fluorescent dye (Rhodamine 6G supplied by Sigma Chemical) was thoroughly mixed into the injected polymer solutions. The dye-laden polymer solution was illuminated with a light sheet normal to the plate surface and aligned with the mean flow direction. Light sheets were formed from the beams of pulsed Nd-YAG lasers operating at the 532 nm wavelength and were measured to be ~125 *μm* thick at the plate surface. The plane of illuminated polymer and dye was imaged with a high-resolution camera (LaVision Imager Pro), where the field of view was approximately 5 *mm* (stream-wise) by 2 *mm* (wall-normal). Periscope prisms protruding 5 *mm* from the test surface were used to redirect the line of sight of the cameras housed in waterproof boxes inside the test model. The prism was located 4 *mm* from the light sheet. A long-pass optical filter was used to attenuate the original 532 *nm* light from the laser and return only the Stokes-shifted light from the fluorescent dye. Finally, a pair of cylindrical lenses was used to stretch the wall-normal component of the images by approximately a factor of 2.5. Further details are provided in Winkel *et al.* (2006).

The intensity of the light collected by the cameras was used to determine the polymer concentration via separate calibration measurements completed as follows. A calibration cell was filled with ~ 2500 cm^3 of dyed polymer solution and fitted onto the plate surface, immersing the light sheet and collection optics. A pump was used to slowly circulate the solution to prevent local heating of the liquid due to repeated laser pulses. The fluorescent return from these solutions was used to relate the intensity at each imaging pixel with the dye concentration, accounting for variations in light sheet intensity. As discussed below, the dilution level of the injected polymer solutions varied between factors of 10 and 1000, depending upon the experimental conditions and the measurement location. Hence, care was taken to set the initial dye concentration and calibration range such that the PLIF measurement at a particular location produced sufficient signal-to-noise ratio. However, it was usually not possible to select a single dye concentration that would result in acceptable measurements at all three PLIF measurement location, necessitating repeated experimental runs at multiple injected dye concentrations. The uncertainty of the PLIF measurements varied with the amount of dilution, but is typically ±20% for dilution of less than a factor of 100 of the initial concentration, and ±30% for dilutions greater than a factor of 100. Background light and electronic noise were the limiting factors for accurate large-dilution concentration measurements.

3. Baseline Flow Results

The baseline flow measurements from this experiment are summarized in Table 1 for the six skin-friction measurement locations ($X - X_i = 0.64, 2.09, 4.62, 6.11, 7.91, 9.36$ m), and the three PLIF measurement stations. Boundary layer growth on the model and test section side-walls caused a slight favorable pressure gradient along the plate; the three free stream test speeds – 6.65, 13.2, and 19.9 ms^{-1} – are valid for the nominal streamwise center of the plate. Full baseline boundary layer profiles were measured at the same locations as the third and sixth shear stress sensors with an LDV system. The local free stream velocity U, the 99% boundary layer thickness δ_{99}, and the momentum thickness Θ, inferred from these measurements, are listed in bold in Table 1. The remaining entries for U in Table 1 were inferred from static pressure measurements made along the plate and the steady Bernoulli equation. The remaining entries for δ_{99} and Θ in Table 1 were obtained from simple power-law fits to the LDV-profile-determined values of δ_{99} and Θ. In all cases, the values obtained from the fits were within a few percent of what would be obtained from standard flat-plate TBL formulae. In addition, Table 1 provides values for the downstream-distance-based Reynolds number, $\mathrm{Re}_x = Ux/\nu$, the skin friction coefficient, $C_f = \tau_w / \frac{1}{2}\rho U^2$, the acceleration parameter $K' = (\nu / U^2)(dU/dx)$, the friction velocity $u_\tau = (\tau_w / \rho)^{1/2}$, the viscous length l_ν, and the ratio, k^+, of the test-surface roughness height divided by l_ν. When $K' < 10^{-6}$, the flow acceleration should be sufficiently mild so that there will be little or no deviation in the boundary layer's profile from the typical log-law (Patel 1965); for the current experiments, $K' < 10^{-9}$. And, when $k^+ \leq 1$ or so, the plate surface can be considered hydro-dynamically smooth.

Baseline skin-friction coefficients measured in this experiment are shown in Figure 2 with the standard friction correlations of White (1991), Eq. (3.1), and Schultz-Grunow (1941), Eq. (3.2),

$$C_f = 0.455 \ln^{-2}\left(0.06\,\mathrm{Re}_x\right) \tag{3.1}$$

$$C_f = 0.370 \log^{-2.584}\left(\mathrm{Re}_x\right) \tag{3.2}$$

Skin-friction results from two separate tests conducted in 2004 and 2005, termed Phases III and IV, are provided to demonstrate the repeatability of the measurements. The measured skin-friction is approximately 5% below that predicted by White's correlation, but shows good agreement with the Schultz-Grunow correlation. A power-law curve fit (solid line) to the experimental data is also provided, given by

$$C_f = (0.0170 \pm 0.0004) \cdot \mathrm{Re}_x^{-(0.1237 \pm 0.0067)} \tag{3.3}$$

The Reynolds numbers given here employ the kinematic viscosity, $\nu = 9.95 \times 10^{-7}\ m^2 s^{-1}$, based on the average temperature of the water (20.4 °C). A complete presentation of the baseline flow measurements obtained during these experiments, including turbulence quantities and near-wall velocity measurements, is provided in Oweis *et al.* (2007).

4. Polymer Rheology

The rheology of high molar mass aqueous PEO solutions is complex. The relationship between the mechanical behavior of PEO solutions and the detailed characteristics and interactions of individual PEO molecules continues to be an active area of investigation (Vlassopoulous and Schowalter, 1994;

Kalashnikov, 1994; Tirtaatmadja *et al.*, 2006). For drag reduction, the most important characteristic of the high molecular weight polymer is its intermittent extension and relaxation in the turbulent flow. Treatments of polymer-laden turbulent flow have captured this physical process by means of various constitutive models of flow-polymer interactions. For example, the FENE-P (Finite Elastic Non-Linear Extensible-Peterlin) dumbbell constitutive model has been widely used because it incorporates the rheological effects of polymer finite extensibility in a computationally efficient way (Beris and Dimitropoulos, 1999; Housiadas and Beris, 2003; Dubief *et al.*, 2004; and Almeida *et al.*, 2006). The FENE-P dumbbell model relates the polymer stress tensor to the local, pre-averaged extension of the dilute polymer molecules. The distribution of length and orientation of the polymer molecules determines the polymer conformation tensor. The polymer stresses in the flow are then a function of the polymer conformation tensor. Molecular parameters in the FENE-P dumbbell model are the equilibrium polymer coil size, the maximum extensibility of the polymer molecule and the polymer concentration. These experimental parameters implicitly determine rheological quantities such as the zero-shear viscosity, the extensional viscosity and the polymer relaxation time (Dealy and Larson, 2006). Formally, the FENE dumbbell models are appropriate as a molecular description of dilute polymer solutions below the overlap concentration, c^*.

The solutions of high molecular PEO injected into the turbulent boundary layer in the present study were of molecular weight, M_w, 2.3, 4, and 8 million $g\ mole^{-1}$, and of concentrations 1000, 2000, or 4000 *wppm*. The intrinsic viscosity, $[\eta]_o$, of PEO solutions, in units of $cm^3\ g^{-1}$, can be determined from M_w using the Mark-Houwink relationship provided by Bailey and Callard (1959):

$$[\eta]_o = 0.0125 M_w^{0.78} \tag{4.1}$$

The dilute limit for polymer solutions is then determined by a common definition of the overlap concentration:

$$c^* = 1/[\eta]_o \tag{4.2}$$

Table 2 presents the results for the three PEO molecular weights used here. Note that the injected concentrations exceed c^* for all the conditions of this study, and there is a substantial portion of the flow where the concentration exceeds c^*. As the polymer mixes with the free-stream fluid, the concentration will be reduced, passing below c^* at some distance downstream of the injector.

The shear viscosity of the polymer solution is a function of polymer molecular weight, concentration, and shear rate. Kalashnikov (1998) provides a relationship for $\Delta = (\eta_0 - \eta_\infty)/\eta_\infty$, where η_0 and η_∞ are the limiting shear viscosities at zero and infinite shear rates:

$$\Delta = \left[\left(\frac{[\eta]_o}{136.6}\right)^2 + 0.434[\eta]_o - 126\right]C \tag{4.3}$$

where C is the concentration ($mg\ mg^{-1}$) and $[\eta]_o$ is the intrinsic viscosity ($cm^3 g^{-1}$), and the constants in (4.3) are dimensional. Table 2 lists the value Δ/C for injected solutions. In the low shear-rate regime, the shear viscosity of the highly concentrated injected solutions will be much higher than the solvent viscosity, but the solutions will undergo substantial shear thinning.

Kalashnikov (1998) also examined the polymer relaxation time for PEO solutions, and developed a relationship for θ_K for PEO solutions with $[\eta]_o > 280\ cm^3 g^{-1}$:

$$\theta_K = \left[\frac{[\eta]_o}{549.5} - \left(\frac{[\eta]_o}{3255}\right)^3 - 0.51\right] e^{-\left(\frac{T_c}{50}\right)^2} C^{1/2} \tag{4.4}$$

where T_C is the mixture temperature in °C. Kalashnikov (1998) reports that this relationship is generally valid over a range of concentrations of order 5 to 2000 *wppm* for a PEO solution with $[\eta]_o = 2650\ cm^3 g^{-1}$. Note, however, that the relaxation time goes to zero at zero concentration, and an alternate expression for the relaxation time, such as the Zimm time, θ_Z, should be used for very low concentrations. The Zimm time, appropriate for single molecules immersed in a good solvent, is:

$$\theta_Z = 0.422 \frac{[\eta]_O M_W \eta_S}{RT} \tag{4.5}$$

where R is the ideal gas constant (Dealy and Larson, 2006). Shin and Shaqfeh (2005) report relaxation times that are somewhat higher that those produced by the Kalashnikov relationship for WSR-301, but both groups report that the relaxation times of the concentrated polymer solutions are much larger that the Zimm time.

In a strong flow, flexible PEO molecules can experience a sufficient deformation rate to be oriented and extended. In turbulent flows, this condition is the onset deformation rate for friction drag reduction (Virk *et al.*, 1967). Although the detailed validity of the molecular interpretation as a coil-stretch transition is unclear above the overlap concentration, the onset condition is a useful quantifier in both conduit and boundary layer flows. This quantity has been characterized for varying aqueous concentrations of PEO; the data provided by Virk (1975) are used here to determine a dimensional relationship for the minimum shear rate for drag reduction onset, γ^* (Vanapalli *et al.*, 2005):

$$\gamma^* = (3.35 * 10^9) M_w^{-1} \qquad (4.6)$$

Another possible determinant of drag reduction behavior is polymer scission and degradation. Vanapalli *et al.* (2005) describe a series of experiments to determine the critical shear rate for degradation, γ_D, of PEO solutions.

$$\gamma_D = 3.23 * 10^{18} * M_w^{-2.20} \qquad (4.7)$$

where M_w is the molecular weight in $g\ mole^{-1}$, and γ_D is in s^{-1}. Table 2 presents these rheological parameters for the three polymer types used in this study.

A potential complication of assessing the polymer rheology is that the treatments discussed above are applicable to polymer chains described by a well-characterized molar mass. However, as discussed in the literature, high molar mass PEO is susceptible to intermolecular aggregation in aqueous solution (Dunlop, and Cox, 1977; Polverari and van de Ven, 1996; Faraone *et al.*, 1999; and Ho *et al.*, 2003). For the solutions considered here, the polymer molar mass is ill defined in the context of the above relationships. Moreover, the molar mass is difficult to characterize and is potentially a sensitive function of sample preparation and deformation history. If aggregation occurs as the polymer molar mass is increased above a certain value, then equations based on scaling (such as 4.6 and 4.7) will perform poorly. Vanapalli (2006) discusses light scattering observations that are suggestive of aggregation behavior in WSR-301. This observation is likewise consistent with the finding that WSR-301 relaxation times greatly exceed Zimm model predictions, even below the overlap concentration (Shin and Shaqfeh, 2005; Tirtaatmadja *et al.*, 2006). Keeping this important factor in mind, these relationships for the rheological properties of PEO will be used to help interpret results.

5. Drag Reduction Resulting From Polymer Injection

5.1. Stages of polymer mixing

Injection of polymer solution into the TBL results in a distribution of polymer across the boundary layer that evolves in the stream-wise direction. Poreh and Hsu (1972) describes four mixing stages: initial, intermediate, transition, and final. In the initial stage, the injected polymer is largely near the wall and within the sub-layer. In the intermediate stage, the polymer lies within a layer thinner than the boundary layer thickness but thicker that the viscous sub-layer and buffer layer. In the transition stage, the polymer is diffused throughout most of the TBL. In the final stage, the growth rate and thickness of the polymer-laden portion of the TBL is the same as that of the TBL itself. This process can be compared to the similarly defined mixing stages of a passive scalar, discussed by Poreh and Cermack (1964). Since the injected polymer flux is usually larger than Q_S, the layer of injected polymer is almost always thicker than the viscous sub-layer, and hence it is artificial to distinguish between the initial and intermediate stages as defined by Poreh and Cermack (1964). Therefore, these stages are combined herein and referred to this as the development stage. Although these stages are defined for the mixing process, the skin-friction drag reduction has a corresponding character in each of these regimes.

5.2. Drag reduction in the development stage

The concentration needed to achieve MDR varies with the molecular weight and other physical properties of the polymer and the topology and Reynolds number of the flow, but typical values for PEO at moderate to high Reynolds numbers range from 10 to 100 *wppm*. Consequently, injection of PEO solutions with concentrations on the order of 1000 *wppm* in the near wall region should result in MDR. Moreover, MDR should persist for a significant downstream extent after injection, possibly even into the transition stage of mixing, creating an extended zone or plateau of MDR some distance downstream of the injector. However, such an MDR plateau was not observed in these experiments. Instead, a region of increasing drag reduction immediately downstream of the injection location was observed, a phenomenon also noted in Petrie *et al.* (1996) and Petrie *et al.* (2005).

The length of the development region where the drag reduction is growing was observed to increase with increasing polymer M_W, C_i (concentration), and Q_i (injection rate), and with decreasing free-stream speed. In the present study, this development region was observed at distances exceeding 5 *m* for the lowest free-stream speed (6.65 ms^{-1}) at the highest M_W and injection rates. The development region was never observed at 19.9 ms^{-1} and only in two cases at 13.2 ms^{-1}. Two examples of the development region for the WSR-301 polymer are shown in Figure 3 which shows *%DR* defined by (2.1) as a percentage *vs*. distance downstream from the injector, $X - X_i$ (*m*).

Polymer concentration-field measurements show that the polymer is highly non-uniform in the development region and in many cases the polymer is observed in long filaments. In some cases, the polymer concentration field is nearly binary, essentially either the injected concentration C_i or nearly zero polymer concentration. Polymer solutions at high concentration have a very large extensional viscosity, and the polymer does not exit the injection slot in a two-dimensional sheet. Instead, the polymer is drawn from the injector by the high-speed water flow. This results in a region of highly intermittent polymer-water mixture. Also, the shear viscosity of the polymer solutions can be several times that of the pure water, and this can locally increase the skin friction near the injector, even though there may be a reduction in turbulent momentum transport. Lastly, the injected polymer solutions have relaxation times on the order of 0.1 seconds at concentrations near C_i. A finite extent of stream-wise flow is needed for the polymers to stretch, mix, and interact with the TBL turbulence. Moreover, once it has passed the injector, the boundary layer turbulence requires a finite time (or distance) to adjust to the new polymer-modified regenerative cycle that leads to high levels of drag reduction. Consequently, the maximum drag reducing potential of the polymer solution is reached some distance, perhaps several meters, downstream of the injector.

5.3. Maximum drag reduction

The maximum levels of drag reduction observed in the current tests are 70, 67, and 60 *%DR* at 6.65, 13.2, and 19.9 ms^{-1}, respectively. These levels of drag reduction are observed with the highest flux (C_i = 4000 *wppm*, $Q_i = 10Q_s$) of the highest M_W polymer (8 million), WSR-308, and are shown in Figure 4. The peak drag reduction was observed at the first measurement station ($X - X_i = 0.64$ *m*) only at 19.9 ms^{-1}. As discussed in the previous section, peak drag reductions occurred approximately 6 and 2 *m* downstream of the injector at 6.65 and 13.2 ms^{-1}, respectively. The maximum level of drag reduction observed in these experiments agrees with prior work. Vdovin and Smol'yakov (1981) observed maximum drag reduction between 65 and 70 percent for injection of WSR-301 solutions. Petrie *et al.* (1996) report maximum drag reduction between 64 and 67 percent for a maximum injection concentration of 2000 *wppm* WSR-301. As M_W increases, the amount of drag reduction that is achieved for a given value of Q_iC_i also increases. WSR-308 has an increase of around 1.1 times *%DR* compared to WSR-301, and both are higher than WSR-N60K by 10*%DR* to 20*%DR*. These differences are less than what is expected based solely on molecular weight or intrinsic viscosity, and this will be discussed further below.

5.4. Drag reduction in the transitional and final mixing regions

The transition and final mixing regions occur once the level of *%DR* peaks and begins to fall with increasing downstream distance (Poreh and Hsu 1972). Figures 4 and 5 illustrate how drag reduction decays with downstream distance from the injector. Warholic *et al.* (1999) suggested that aggregates play an important role in polymeric drag reduction. In their experiments they injected equivalent fluxes of polymer while varying the injected polymer concentration and injection rates. For equivalent fluxes of polymer, drastically larger drag reductions were observed with 500 *wppm* solution than 100 *wppm*, 45% *vs.* 19%, respectively. This indicates that the higher concentration polymer, where aggregates are more likely to occur, will be more effective at reducing drag. In contrast, results from the work of Vdovin and Smol'yakov (1978, 1981) indicate that the product of injection rate and concentration, Q_iC_i, will scale the drag reducing capacity of the injected solution. Results from the present experiment are shown in Figure 5 for two pairs of equivalent fluxes of WSR-301 at two concentrations. The present results indicate that the total polymer flux, Q_iC_i, is the primary factor. Since the experiments of Warholic *et al.* (1999) were performed in a relatively slow channel flow with speeds up to 2 ms^{-1}, the role of aggregation may have been more pronounced.

5.5. K-Factor scaling of the drag reduction

A simple scaling relationship for the observed drag-reduction based on the polymer injection, downstream distance, and flow-speed was developed by Vdovin and Smol'yakov (1981). They observed that the near-wall concentration decreased exponentially in the transition region, and proposed a scaling parameter that led to a reasonable collapse of their drag-reduction data. Their parameter, K, is given by

$$K = \frac{Q_iC_i}{\rho X_i U_\infty} \qquad (5.1)$$

where X_i is the distance from the line source ejecting the polymer. When the percentage of drag reduction, *%DR*, is plotted against K, data from the intermediate region show a logarithmic decrease in drag reduction with decreasing K (*i.e.* increasing X_i after fixing the other variables). Poreh and Hsu (1972) demonstrate that such behavior can be explained using a Lagrangian similarity hypothesis for mixing of the polymer in the logarithmic layer of the TBL, as first proposed by Batchelor (1957). The rate of mixing is related to the local friction velocity that, in turn, is a function of the near-wall polymer concentration. Consequently, the mixing rate is not expected to be a simple logarithmic relationship. Nevertheless, the K scaling has proven useful as a way of organizing and comparing *%DR* data, and it can help reveal some underlying flow processes.

Figure 6 presents *%DR vs.* K for the three polymers used. The development region is evident for higher values of K (*e.g.* the measurements closest to the injector). *%DR* grows and reaches a maximum near $K \sim 2\text{x}10^{-7}$, then decreases with decreasing K value (*e.g.* increasing distance from the injector). The product

Q_iC_i adequately collapses the data for a given speed, suggesting that it is the total flux of polymer that is the relevant quantity, whether it is slowly injected at high concentration or rapidly injected at low concentration, over the range of variables of these tests. However, the length of the initial region varies with free-stream speed, with the location of the peak drag reduction decreasing with increasing U. In turn, increasing M_W extends the development region and level of maximum drag reduction, with the differences between the low molecular weight polymer, WSR-N60K much more pronounced compared to the two higher molecular weight polymers, WSR-301 and WSR-308. Figure 7 illustrates the speed dependence of the K plots for WSR-301. The slopes of *%DR vs. K* for the transition region are similar, but the start of the transitional region varies with speed. Also plotted is a line representing the best-fit slope for the transitional regime reported by Vdovin and Smol'yakov (1981) for WSR-301.

The slopes of the present data are similar to this, although the length of the development region varies with speed. Table 3 describes the parameters and conditions under which the data were collected. Vdovin and Smol'yakov (1981) only report an overall range of speeds and do not distinguish their *%DR* data with their specific injection conditions and free-stream speed. Moreover, their stated aim was to examine the transitional region, and they avoided injection conditions that would lead to measurement of an initial and intermediate region, and do not report any data illustrating this regime. But, their data are similar in slope and maximum *%DR* to the low and medium speed data from the present study, along with the approximate K value for the beginning of the transition region.

Examination of other published results for WSR-301 also shows considerable variability. Figure 8 presents *%DR vs. K* for several experiments, sorted into low, medium, and high-speed investigations. Table 3 presents details on the experiments and how these data were collected. There is considerable spread in the plot, and the maximum drag reduction level varies considerably. Recall that in Fontaine *et al.* (1992) and Petrie *et al.* (2003), a relatively large drag balance was employed that could mask the initial region and peak level of drag reduction. Moreover, in Fontaine *et al.* (1992) and Petrie *et al.* (1996), the slot comprised only the middle 50% of the span. Span-wise diffusion of the polymer is likely limited near the injector and at higher concentration. However, as the polymer dilutes, spanwise mixing may take place, and this may be responsible for the steeper decrease in *%DR* with decreasing *K* for these data sets. Such change in slope between 30 *%DR* and 40 *%DR* can be discerned in the data from these experiments, although the scatter in the data makes definitive conclusions difficult. The low speed data are most scattered, and the location of peak drag reduction varies most. As the free-stream speed increases, *K* at maximum *%DR* increases, *e.g.* maximum *%DR* moves upstream. In the present experiments, the peak in *%DR* was not observed at the highest speed, since it occurred before the first shear-stress measurement station. The data of Petrie *et al.* (1996) and Petrie *et al.* (2005) appear to show a maximum in *%DR* near the injector, although it may also be a plateau. This variability in the *%DR vs. K* plots is not surprising, considering that the *K* parameter is essentially a similarity variable based on outer scales that does not incorporate the detailed physical processes involved in the different mixing zones. It is interesting to note that the logarithmic rate of decrease in *%DR* is similar for these cases, at least in the region of drag reduction greater than ~30 *%DR*, when the flow is in this transitional mixing region, and polymer is moving into the log-layer.

One should also consider the physical dimension of the initial mixing region in the present and previous experiments. In the present case, the peak of the drag reduction usually lays between the injector and the second measurement station, which was 2.09 meters from the injector. Table 3 shows the range of the development length, X_D defined as the distance between the injection and the location where $K = 2\text{x}10^{-7}$, for the range of Q_iC_i in each experiment at U = ~7 and ~20 ms^{-1}. For the smaller scale experiments, it is often not possible to resolve the longest initial regions at the lower speeds since X_D can extend beyond the farthest measurement location. In the present experiment, X_D is the largest at the lowest speed and highest Q_iC_i, and this distance is comparable to the experiments of Vdovin and Smol'yakov (1981) and about a meter longer than that reported by Petrie *et al.* (1996). At the highest free-stream speeds, X_D is reduced, and there is less spread in the *%DR vs. K* data from the different experiments. The *%DR vs. K* plots also reveal the end of the transition and final mixing zones, where the polymer has filled the boundary layer and mixes at a rate similar to that of a passive scalar. Here, the *%DR* has decreased to less than 10%. The *K* value at which transition to the final zone mixing occurs varies with M_w, but is generally between $2 \text{ x } 10^{-9} < K < 6 \text{ x } 10^{-9}$.

Variation in the geometry of the injection slots used in these studies as well as variation in the exit velocity of the injected polymer (typically 1% to 10% of the free-stream speed) did not appear to strongly influence the length of the initial region. Vdovin and Smol'yakov (1981) compared sampled polymer using a near tangential injector on a small (~1 meter long) flat plate (Vdovin and Smol'yakov, 1978) with the similar measurements on their larger-scale test. From these concentration measurements, they suggested that near-tangential injection of the polymer solution would be advantageous. However, Petrie *et al.* (2003) and Petrie *et al.* (2005) employed an injector with a near tangential exit, and the resulting drag reduction was not substantially different when compared to data obtained with finite angle slots, as evidenced by the comparative *%DR vs. K* plots. This observation is consistent with those of Walker *et al.* (1986) who reported that the developed drag reduction was not sensitive to changes in a slot injector angle between 15 and 25 degrees.

Finally, while *%DR vs. K* plots are helpful in organizing and studying the data from comparable experiments, it may be problematic to use these data to predict far beyond the parameters of the original experiments from which they are derived. Injection of very dilute or highly concentrated solutions, or injection at very high fluxes in excess of $10Q_s$, say, can produce different flows near the injector and mixing rates in the initial region, especially since very high injection fluxes may result in polymer solution being driven from the surface. Findings for the detailed mixing processes associated with the initial and transition regions are discussed next.

6. Evolution of the near-wall polymer concentration

6.1. Near-wall polymer concentration profiles

Measurements of the polymer concentration were made in the near-wall region at three stream-wise locations using pulsed laser induced fluorescence (PLIF). Examples of wall-normal profiles of the polymer at the first two PLIF measurement stations ($X - X_i = 0.64$ *m* and 4.62 *m*) are shown in Figure 9 for WSR-301, 6.65 ms^{-1}, and $Q_i = 10Q_S$. The sharpest concentration gradients near the wall occur at the first measurement station. Note that the peak polymer concentration does not occur at the wall, but a few hundred microns away. This phenomenon was only observed at the Station 1 at the lowest test speed. While an unintended artifact of the optical train may be suspected for this anomaly, this was not observed in the calibrations performed with uniform polymer/dye concentrations. Moreover, this phenomenon has also been observed by Brungart *et al.* (1991). They found peak concentrations occurred at $10 < y^+ < 50$ from the wall 0.12 m from the injector at 4.6 ms^{-1}. However, they ascribe this result to the varying index of refraction with polymer concentration. At the second and third measurement stations, the concentration profiles are much smoother and nearly uniform over the measurement volume $0 < y < 2$ mm. For the remaining diffusion analysis, the maximum concentration will be used which is often, but not necessarily the wall concentration.

Vdovin and Smol'yakov (1978 and 1981), Fontaine *et al.* (1996), Petrie *et al.* (1996), and Petrie *et al.* (2005) measured concentration across the boundary layer and discuss the evolution of the diffusion zone 50% thickness (λ,) relative to the boundary layer thickness, λ/δ_{99}, as a function of downstream distance from the point of injection. Sommer and Petrie (1992) also discuss the evolution of the concentration profile, $C(y)/c_M$, within the different mixing zones, where c_M is the maximum concentration in the near-wall region. The concentration measurements of the present experiments do not extend over the entire thickness of the polymer diffusion layer, but are limited to between 1% and 10% of the Newtonian boundary layer thickness, making the typical measured thickness much less than λ/δ_{99}.

6.2. Near-wall concentration vs. K

The scaling of polymer concentration as a function K is provided in Figure 10. As expected, the near wall concentration is reduced as K is reduced (*e.g.* as the distance from the injection location increases). This scaling produces a reasonable collapse of c_M, but the scatter increases if the data are normalized with the injection concentration, C_i. Most of the data collected at the second and third measurement stations are in the transitional and final mixing zones, while a few data points are collected in the initial region. (The data for WSR-N60K also includes data presented by Petrie *et al.*, 2005). There is considerable scatter in the data, but the data consistently suggest that, with increasing speed, c_M is reduced for a given value of K.

The experimental conditions of the present study are comparable to those of previously reported experimental studies of Fruman and Tulin (1976), Vdovin and Smol'yakov (1978) and (1981), Fontaine *et al.* (1992), and Petrie *et al.* (2005), presented in Table 3. As in the present work, these studies injected polymer solutions mixed with dye, and the polymer concentration is inferred from the dye concentration. However, in the first three references, the near wall flow was physically drawn from the test model and piped to a concentration measurement system. Fruman and Tulin (1976) discuss the proper selection of sampling flux, since it is important that only the near wall fluid be sampled. However, even if the proper boundary layer flux is prescribed, it is possible to erroneously sample the polymer solution, since the solution is highly non-Newtonian (Lotto and El Riedy, 1981). Hence, these indirect measurements of wall concentration are potentially less certain than those resulting from direct *in situ* PLIF interrogation. Moreover, it is unclear how Fruman and Tulin (1976) managed the build-up of background polymer and dye in their experiment. Nevertheless, we will include these measurements in our comparison with the present data as they illustrate the overall mixing process.

Figures 11 and 12 present the dimensional and normalized development of the near-wall concentration as a function of K. Three regimes of polymer mixing can be identified. The development region is characterized by a wall concentration that is decreasing as approximately $K^{0.2}$. At a value of $1 \times 10^{-7} < K < 2 \times 10^{-7}$, the wall concentration of the polymer begins to decrease at a must faster rate of $K^{2.7}$. This is the transitional mixing regime where the polymer is being mixed across the log-layer of the TBL. Once fully mixed across the TBL, the polymer is much more diluted and the level of drag reduction is much reduced. In the final mixing region, the near wall concentration reduces at the rate of TBL growth, $\sim K^{7/8}$. The data in Figure 12 are scattered, but the overall trends and dilution rates are remarkably similar. The data of Fruman and Tulin (1976) lie outside the general envelope of the data from more recent experiments, but it should be noted that these experiments employed relatively high polymer fluxes ($10 < Q_i/Q_S < 30$) and high injection velocities (10% to 40% of the free-stream speed) compared to the conditions of the other experiments shown in Table 4.

6.3. Mixing in the development region

The development region was not commonly measured in the present experiments, since its length was often less than the ~0.6 meters from the injector to the location of the first measurement station. However, we can infer the development length through examination of both the *%DR vs. K* plots and the c_M *vs. K* plots. Both show the start of the precipitous drop in *%DR* and c_M with decreasing K (*e.g.* increasing distance from the injector location) between $1\text{x}10^{-7} < K < 2\text{x}10^{-7}$, with the length being somewhat longer at lower speeds. This is consistent with the development of the 50% thickness of the concentration layer described by Petrie *et al.* (2003) and Petrie *et al.* (2005). They reported that the measured thickness of the concentration layer was typically much less than $\lambda/\delta_{99} = 0.1$, corresponding to the development region for $1\text{x}10^{-7} < K < 2\text{x}10^{-7}$. For $K < 1\text{x}10^{-7}$ the concentration thickness rapidly increases, with $\lambda/\delta_{99} > 0.5$ for $K < 10^{-8}$. The rate of polymer mixing is variable, but roughly corresponds to a rate of $K^{0.2}$, although the slope varies considerably.

The length of the development region depends on the mixing rate of the near-wall polymer flow formed downstream of the injector. If we consider the flow through the Newtonian boundary layer, a flux of Q_i/Q_S = 1 to 10 exists in a region of the fluid bounded by y^+ = 10 to 60, and the average velocity in the layer would be $5u_\tau$ to $12u_\tau$. This would make the initial layer have thicknesses on the order of 100 microns for the current experiment, and this is consistent with the near wall profiles of such as that shown in Figure 10. In this region the rate at which the near wall polymers mix into the TBL is the slowest immediately downstream of the injection location. Poreh and Zsu (1972) scale the mixing process as a diffusion layer with a characteristic length, $L_D = Uh^2/D_D$, where U is a velocity scale, h is the layer thickness, and D_D is a diffusivity. They show that mixing due to molecular diffusivity alone is much too low to be consistent with the observed mixing rates, and they suggest that the actual diffusivity is that of the near-wall turbulent flow. This assumption, however, implies a much higher rate of mixing and shorter development region than is typically observed.

The injected polymer forms a near-wall sheet in only the most general sense. Recall that the injected polymer solutions have relaxation times on the order of 10 milliseconds. The polymer need not exit the injector as a planar sheet, but is drawn from the slit as a result of the very high elasticity of the solution. The flow then strains the polymer, forming filaments, which will be discussed in Section 6.5. The relaxation times of the highly concentrated injected solutions are larger than the integral timescales of the flow, $\delta_{99}/U \sim 10^{-3}$ *s* near the injector. Hence, while the mean shear level near the wall is quite large, the high-concentration polymer solutions will not be easily deformed by the relatively high-frequency velocity fluctuations in the incoming TBL. Instead, the injected polymer will be strained by the mean near-wall shear flow.

Examination of the *K vs. %DR* plots indicates that the length of the development region, L_D, is approximately scaled with a *K* value of $K_D \sim 10^{-7}$, and the present data suggest that increasing speed decreases L_D and K_D. Nevertheless, the observation that the *K*-scaling is somewhat successful at scaling the length of the development region is revealing, since this supports the notion that the mixing processes in the initial region is grossly scaled with the outer variables of the TBL. We will return to the discussion of the mixing in the development region during the discussion of polymer filamentation.

6.4. Mixing in the transitional and final regions

The transitional region extends from roughly from $2\text{x}10^{-7} > K > 2\text{x}10^{-8}$. The mixing rate is not constant over this region, but roughly scales as $K^{2.7}$ (compared with the exponent of 2.5 reported by Petrie *et al.* (2005), for WSR-N60K.) Again, it is helpful to compare using *K vs. %DR* plots. Over this range of *K*, the drag reduction drops from its peak to around 10 to 20 *%DR*.

Vdovin and Smol'yakov (1978 and 1981), Fontaine *et al.* (1992) suggest that the polymer mixing process can be scaled for a given polymer type through determination of the “concentration decay length”, *L*, such that

$$\frac{C_M}{C_i} = e^{-X_I/L} \qquad (6.1)$$

where L is the *e*-folding distance (*i.e.* the length from the injection location to where the near-wall concentration falls to e^{-1} = 37% of the injected solution concentration). It has been supposed that L is a function of the injection parameters and the free-stream speed:

$$L = \frac{K_T Q_i C_i}{\rho U} \tag{6.2}$$

where K_T is a constant that is fixed for a given polymer-solvent combination and molecular weight. Data presented by Vdovin and Smol'yakov (1978 and 1981), Fontaine *et al.* (1992), and Petrie *et al.* (1996) indicate that $4.9\text{x}10^6 < K_T < 6.25\text{x}10^6$ for WSR-301 in water. If K_T is solely a function of polymer type, then K will be sufficient to scale the mixing processes. For this to be the case, the length of the development region must be small compared to L, since we are taking as our length the distance from the injector and not from the end of the development region. Also, we must assume that the mixing rate in linear with free-stream speed. The plot of c_M/C_i *vs.* K in Figure 12 shows an exponential decay in concentration after the development region, but the scatter in the data suggests that the decay length is not completely scaled with K. (Note that the data from Vdovin and Smol'yakov (1981) is re-plotted using a constant value of L derived from their best fit for K_T. We believe that the c_M/C_i data presented in their manuscript have been normalized by the specific value of L derived from *each individual experiment*. However, we are forced to use their best-fit value of L to re-plot their data. Therefore, the scatter in their data due to *variation* in L is not represented. Figure 1 of their manuscript suggests a variation in L of ±20%).

In the transitional mixing region, the wall concentrations decrease from 100's of *wppm* to around 10 *wppm*, but significant turbulence modification is still possible with concentrations as low as a few *wppm*. Finite levels of drag reduction are still observed. The mixing rate decreases in the final region, where the polymer has been diluted to less than 10 wppm and is largely mixed throughout the TBL, at $K \sim 10^{-8}$. The rate of concentration reduction scales with the growth of the TBL due to entrainment, with a growth rate of $\sim K^{7/8}$, which corresponds to the entrainment rate of a high Reynolds number TBL with little or no friction drag reduction. By $K \sim 10^{-9}$, the drag reduction has ceased, and the concentration has fallen to less than 1 *wppm*.

6.5. Filamentation of high concentration polymer solutions

The PLIF measurements of the near-wall concentration field often exhibited significant stratification. A layer of injected polymer was often observed near the wall, but the distribution of polymer was not necessarily uniform and continuous. Particular images would reveal the near absence of polymer near the wall with local, high concentration strands of polymer away from the wall. Vlachogiannis and Hanratty (2004) observed similar processes of polymer filamentation in their study of wall-injected polymer in a channel flow. They concluded that the presence of polymer filamentation resulted in enhanced drag reduction, and this, in turn may be due to the formation of polymer aggregates, as previously suggested by Cox *et al.* (1974). As discussed above, it is likely that there is substantial aggregation of the injected polymer solutions. The high elasticity of the injected solutions leads them to be drawn from the injector, which will introduce three-dimensionality to the near-wall polymer concentration distribution.

Examination of the PLIF images shows that for $K > 2.4 \times 10^{-7}$, the concentration field is very stratified, with large regions of nearly pure water and high concentrations of polymer filaments. Figure 13 shows three sample images. As the polymer diffuses from the filaments into the surrounding solvent, the background concentration of the polymer increases. Between $5 \times 10^{-8} < K < 2.4 \times 10^{-7}$, the near wall region consists of polymer filaments with a background of somewhat homogeneous polymer solution (Figure 14). . In this region the peak drag reduction has occurred and the mixing into the log-layer has commenced. Finally, with $K < 5 \times 10^{-8}$, the filaments have mixed into the flow and the concentration fields are nearly uniform throughout the field of view. The rheology of these highly stratified mixtures is potentially much more complicated than that of the uniform mixtures, but the relaxation time of the filaments will be on the order of that for the injected polymer solutions. As discussed in Section 6.3, the stretching and mixing of these filaments will then take place over outer flow length and time-scales that result in the development region, until the flow is sufficiently diluted and mixed to near-wall concentrations less than 100 *wppm*.

7. Relationship between polymer type, concentration, and the resulting drag reduction

7.1. Development of the Weissenberg number with flow conditions

We next consider how the observed drag reduction can be related to the polymer solution rheology and the near-wall flow of the TBL. The onset of drag reduction occurs when the near-wall shear rate exceeds γ^*. We can define a Weissenberg number for onset of drag reduction,

$$We^* = \frac{u_\tau^2}{\nu\gamma^*} \qquad (7.1)$$

Note that We* > 1 because onset scales on the magnitude of the fluctuating velocity gradient. These fluctuations are about an order of magnitude smaller than the turbulent scales used in (7.1) (Dimitropoulos *et al.*, 1998). The We* onset condition can be compared to the Weissenberg number based on the relaxation time of the polymer at the particular conditions of the experiment,

$$We^+ = \frac{\theta u_\tau^2}{\nu} \qquad (7.2)$$

where θ is the value provided by Kalashnikov (1998) for values above the Zimm time, which is the minimum value. Experiments in dilute polymer solutions indicate that onset typically occurs when the deformation rate in the flow exceeds a value necessary to stretch the long-chain polymers, and this corresponds to the onset value of We^+, resulting in a We^+ that is typically much greater than unity (Sreenivasan and White, 2000; Housiadis and Beris, 2003). Table 5 shows the spatial evolution of We^+ for WSR-301 for ranges of *K* that correspond to the development, transitional, and final mixing regions for the intermediate speed of 13.2 ms^{-1}. (Note that We^+ at any downstream location on the plate is a function of the local polymer concentration.) At these high values of Weissenberg number, the individual polymer molecules can achieve significant extension. For $We^+ \gg We^*$, polymer modification of the turbulence will become increasingly insensitive to further increases in We^+. This inequality appears satisfied for most experiments except the dilute flows of WSR-N60K at 6.65 ms^{-1}. These results are consistent with the findings of Housiadis and Beris (2003) who suggest that at these values of We^+, the flow will be in the low to moderate drag reduction regime. The flows with WSR-301 and WSR-308 both have sufficiently high

We$^+$, and these flows are in the high drag reduction regime for all but the most dilute (*i.e.* downstream) portions of the flow.

Finally, the potential for polymer degradation can be evaluated using (4.7) with the definition of the degradation Weissenberg number, We$_D$

$$We_D = \frac{u_\tau^2}{\nu\gamma_D} \tag{7.3}$$

Significant levels of polymer degradation are expected when We$_D$ >> 1, which is likely to occur with the present flow.

7.2. Comparison of observed and expected levels of drag reduction with varying M_W

With the data presented above, we can construct the universal drag reduction curves for the flow over the plate. These curves can be used to determine the intrinsic drag reduction and concentration of a particular polymer, quantities that were introduced for pipe-flows by Virk *et al.* (1967). Figure 15 shows $\%DR/c_M$ as a function of c_M for the three polymer molecular weights. The intrinsic drag reduction $[\%DR/c_M]$ and intrinsic concentration $[C]$ was determined as a result of a best fit of the data to a function of the form

$$\%DR / c_M = \frac{[\%DR / c_M]}{1 + c_M / [C]} \tag{7.4}$$

Table 6 presents the values for each molecular weight at each test speed and an average curve fitted to the data from of all of tested speeds. The data are scattered at the lowest concentrations, but some trends are apparent. First, the lowest molecular weight polymer, WSR-N60K, has much lower intrinsic drag reduction values than WSR-301. The average intrinsic drag reduction of WSR-N60K is ~5 times less than that of WSR-301. The average intrinsic drag reduction of WSR-308 is ~1.2 times that of WSR-301.

The relationship between the intrinsic drag reduction and the underlying polymer rheology is not readily apparent; however, qualitatively we see that this quantity is more influenced by the drag-reducing polymer than the flow speed. The existence of the intrinsic drag reduction from the functional form of 7.4 implies dilute solution behavior, as evidence by the low concentration plateaus in Figure 15. Thus, we might expect that [$\%DR/c_M$] would scale with the Zimm relaxation time (or some multiple thereof), but examination of Table 2 shows that the θ_Z for WSR-301 is ~2.7 times that of WSR-N60K, and θ_Z for WSR-308 is ~3.4 times that of WSR-301. Thus, consideration of the Zimm time alone is not sufficient to scale these results. Use of the Kalashnakov relaxation time introduces two further complications. First, this relationship is valid for relatively high concentrations. Tirtaatmadja *et al.* (2006) discuss the influence of molecular weight and concentration on the relaxation time for PEO solutions in good solvents. They showed that, for solutions with $C/c^* < 10^{-2}$, the relaxation time approaches the Zimm time. In regimes where the concentration is $C/c^* > 10^{-2}$, we can use the Kalashnikov relaxation time to compare the performance of the polymer solutions. This corresponds to concentrations of approximately 5 *wppm* and above. Second, $\theta_K \sim \sqrt{C}$ which would not lead to a constant value of the intrinsic drag reduction in the limit as $C \to 0$, a result that appears inconsistent with the data from Figure 15.

Virk *et al.* (1967) reported a phenomenological relationship between the intrinsic drag reduction and intrinsic viscosity, where

$$[\%DR / c_M] \sim [\eta]_o^3 \ln(We^*) \tag{7.5}$$

The changing free-stream speed will lead to slight variation in We*. For example, changing the speed from 6.65 ms^{-1} to 13.2 ms^{-1} increases ln(We*) by ~1.3 for all three polymers. Similarly, further changing the speed from 13.2 ms^{-1} to 19.9 ms^{-1} increases ln(We*) by ~1.2. Combining these results with Eq. 4.1, the scaling of Eq. 7.5 implies that WSR-301 would be ~4.6 as effective at WSR-N60K, and WSR-308 would be ~6.3 times as effective as WSR-301. This empirical scaling appears to capture the difference in the intrinsic drag reduction between WSR-301 and WSR-N60K. But, the intrinsic performance of the dilute WSR-308 solutions is much less than predicted. We argue that an important contributing factor to this discrepancy is the process of flow-induced polymer degradation.

The intrinsic drag reduction tends to decrease with increasing speed, and these changes are more pronounced with increasing molecular weight. Examination of We_D for the 13.2 ms^{-1} conditions in Table 5 indicates that all the polymers are potentially susceptible to degradation, with WSR-308 being the most likely to degrade. Vanapalli *et al.* (2005) has shown that high molecular weight PEO solutions like WSR-308 undergo significant degradation in turbulent shear flow for $We_D >> 1$. Continued exposure to flows with sufficient stretch for scission results in continual reduction in M_W, until the polymer molecules are sufficiently shortened that they become scission resistant at the given deformation rate of the flow. Degradation of WSR-308 will result in a polymer solution that behaves more like WSR-301, as seen in the present study.

The observation that the intrinsic drag reduction decreases with speed is consistent with the presence of increased degradation at high speeds and higher M_W for a given speed. Thus, under the conditions of the present study, the flow in the TBL will continually degrade polymer molecules, reducing the mean molecular weight of the polymers in solution. (Note that scission of the molecules will increase the *number* of lower M_W molecules, but maintain a *constant* mass-fraction concentration). Vanapalli *et al.* (2006) analyzed the scaling of polymer scission in wall-bounded turbulent shear flow and show that the bulk of the polymer degradation takes place in the log-layer of the TBL, since this is where the appropriate combination of volume flux and shear rate is highest. Consequently, the *rate* at which the polymers degrade is expected to be a function of numerous flow parameters, including both the inner and outer scales of the TBL, and the distribution of polymer within the TBL. The data presented here suggest that the stream-wise extent of the test model used in the current study was sufficiently long to reveal the presence of significant polymer degradation for the higher molecular weight polymers. Note that the most dilute polymer solutions occurred farthest downstream from the injector, and the polymers solutions there have had the longest exposure to the turbulent flow.

Examining the intrinsic drag reduction of WSR-308 reveals that $[\%DR/c_M]$ is much higher at the lowest speed and is about twice that of WSR-301 under equivalent conditions (although the data are sparse). These low-speed results illustrate that WSR-308 *can* achieve a higher intrinsic drag reduction if the level of degradation is reduced. However, as the flow speed is increased, the rate of degradation becomes substantial, and the drag reduction achieved by the degraded WSR-308 approaches that of WSR-301.

8. Conclusions

A set of experiments has been conducted at the Large Cavitation Channel (LCC) in Memphis, Tennessee to investigate the phenomena of friction drag reduction at large scales and high Reynolds numbers in a controlled test environment. Drag reduction was achieved by injecting aqueous solutions of poly(ethylene oxide) (PEO) of three different molecular weights into the nearly zero-pressure-gradient turbulent boundary layer on a smooth flat-plate test model. The measurements covered more than nine meters of flow development length downstream of the injector at free stream flow speeds up to 20 ms^{-1}.

With sufficiently large mass flux of injected polymer, maximum drag reduction (MDR) was reached over a limited extent of the test model surface. However, a plateau at MDR was not observed. Instead, a development region near the injector produced a broad peak in drag reduction where MDR was nearly achieved, then the continued process of mixing led to a steady decrease in the level of drag reduction. Increasing polymer molecular weight resulted in higher levels of drag reduction, as did increasing the net polymer flux injected into the TBL. These results were collected at high Reynolds numbers and large physical scales, and they are broadly consistent with previously reported results acquired on smaller test models and at lower speeds.

The process of polymer mixing in the TBL can be broadly divided into three regimes: the development region, the transitional region, and the final region. The development region occurs just downstream of the injection location. The highly viscoelastic polymer solutions are stretched and mixed into the TBL, forming a stratified mixture of polymer and solvent. As this mixing process occurs, the friction drag reduction increases to its peak value. The rate of polymer mixing in the development region is relatively slow. However, as the polymer begins to mix across the TBL in the transitional regime, the mixing rate dramatically increases. Mixing-induced dilution of the polymer reduced the level of friction drag reduction. And, in the final region, polymer dilution is due to entrainment of free-stream liquid into the

TBL. At best these mixing processes are adequately scaled with the *K*-Factor, a parameter that includes the injected polymer flux, free-stream speed, and distance from the injection location. By injecting high-concentration polymer solution, a relatively long development region was produced. However, the length of this high drag reduction never extended over the entire test model.

The drag reducing performance of the polymers increased with increasing weight concentration and molecular weight of the polymer solution. However, the level of drag reduction for a given near wall polymer concentration was reduced with increasing speed. And, the highest molecular weight solutions produced, on average, levels of drag reduction that were only modestly higher than solutions with one-half the molecular weight. These observations are consistent with the presence of flow-induced degradation, a process that was expected to occur based on the known molecular scission potential of the PEO solutions used. Attempts to scale the observed intrinsic drag reduction with changes in PEO molecular weight were not successful, suggesting that the solution intrinsic viscosity alone is not sufficient to scale the observed levels of drag reduction in the diluted polymer solutions. We hypothesize that the presence of significant polymer degradation will lead to a failure of such simple scalings. Moreover, the relationship between the solution relaxation time, concentration, and resulting turbulence modification may be too complex for such simple scaling ideas, especially in regions of high drag reduction. Future study is needed to resolve this issue.

Acknowledgements

The authors would like to acknowledge significant contributions to this work from our colleagues at Michigan, the Naval Surface Warfare Center, and the overall DARPA Friction Drag Reduction Program. We would like to acknowledge the helpful discussions we had with many members of the DARPA Friction Drag Reduction Program, with special thanks to Mr. Duncan Brown and Dr. Howard Petrie. This work was supported by DARPA under contract number HR0011-04-1-0001, Dr. Thomas Beutner, Program Manager. The content of this document does not necessarily reflect the position or policy of the United States Government, and no official endorsement should be inferred.

References

Almeida, T. G., Walker, D. T., Leighton, R. I., Alajbegovic, A., Pankajakshan, R., Taylor, L. K., Whitfield, D. L., and Ceccio, S. L., 2006, "A Reynolds-Averaged Model for the Prediction of Friction Drag Reduction by Polymer Additives", *Proc. 26th Symp. on Naval Hydrodynamics*, Rome

Bailey, F. E. and Callard, R. W., 1959, "Some Properties of Poly(ethylene oxide) in Aqueous Solutions", *Journal of Applied Polymer Science*, **1**(1), 56-62.

Batchelor, G. K., 1957, "Diffusion in Free Turbulent Shear Flows", *Journal of Fluid Mechanics*, **3**(1), 67-80.

Beris, A. and Dimitropoulos, C., 1999, "Pseudospecrtral Simulation of Turbulent Viscoelastic Channel Flow", *Computer Methods in Applied Mechanics and Engineering*, **180**, 365-392.

Cox, L. R., Dunlop, E. H., and North A. M., 1974, "Role of Molecular Aggregates in Liquid Drag Reduction by Polymers", *Nature*, **249**(5454), 243-245.

Dealy, J. M. and Larson, R. G., 2006, *Structure and Rheology of Molten Polymers*, Hanser Gardener Publications, Cincinnati.

Dubief, Y., White, C. M., Terrapon, V. E., Shaqfeh, E. S. G., Moin, P., and Lele, S. K., 2004, "On the Coherent Drag-Reducing and Turbulence-Enhancing Behaviour of Polymers in Wall Flows", *Journal of Fluid Mechanics*, **514**, 271-280.

Dunlop, E. H. and Cox, L. R., 1977, "Influence of molecular aggregates on drag reduction," *Physics of Fluids*, **20**, S203-S213.

Ellis, A. T., Ting, R. Y., and Nadolink, R. H., 1972, "Some Storage and Shear history Effects on Polymeric Friction Reduction", *Journal of Hydronautics*, **6**(2), 66-69, Etter R. J., Cutbirth, J. M., Ceccio, S. L., Dowling, D. R., Perlin, M., 2005, "High Reynolds Number Experimentation in the U. S. Navy's William B. Morgan Large Cavitation Channel", *Measurement Science and Technology*, **16**(9), 1701-1709.

Faraone, A., Magazu, S., Maisano, G., Migliardo, P., Tettamanti, E., and Villari, V., 1999, "The puzzle of poly(ethylene oxide) aggregation in water: Experimental findings," *J. of Chemical Physics*, **110**, 1801-1806.

Fontaine, A.A., Petrie, H.L. & Brungart, T.A., 1992, "Velocity profile statistics in a turbulent boundary layer with slot-injected polymer", *Journal of Fluid Mechanics*, **238,** 435-466.

Fruman, D. H. and Tulin, M. P., 1976, "Diffusion of a Tangential Drag-Reducing Polymer Injection on a Flat Plate at High Reynolds Number", *Journal of Ship Research*, **20**(3), 171-180.

Jimenez, J. and Pinelli, A., "The autonomous cycle of near-wall turbulence," *Journal of Fluid Mechanics*, **389**, 335-359.

Kalashnikov, V. N. 1994, "Shear-rate dependent viscosity of dilute polymer solutions," *J. Rheology*, **38**, 1385-1403.

Kalashnikov, V. N., 1998, "Dynamical Similarity and Dimensionless Relations for Turbulent Drag Reduction by Polymer Additives", *Journal of Non-Newtonian Fluid Mechanics*, **75**, 209-230.

Ho, D. L., Hammouda, B., and Kline, S. R., 2003, "Clustering of poly(ethylene oxide) in water revisited," *J. of Polymer Science Part B-Polymer Physics*, **41**, 135-38.

Horn, A. F. and Merrill, E. W., 1984, "Midpoint scission of macromolecules in dilute solution in turbulent flow", *Nature*, **312**, 140-141.

Housiadas, K. D. and Beris, A. N., 2003, "Polymer Induced Drag Reduction: Effects of the Variations in Elasticity and Inertia in Turbulent Viscoelastic Channel Flow", *Physics of Fluids*, **15**(8), 2369-2384.

Larson, R. G., 2003, "Analysis of polymer turbulent drag reduction in flow past a flat plate", *Journal Non-Newtonian Fluid Mechanics.*, **111**, 229-250.

Lotto, B. and El Riedy, O. K., 1981, "Effects of Sampling Rate on Concentration Measurements in Nonhomogeneous Dilute Polymer Solution Flow", *Journal of Rheology*, **25**(6), 583-590.

Oweis, G. F., Winkel, E. S., Cutbirth, J. M., Ceccio, S. L., Perlin, M., and Dowling, D. R., "Smooth-Flat-Plate Turbulent Boundary Layer Measurements at High Reynolds Number," *Journal of Fluid Mechanics*, (to be submitted in 2007).

Patel, V. C., 1965, "Calibration of the Preston Tube and Limitations on its use in Pressure Gradients", *Journal of Fluid Mechanics*, **23**, 185-208.

Petrie, H. L., Brungart, T. A., and Fontaine, A. A., 1996, "Drag Reduction on a Flat Plate at High Reynolds Number with Slot-injected Polymer Solutions", *Proceedings of the ASME Fluids Engineering Division*, **237**, 3-9.

Petrie, H. L. and Fontaine, A. A., 1996, "Comparison of Turbulent Boundary Layer Modifications with Slot-injected and Homogeneous Drag-reducing Polymer Solutions", *Proceedings of the ASME Fluids Engineering Division*, **237**, 205-210.

Petrie, H. L., Deutsch, S., Brungart, T. A., and Fontaine, A. A., 2003, "Polymer Drag Reduction with Surface Roughness in Flat-Plate Turbulent boundary Layer Flow", *Experiments in Fluids*, **35**, 8-23.

Petrie, H., Fontaine, A., Money, M., and Deutsch, S., 2005, "Experimental Study of Slot in Injected Polymer Drag Reduction", *Proceedings of the 2nd International Symposium on Seawater Drag Reduction*, Busan, 605-620.

Polverari, M. and van de Ven, T.G.M., 1996, "Dilute aqueous poly(ethylene oxide) solutions: Clusters and single molecules in thermodynamic equilibrium," *J. of Physical Chemistry*, **100**, 13687-95.

Poreh, M. and Cermak, J. E., 1964, "Study of Diffusion From a Line Source in a Turbulent Boundary Layer", *International Journal of Heat and Mass Transfer*, **7**(10), 1083-1095.

Poreh, M. and Hsu, K. S., 1972, "Diffusion of Drag Reducing Polymers in a Turbulent Boundary Layer", *Journal of Hydronautics*, **6**(1), 27-33.

Ptasisnski, P. K., Boersma, B. J., Nieuwstadt, F. T., M., Hulsen, M. A., van den Brule, A., and Hunt, J. C. R., 2003, "Turbulent Channel Flow Near Maximum Drag Reduction: Simulations, Experiments and Mechanisms", *Journal of Fluid Mechanics*, **490**, 251-291.

Sanders, W. C., Winkel, E. S., Dowling, D. R., Perlin, M., and Ceccio, S. L., 2006, "Bubble Friction Drag Reduction in a High-Reynolds number Flat-Plate Turbulent Boundary Layer", *Journal of Fluid Mechanics*, **552**, 2006, 353-380.

Schultz-Grunow, F., 1941, "New Frictional Resistance Law for Smooth Plates", *NACA Technical Memorandum*, **17**(8), 1-24.

Sellin, R. H. J., 1982, "The Effect of Drag-reducing Additives on Fluid Flows and their Industrial Applications Part 2: Present Applications and Future Proposals", *Journal of Hydraulic Research*, **20**(1), 29-69.

Shin, M. and Shaqfeh, E. S. G., 2005, "Viscoelastic Turbulent Boundary Layer with Near-wall Injection of Polymer Molecules", *Center for Turbulence Research Annual Research Briefs*, Stanford University.

Sreenivasan, K. R. and White, C. M. 2000, "The Onset of Drag Reduction By Dilute Polymer Additives, and the Maximum Drag Reduction Asymptote", *Journal of Fluid Mechanics*, **409**, 149-164.

Tirtaatmadja, V., McKinley, G. H., and Cooper-White. J. J., 2006, "Drop formation and breakup of low viscosity elastic fluids: Effects of molecular weight and concentration," *Physics of Fluids* **18**, 043101

Vanapalli, S. A., 2007, "Polymer Chain Scission in Extensional and Turbulent Flows and Implications for Friction Drag Technologies," Ph.D. dissertation, University of Michigan.

Vanapalli, S. A., Islam, M. T., and Solomon, M. J., 2005, "Scission-induced bounds on maximum polymer drag reduction in turbulent flow", *Physics of Fluids*, **17**,1-11.

Vanapalli, S. A., Ceccio, S. L., and Solomon, M. J., 2006, "Universal scaling for polymer chain scission in turbulence", *Proceedings of the National Academy of Science*, **103**(45), 16660-16665.

Vlassopoulous, D. and Schowalter, W. R., 1994, "Steady viscometric properties and characterization of dilute drag-reducing polymer solutions," *J. Rheology*, **38**, 1427-1446

Virk, P. S., Merrill, E. W., Mickley, H. S., Smith, K.A., and Mollo-Christensen, E. L., 1967, "The Toms Phenomenon: Turbulent Pipe Flow of Dilute Polymer Solutions", *Journal of Fluid Mechanics*, **30**(2), 305-328.

Virk, P. S., Mickley, H. S., and Smith, K. A., 1970, "The ultimate asymptote and mean flow structure in Toms' phenomenon", *Transactions of the ASME Journal of Applied Mechanics*, **37**(2), 488-493.

Virk, P. S., 1975, "Drag Reduction Fundamentals", *Journal of the American Institute of Chemical Engineers*, **21**(4), 625-656.

Vdovin, A. V. and Smol'yakov, A. V., 1978, "Diffusion of Polymer Solutions in a Turbulent Boundary Layer", *Journal of Applied Mechanics and Technical Physics*, **19**(2), 66-73.

Vdovin, A. V. and Smol'yakov, A. V., 1981, "Turbulent Diffusion of Polymers in a Boundary Layer", *Journal of Applied Mechanics and Technical Physics*, **22**(4), 98-104.

Vlachogiannis, M. and Hanratty, T. J., 2004, "Influence of wavy structured surfaces and large scale polymer structures on drag reduction", *Experiments in Fluids*, **36**, 685-700.

Walker, D. T., Tiederman, W. G., and Luchik, T. S., 1986, "Optimization of the injection process for drag-reducing additives", *Experiments in Fluids*, **4**, 114-120.

Winkel, E. S., Oweis, G., Vanapalli, S.A., Dowling, D. R., Perlin, M., Solomon, M. J., and Ceccio, S. L., 2006, "Friction Drag Reduction at High Reynolds Numbers with Wall Injected Polymer Solutions", *Proceedings of the 26th Symposium on Naval Hydrodynamics*, Rome.

Warholic, M. D., Massah, H., and Hanratty, T. J., 1999, "Influence of Drag-reducing Polymers on Turbulence, Effects of Reynolds Number, Concentration, and Mixing", *Experiments in Fluids*, **27**, 461-472.

White, C. M., Somandepalli, V.S.R., and Mungal, M. G., 2004, "The turbulence structure of drag reduced boundary layer flow", *Experiments in Fluids*, **36**, 62-69.

White, F. M., 1991, *Viscous Fluid Flow*, McGraw Hill, New York.

Wu, J. and Tulin, M. P., 1972, "Drag Reduction by Ejecting Additive Solutions into Pure-Water Boundary Layer", *Journal of Basic Engineering, Transactions of the ASME*, **94**, 749-756.

Table 1: Single phase free-stream velocity U, Reynolds number $\mathbf{Re}_X$, 99% boundary layer thickness δ_{99}, momentum thickness Θ, acceleration parameter K', skin friction coefficient C_f, the friction velocity u_τ, the viscous length l_ν, and the surface roughness parameter k^+, at the downstream locations of the injector, the six skin-friction measurement balances, and the three PLIF measurement stations.

	X/L	$X\text{-}X_i$ (m)	U (ms^{-1}) ±1%	$\mathbf{Re}_X$ x 10^6	δ_{99} (mm) ±10%	Θ (mm) ±5%	K' x 10^{10}	C_f ± 0.0001	u_τ (ms^{-1})	l_ν (μm)	k^+
Injector	0.10	0	6.57	8.7	18	2.2	7.3	0.0024	0.23	4.4	0.1
			13.11	17	17	1.9	3.7	0.0022	0.43	2.3	0.2
			19.75	26	15	2.0	2.4	0.0021	0.63	1.6	0.3
Sensor 1	0.15	0.64	6.58	13	25	2.8	7.3	0.0023	0.22	4.5	0.1
MS1			13.13	26	23	2.6	3.7	0.0021	0.42	2.4	0.2
			19.78	39	21	2.1	2.4	0.0020	0.62	1.6	0.2
Sensor 2	0.26	2.09	6.60	23	38	4.0	7.2	0.0021	0.22	4.6	0.1
			13.18	45	35	3.6	3.6	0.0019	0.41	2.5	0.2
			19.85	67	34	3.6	2.4	0.0018	0.60	1.7	0.2
Sensor 3	0.46	4.62	**6.65**	40	**58**	**5.7**	7.2	0.0020	0.21	4.8	0.1
MS2			**13.25**	79	**55**	**5.3**	3.6	0.0018	0.40	2.5	0.2
			19.93	119	**54**	**5.2**	2.4	0.0017	0.58	1.7	0.2
Sensor 4	0.58	6.11	6.66	50	68	6.5	7.2	0.0019	0.21	4.8	0.1
			13.30	99	65	6.1	3.6	0.0017	0.39	2.5	0.2
			20.03	150	65	6.0	2.4	0.0017	0.58	1.7	0.2
Sensor 5	0.72	7.91	6.69	62	81	7.5	7.2	0.0019	0.20	4.9	0.1
			13.35	124	77	7.1	3.6	0.0017	0.39	2.6	0.2
			20.11	187	78	6.9	2.4	0.0016	0.58	1.7	0.2
Sensor 6	0.83	9.36	**6.70**	72	**90**	**8.2**	7.1	0.0018	0.20	5.0	0.1
MS3			**13.39**	144	**86**	**7.8**	3.6	0.0017	0.39	2.6	0.2
			20.22	217	**88**	**7.5**	2.4	0.0016	0.57	1.8	0.2

Table 2: Polymer Solution Properties.

PEO Polymer	M_w ($g\ mole^{-1}$)	$[\eta]_o$ ($cm^3 g^{-1}$)	c^* ($wppm$)	Δ/C ($wppm^{-1}$)	θ_Z (s)	$\theta_K/C^{1/2}$ (s)	γ^* (s^{-1})	γ_D (s^{-1})
WSR-N60K	2.3×10^6	1.1×10^3	8.7×10^2	4.4×10^2	4.6×10^{-4}	1.30	1.5×10^3	2.4×10^4
WSR-301	4×10^6	1.8×10^3	5.7×10^2	8.1×10^2	1.2×10^{-3}	2.17	8.4×10^2	7.1×10^3
WSR-308	8×10^6	3.0×10^3	3.3×10^2	1.7×10^3	4.2×10^{-3}	3.58	4.2×10^2	1.5×10^3

Table 3: Experimental setup and conditions of previous experiments reporting drag reduction *vs.* K-Factor for line-source injection into a turbulent boundary layer using WSR-301.

	TBL Thickness at Injector *(mm)*	**Maximum Measurement Distance from the Injector** *(m)*	**Speed Range** (ms^{-1})	**Conc. Range** *(wppm)*	Q_i/Q_s	**Balance Type**	**Injector Type**	**Injector Span (% of total)**	X_D **K=2x10^{-7} U = 6.7 ms-^{1}** *(m)*	X_D **K=2x10^{-7} U = 20 ms-^{1}** *(m)*
Vdovin and Smol'yakov (1981)	8 to 50	4.375	2.5 to 10	250 to 4000	1.1 to 23	Local (20 mm x 20 mm)	20 degree slot (0.4 x 140 mm or 0.8 x 140 mm)	87%	0.02 to 5.16	0.01 to 1.72
Fontaine *et al.* (1992)	~4*	0.36 to balance trailing edge	4.5 to 18.3	500 and 1000	1.6 to 4	Integrated (318 x 152 mm)	25 degree slot (1 mm x 152 mm)	50%	0.05 to 0.22	0.02 to 0.08
Petrie *et al.* (1996)	~10 to ~20**	1.87	7.6 to 16.8	500 to 2000	2.5 to 10	Local (38 x 127 mm)	25 degree slot (2.5 mm x 610 mm)	50%	0.07 to 1.12	0.02 to 0.37
Petrie *et al.* (2003)	~4*	0.38 to balance trailing edge	4.57 to 13.7	200 to 2000	2 to 20	Integrated (318 x 152 mm)	Contoured Plenum Slot	81%	0.02 to 2.24	0.01 to 0.75
Petrie *et al.* (2005)	~4*	0.33	6 to 18	100 to 500	2 to 20	Local (38 x 127)	Contoured Plenum Slot	81%	0.01 to 0.56	0.00 to 0.19
Present Results	16 to 20	9.36	6.6 to 20	1000 to 4000	2 to 10	Local (152.4 mm diameter)	25 degree slot (1 mm exit cross section x 2650 mm)	88%	0.11 to 2.04	0.04 to 0.75

* reported by Madavan *et al.* (1985); ** estimated assuming the origin of the TBL is the model leading edge

Table 4: Experimental setup and conditions of previous experiments reporting near-wall concentration measurements for line-source injection into a turbulent boundary layer using WSR-301 and WSR-N60K (present results and Petrie *et al.*, 2005).

	Maximum Measurement Distance From the Injector *(m)*	**Speed Range** *(ms^{-1})*	**Conc. Range** *(wppm)*	Q_i/Q_s	**Measurement Method**	**Injector Type**	**Injector Span (% of total)**
Fruman and Tulin (1976)	2.337	10.65	100 to 1000	11.2 to 27.3	Sampling Slits 38 mm x 0.25 mm	0 degree slot (0.5 x 300 mm)	~100%
Vdovin and Smol'yakov (1978)	0.557	2 to 12	560 to 5000	1.3 to 12.6	Sampling Ports 0.5 mm diameter and Traversed Sampling Tubes with 0.15 x 1.5 mm openings	7 degree slot (0.7 x 120)	80%
Vdovin and Smol'yakov (1981)	4.5	2.5 to 10	250 to 4000	1.1 to 23	Sampling Ports	20 degree slot (0.4 x 140 mm or 0.8 x 140 mm)	87%
Fontaine *et al.* (1992)	~0.3	4.5 to 18.3	500 and 1000	1.6 to 4	PLIF	25 degree slot (1 mm x 152 mm)	50%
Petrie *et al.* (2005)	~0.3	6 to 18	100 to 500	2 to 20	PLIF	Contoured Plenum Slot	81%
Present Results	9.36	6.6 to 20	1000 to 4000	2 to 10	PLIF	25 degree slot (1 mm exit cross section x 2650 mm)	88%

Table 5: Evolution of the Weissenberg Numbers with decreasing K-Factor at $U = 13.2\ ms^{-1}$. The intrinsic drag reduction and intrinsic concentration were derived from all the near-wall concentration measurements at all speeds for a given polymer.

WSR-N60K	K	c_M ($wppm$)	θ (s)	u_τ (ms^{-1})	We^+	We^*	We_D
Development Region	$> 2 \times 10^{-7}$	>200	>0.02	~0.3	>1800	~60	~4
Middle of the Transitional Region	$\sim 6 \times 10^{-8}$	~20	~0.01	~0.3	~720	~60	~4
End of the Transition Region	$\sim 2 \times 10^{-8}$	~5	~0.004	~0.4	~640	~107	~7
Final Region	$\sim 2 \times 10^{-9}$	< 1	~0.0005	~0.4	~160	~107	~7
WSR-301							
Development Region	$> 2 \times 10^{-7}$	>500	>0.05	~0.3	>4000	~107	~12
Middle of the Transitional Region	$\sim 6 \times 10^{-8}$	~20	~0.01	~0.3	~1000	~107	~12
End of the Transition Region	$\sim 2 \times 10^{-8}$	~2	~0.004	~0.4	~640	~190	~23
Final Region	$\sim 2 \times 10^{-9}$	< 1	~0.001	~0.4	~480	~190	~23
WSR-308							
Development Region	$> 2 \times 10^{-7}$	>500	>0.05	~0.3	>9900	~214	~59
Middle of the Transitional Region	$\sim 6 \times 10^{-8}$	~50	~0.035	~0.3	~3150	~214	~59
End of the Transition Region	$\sim 2 \times 10^{-8}$	~5	~0.011	~0.4	~1760	~381	~105
Final Region	$\sim 2 \times 10^{-9}$	< 1	~0.004	~0.4	~1600	~381	~105

Table 6: The intrinsic drag reduction, $[\%DR/c_M]$, and intrinsic concentration, $[C]$, for the near-wall polymer solutions. The values for each speed and for all speeds combined are presented. The fitted curves are shown in Figure 15.

	U (ms^{-1})	$[\%DR/c_M]$ ($wppm^{-1}$)	$[C]$ ($wppm$)
WSR-N60K	6.65	6	7
	13.2	6	8
	19.9	4	12
	All	**5**	**10**
WSR-301	6.65	32	2
	13.2	25	2
	19.9	17	3
	All	**26**	**2**
WSR-308	6.65	73	1
	13.2	27	3
	19.9	14	5
	All	**32**	**2**

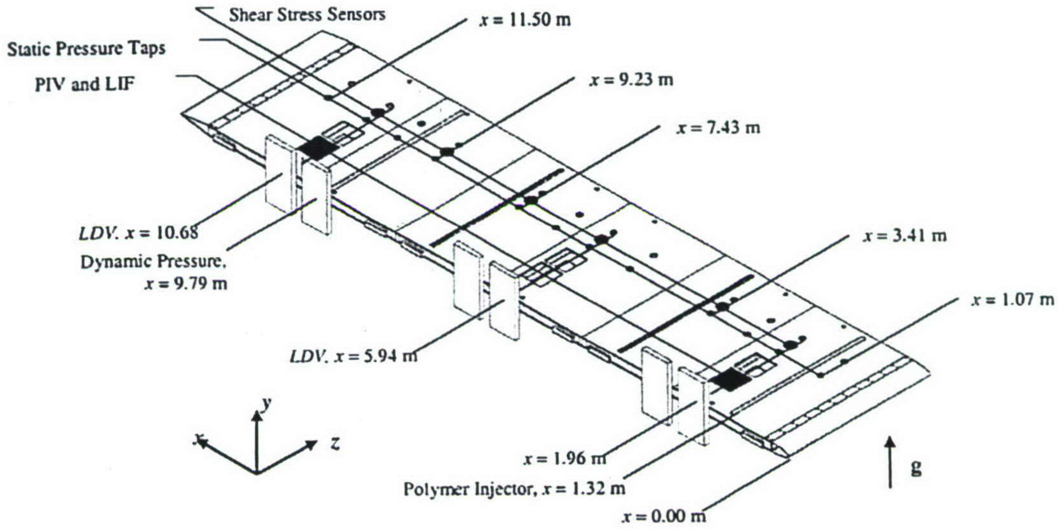

Figure 1: Schematic drawing of the large flat-plate test model with injection and measurement locations.

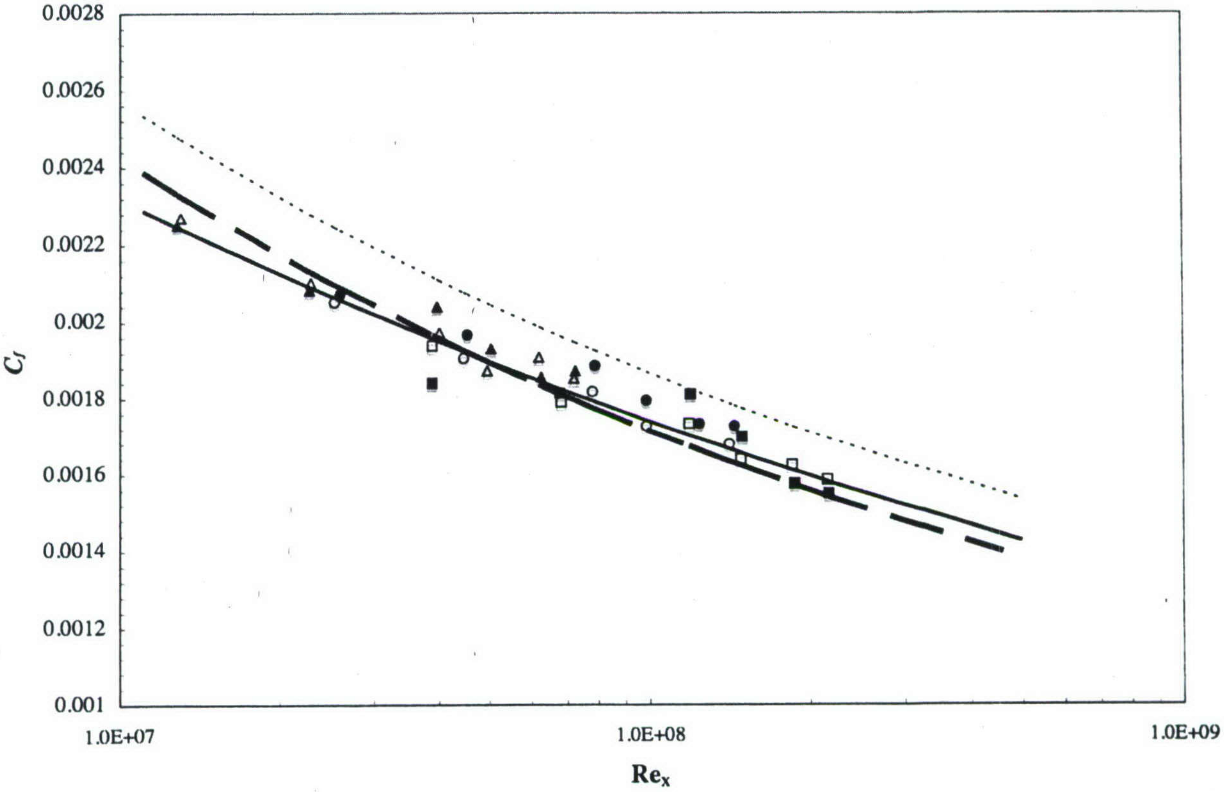

Figure 2: Baseline skin-friction coefficient, C_f, *vs*. Reynolds Number from two separate phases of the experiments (open symbols are from Phase III and closed symbols are from Phase IV) for $U = 6.65$ (Δ), 13.2 (○), and (□) 19.9 ms^{-1}. Also shown are the power-law fit to the experimental data (Equation 3.3, solid line) and two standard skin-friction correlations from White (1991) (Equation 3.1, light dashed line) and Schultz-Grunow (1941) (Equation 3.2, heavy dashed line).

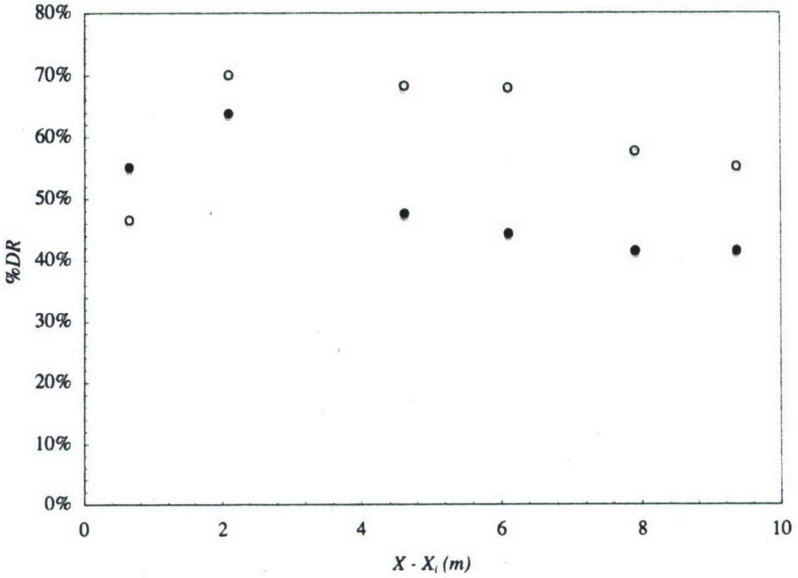

Figure 3: The *%DR vs.* downstream distance from the injector, $X\text{-}X_i$, illustrating the development region. The injected polymer is WSR-301 with $C_i = 4000$ *wppm*, and $Q_i/Q_s = 10$ for $U = 6.65$ (○) and 13.2 ms^{-1}(●).

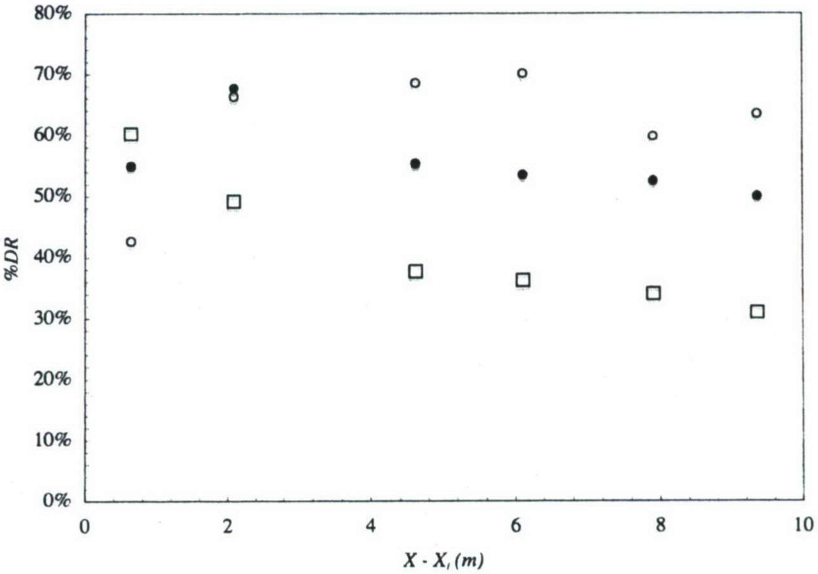

Figure 4: The *%DR vs.* downstream distance from the injector, $X\text{-}X_i$, for WSR-308 for $C_i = 4000$ *wppm* polymer injected at $Q_i/Q_S = 10$ for $U = 6.65$ (○), 13.2 (●), and 19.9 ms^{-1} (□).

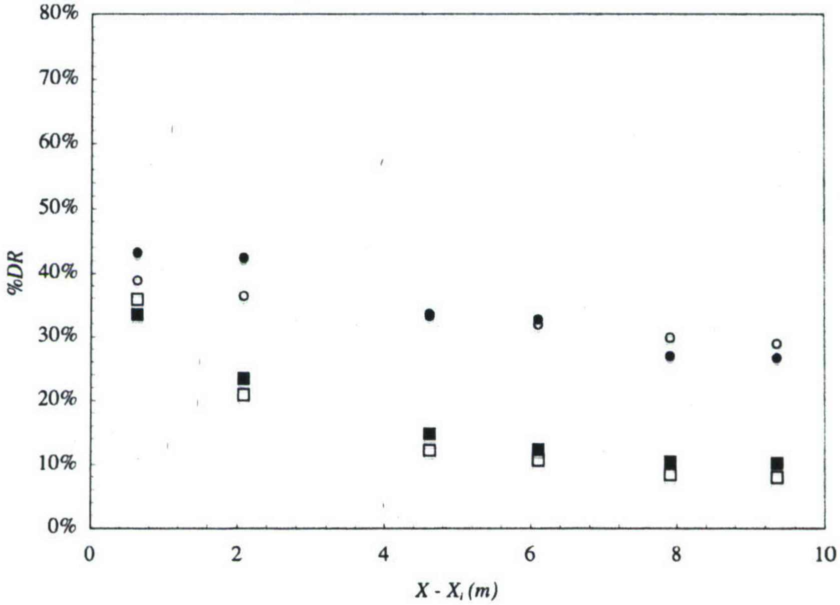

Figure 5: The *%DR vs.* downstream distance from the injector, $X\text{-}X_i$, for WSR-301. (○) $U = 6.65\ ms^{-1}$, $C_i = 1000$ *wppm* and $Q_i/Q_S = 4$; (●) $U = 6.65\ ms^{-1}$, $C_i = 2000$ *wppm* and $Q_i/Q_S = 2$; (□) $U = 13.2\ ms^{-1}$, $C_i = 1000$ *wppm* and $Q_i/Q_S = 4$; (■) $U = 13.2\ ms^{-1}$, $C_i = 2000$ *wppm* and $Q_i/Q_S = 2$.

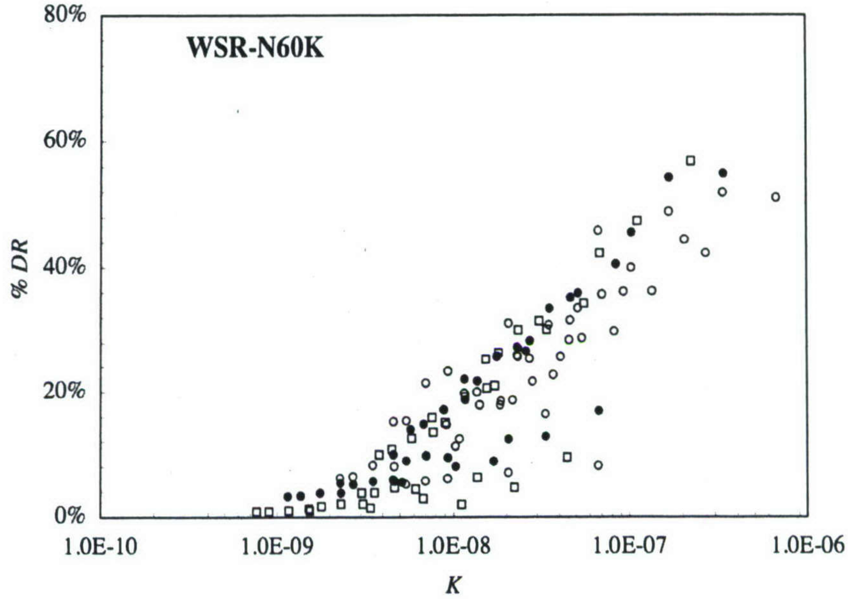
WSR-N60K
80%
60%
40%
20%
0%
% DR
1.0E-10
1.0E-09
1.0E-08
1.0E-07
1.0E-06
K

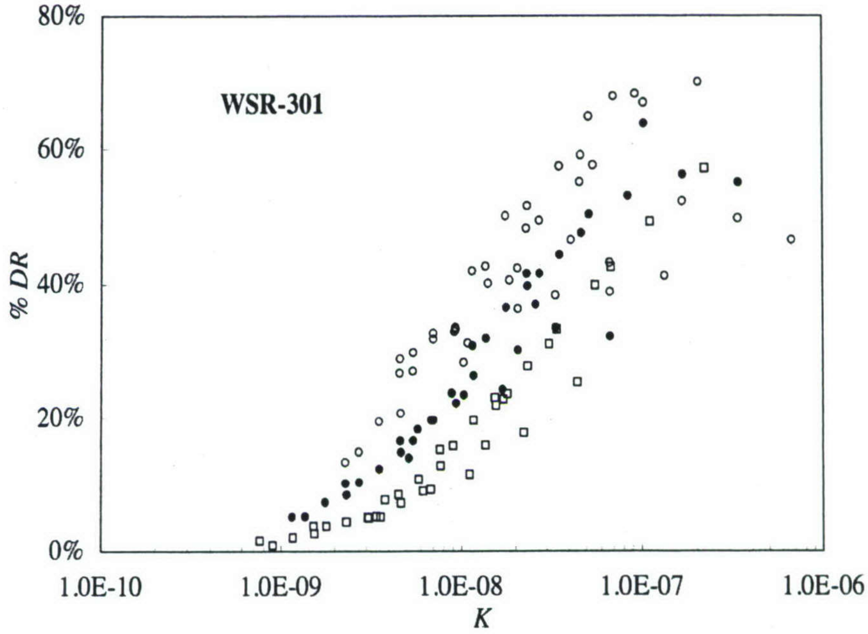
WSR-301
80%
60%
40%
20%
0%
% DR
1.0E-10
1.0E-09
1.0E-08
1.0E-07
1.0E-06
K

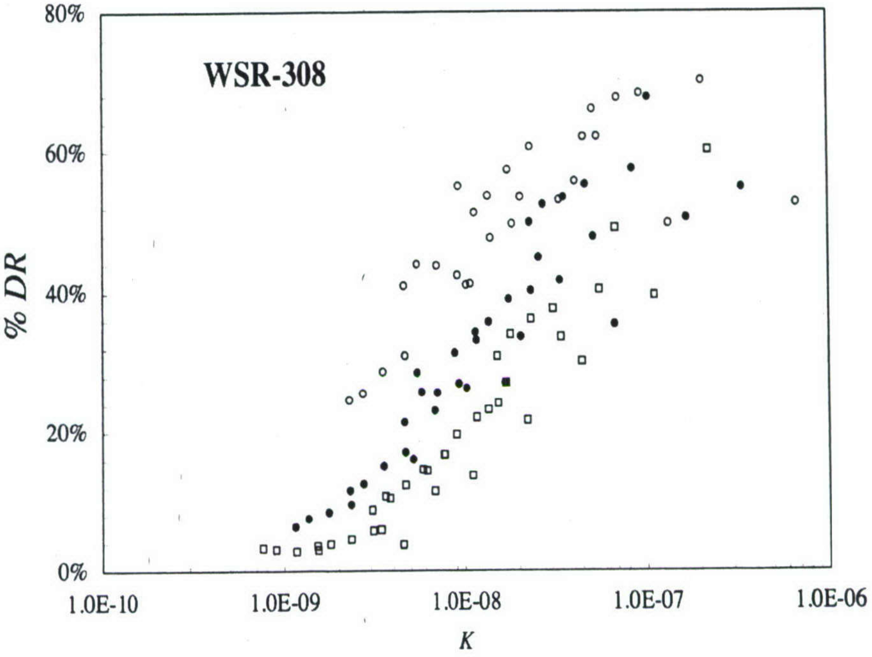

Figure 6: *%DR vs. K* for all three M_w polymers at $U = 6.65$ (○), 13.2 (●), and 19.9 (☐) ms^{-1}.

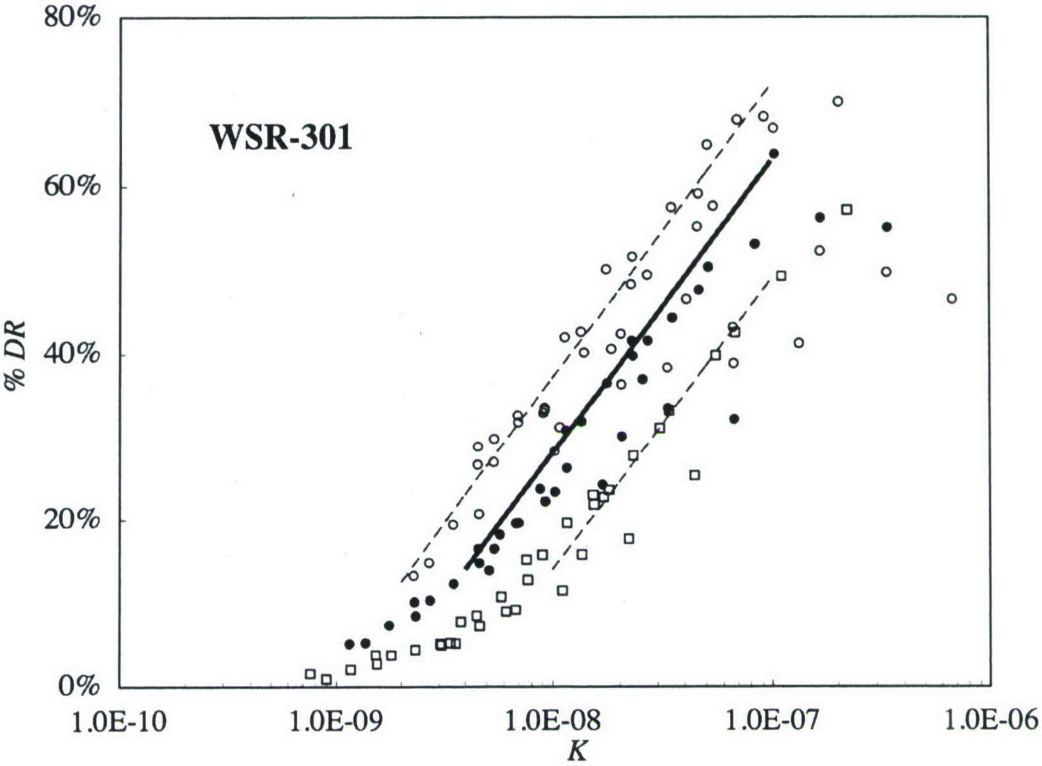

Figure 7: *%DR vs. K* for WSR-301 at *U* = 6.65 (○), 13.2 (●), and 19.9 (☐) *ms*$^{-1}$. Also shown is the trend line reported by Vdovin and Smol'yakov (1981) for flow in the transitional region (solid line). Similar slopes are found at all three speeds, although the *K* value at which the transition region starts changes with speed (dashed lines).

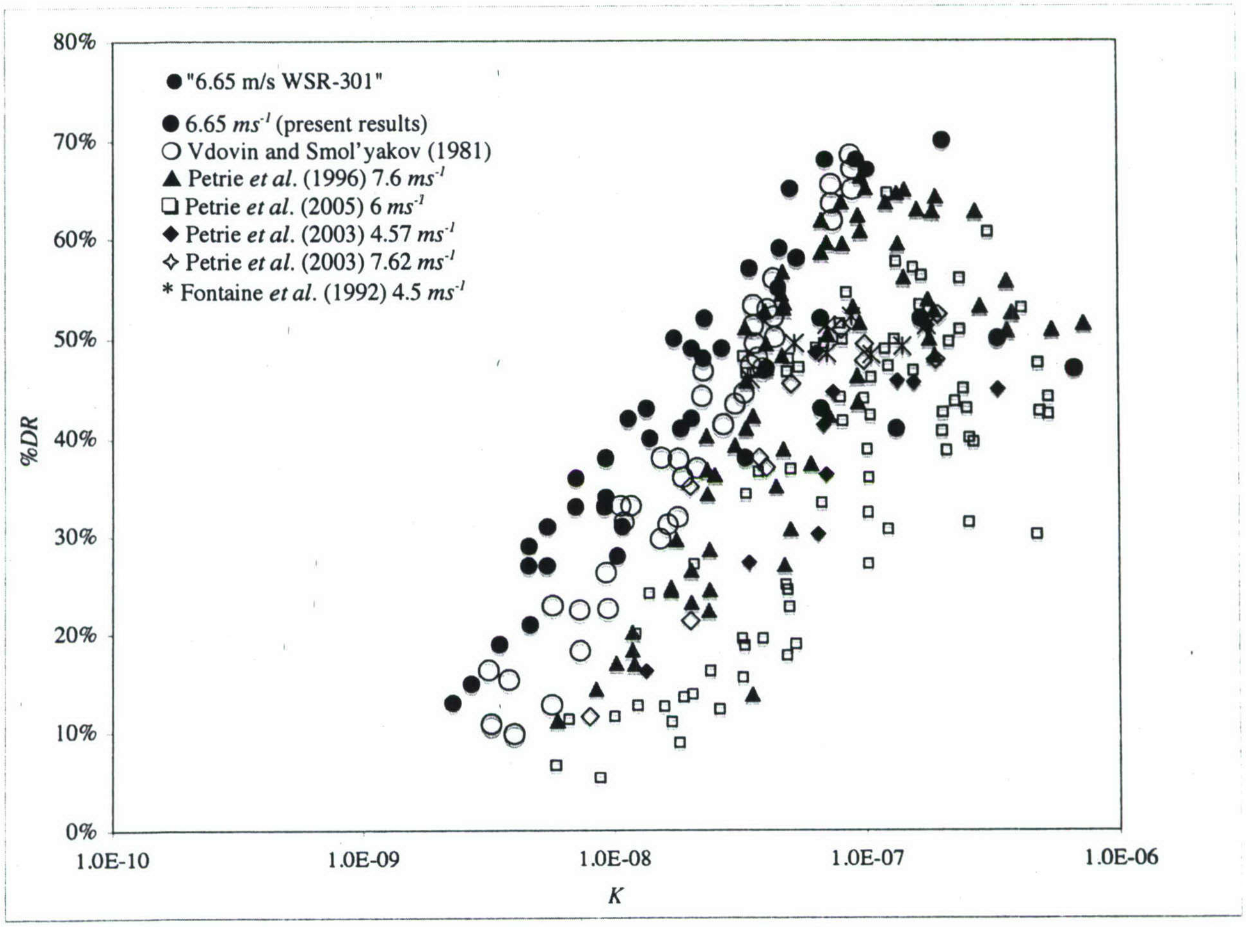

80%
70%
60%
50%
40%
30%
20%
10%
0%
%DR
1.0E-10
1.0E-09
1.0E-08
1.0E-07
1.0E-06
K
● "6.65 m/s WSR-301"
● 6.65 ms^{-1} (present results)
○ Vdovin and Smol'yakov (1981)
▲ Petrie *et al.* (1996) 7.6 ms^{-1}
☐ Petrie *et al.* (2005) 6 ms^{-1}
◆ Petrie *et al.* (2003) 4.57 ms^{-1}
◇ Petrie *et al.* (2003) 7.62 ms^{-1}
* Fontaine *et al.* (1992) 4.5 ms^{-1}

(a)

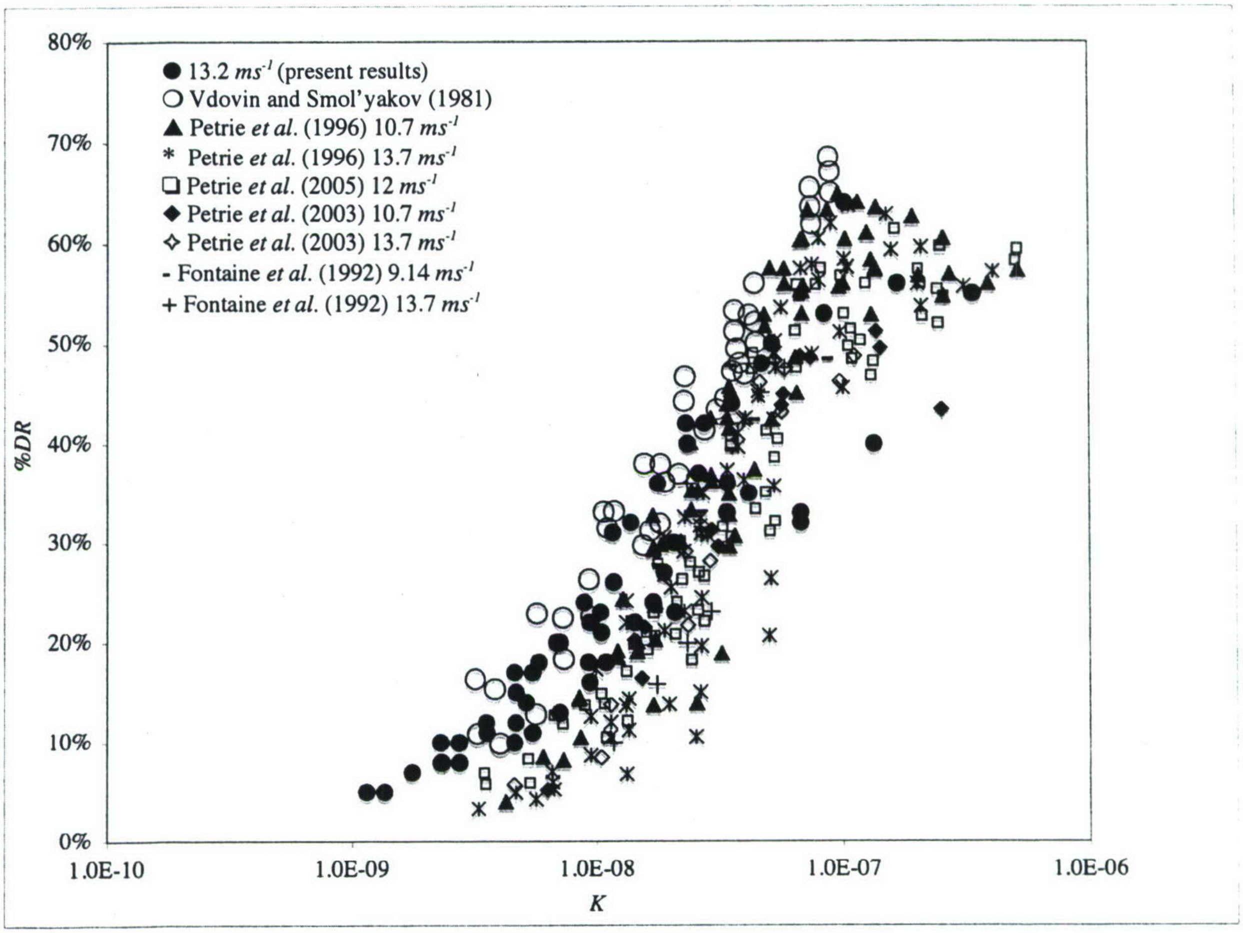
80%
70%
60%
50%
40%
30%
20%
10%
0%
%DR
● 13.2 ms-1 (present results)
○ Vdovin and Smol'yakov (1981)
▲ Petrie et al. (1996) 10.7 ms-1
* Petrie et al. (1996) 13.7 ms-1
□ Petrie et al. (2005) 12 ms-1
◆ Petrie et al. (2003) 10.7 ms-1
◇ Petrie et al. (2003) 13.7 ms-1
- Fontaine et al. (1992) 9.14 ms-1
+ Fontaine et al. (1992) 13.7 ms-1
1.0E-10
1.0E-09
1.0E-08
1.0E-07
1.0E-06
K

(b)

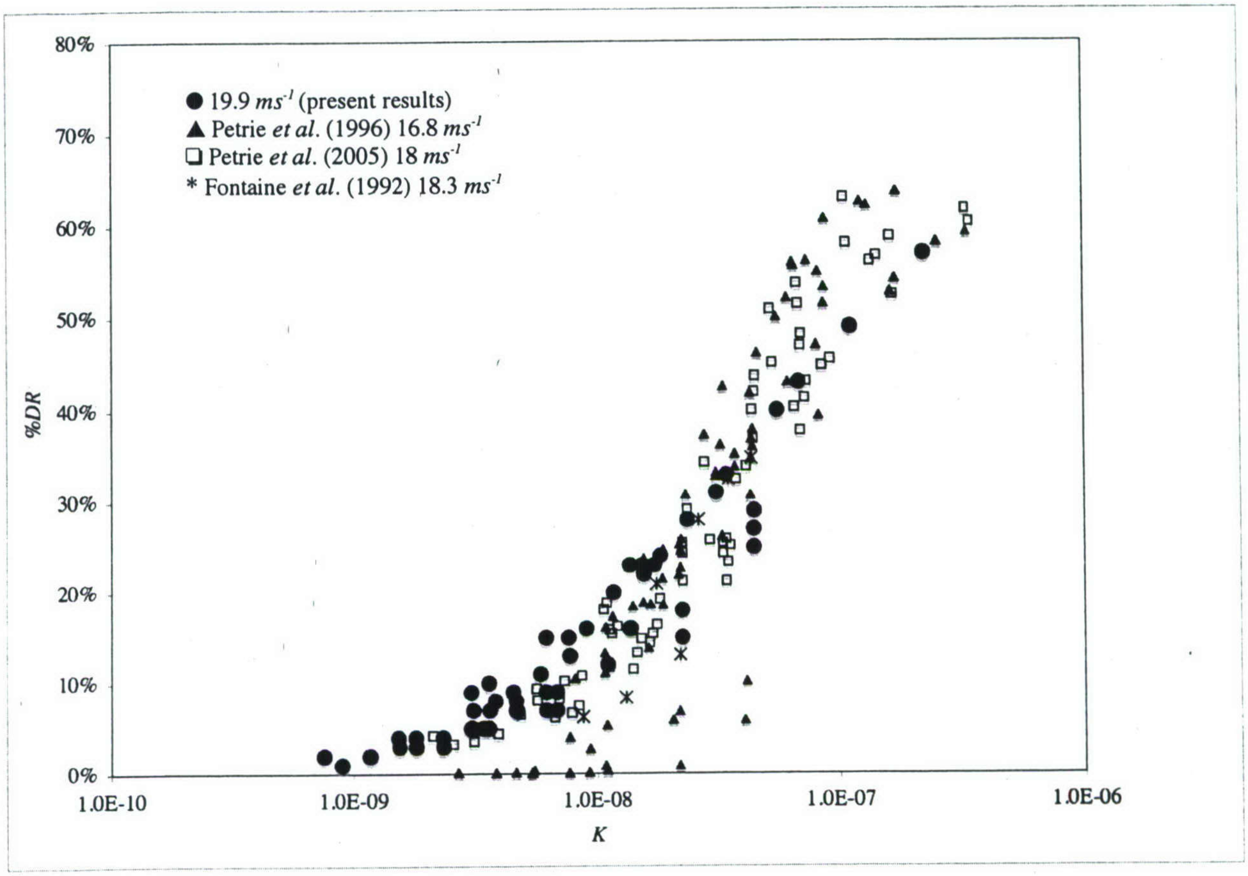

(c)

Figure 8: *K vs. %DR* from the present experiments and those reported previously for WSR-301. Data is segregated into (a) low, (b) medium, and (c) high free-stream speeds. The experimental descriptions and conditions are provided in Table 3.

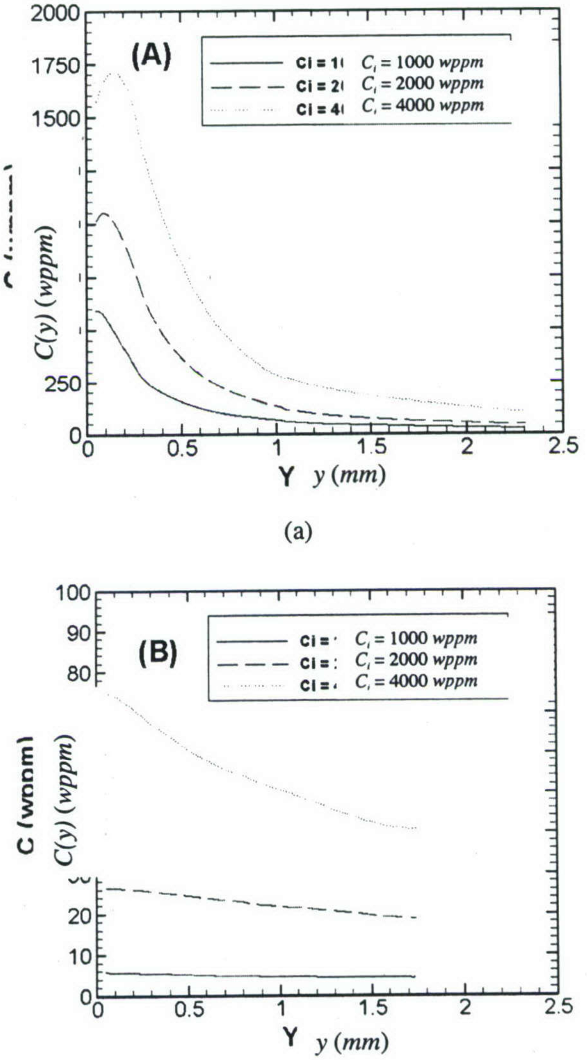

(a)

(b)

Figure 9: Near-wall concentration profiles of WSR-301 at $X\text{-}X_i = 0.64$ *m* (a) and 4.62 *m* (b) for $U = 6.65$ ms^{-1} and Q_i/Q_S=10.

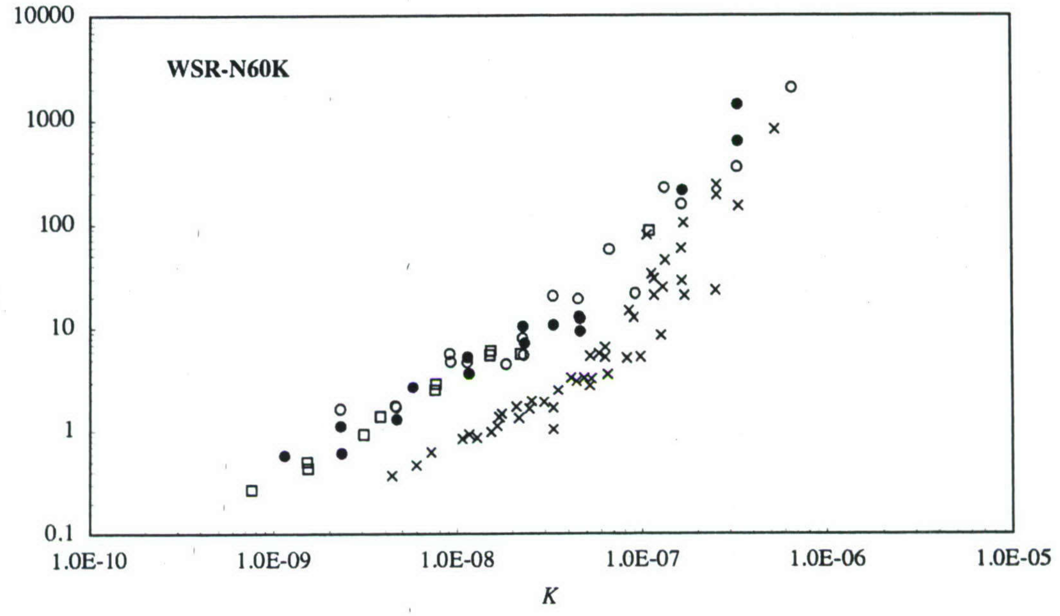
WSR-N60K
10000
1000
100
10
1
0.1
c_M (wppm)
1.0E-10
1.0E-09
1.0E-08
1.0E-07
1.0E-06
1.0E-05
K

(a)

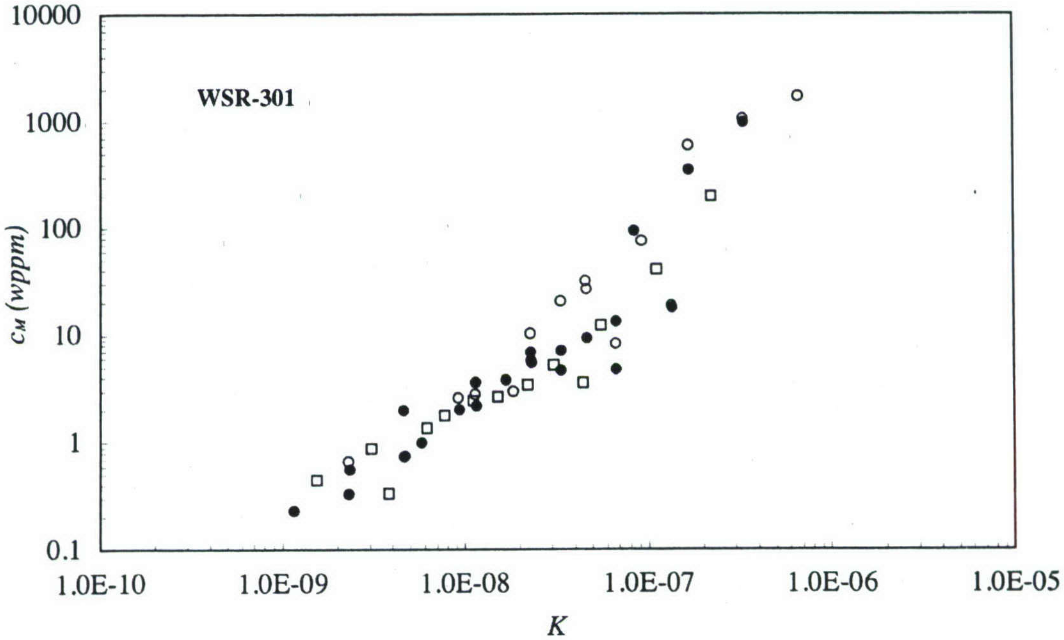
WSR-301
10000
1000
100
10
1
0.1
c_M (wppm)
1.0E-10
1.0E-09
1.0E-08
1.0E-07
1.0E-06
1.0E-05
K

(b)

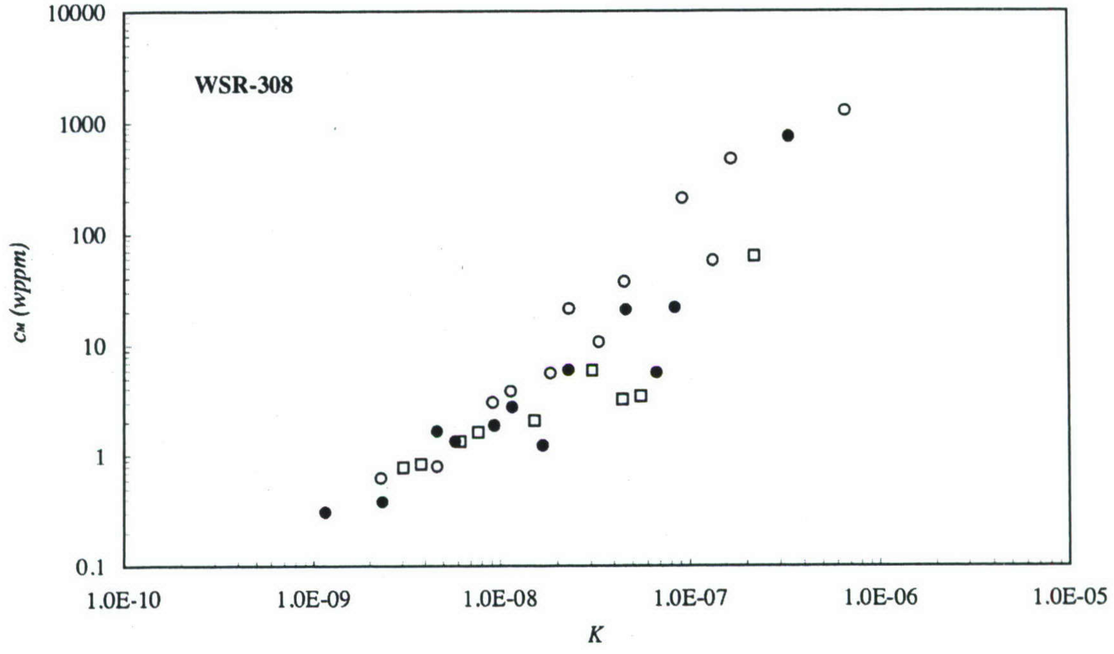

(c)

Figure 10: The maximum near wall concentration, c_M, *vs*. *K* for (a) WSR-N60K, (b) WSR-301, and (c) WSR-308 at *U* = 6.65 (○), 13.2 (●), and 19.9 (□) ms^{-1}. The data for WSR-N60K from Petrie *et al*. (2005) are also included (×).

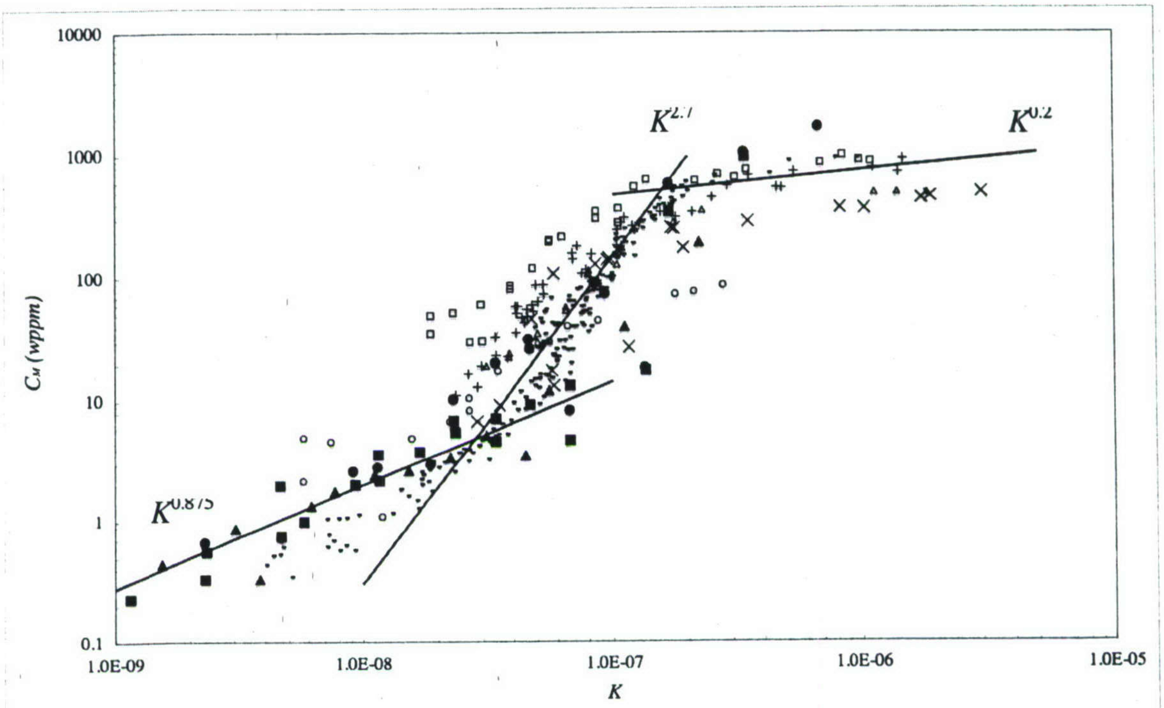

Figure 11: c_M *vs*. *K* for WSR-301 of the present experiment (U = 6.65 (●), 13.2 (■), and 19.9 (▲) ms^{-1} with previously reported results; Fruman and Tulin (1976) with C_i = 100 *wppm* (○), 500 *wppm* (Δ), and 1000 *wppm* (□); Vdovin and Smol'yakov (1978), assuming C_i = 1000 *wppm* (+); Vdovin and Smol'yakov (1981), assuming C_i = 1000 *wppm*; (-); Fontaine *et al*. (1992) (X). The three lines correspond to exponents of 0.2, 2.7, and 0.857. Details of the previous experiments are provided in Table 4.

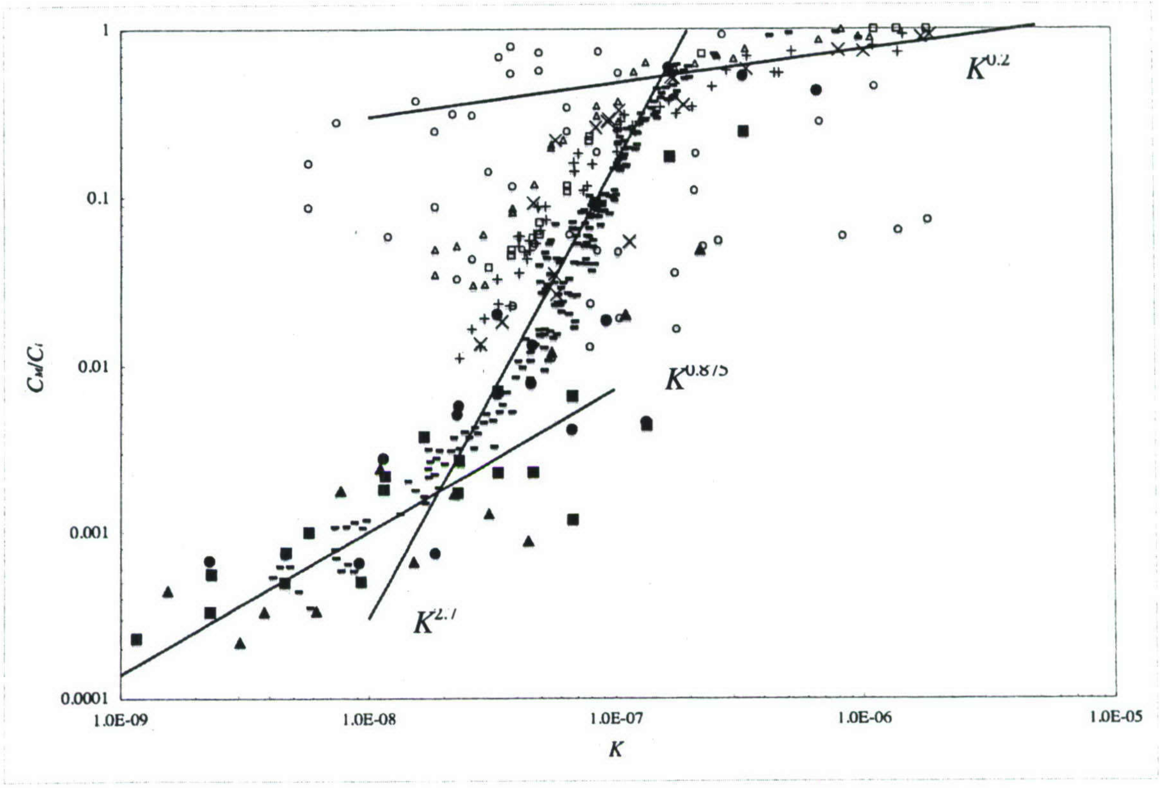

Figure 12: c_M/C_i *vs.* K for WSR-301 of the present experiment (U = 6.65 (●), 13.2 (■), and 19.9 (▲) ms^{-1} with previously reported results; Fruman and Tulin (1976) with C_i = 100 *wppm* (○), 500 *wppm* (Δ), and 1000 *wppm* (□); Vdovin and Smol'yakov (1978), assuming C_i = 1000 *wppm* (+); Vdovin and Smol'yakov (1981), assuming C_i = 1000 *wppm*; (-); Fontaine *et al.* (1992) (×). The three lines correspond to exponents of 0.2, 2.7, and 0.857. Details of the previous experiments are provided in Table 4.

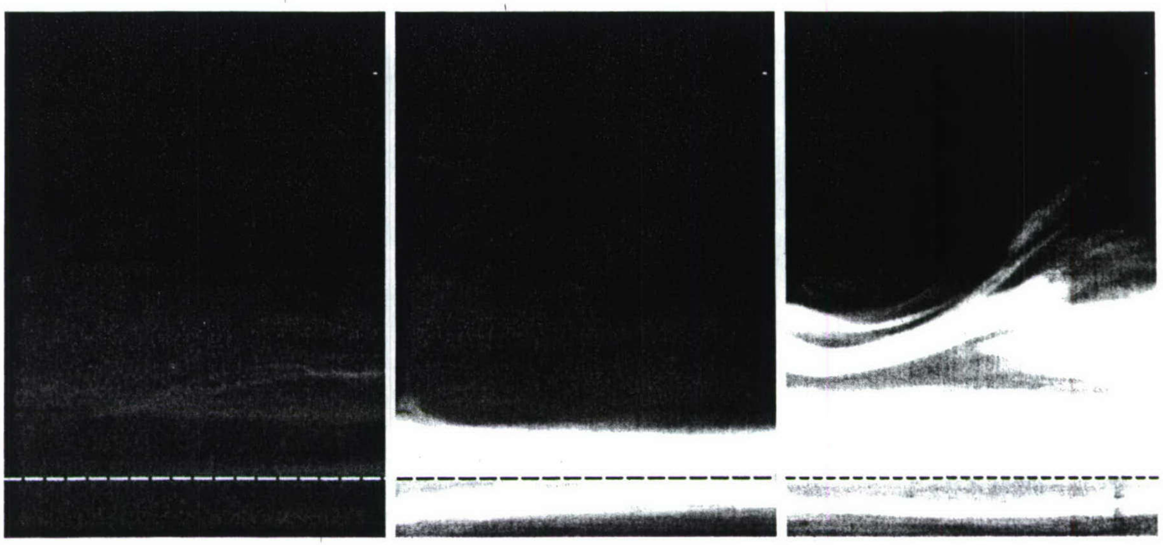

Figure 13: Three images of the near-wall polymer concentration fields taken in the filamented region where $K > 2.4 \times 10^{-7}$ (WSR-301, $Q_i/Q_s = 10$, $C_i = 4000$ *wppm*, $U = 6.65$ ms^{-1}). Three types of images are common: 1) Images with minimal polymer concentration (left image), 2) Images that appear to have a thin sheet of polymer flowing along the model surface (middle image), and 3) Images with large amounts of filaments both along the model surface and lofted away from the surface (right image). The flow is from left to right, and the dashed line denotes the location of the solid wall. The stretched field of view is 5 *mm* (stream-wise) by 2.25 *mm* (wall normal).

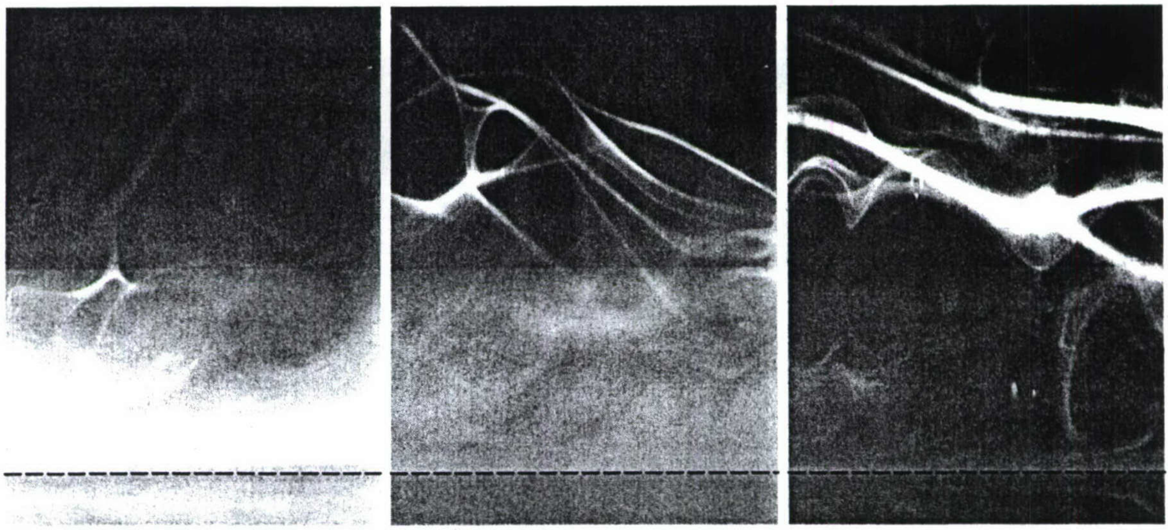

Figure 14: Three images of the near-wall polymer concentration fields taken in the transition region between highly filamented and uniform regions ($5.3 \times 10^{-8} < K < 2.4 \times 10^{-7}$) (WSR-301, $Q_i/Q_s = 2$, $C_i = 4000$ *wppm*, $U = 6.65$ ms^{-1}). This flow regime is characterized by periodic filaments in a somewhat uniform background polymer concentration. The images selected show various examples of background polymer concentration with lofted polymer filaments. The flow is from left to right, and the dashed line denotes the location of the solid wall. The stretched field of view is 5 *mm* (stream-wise) by 2.25 *mm* (wall normal).

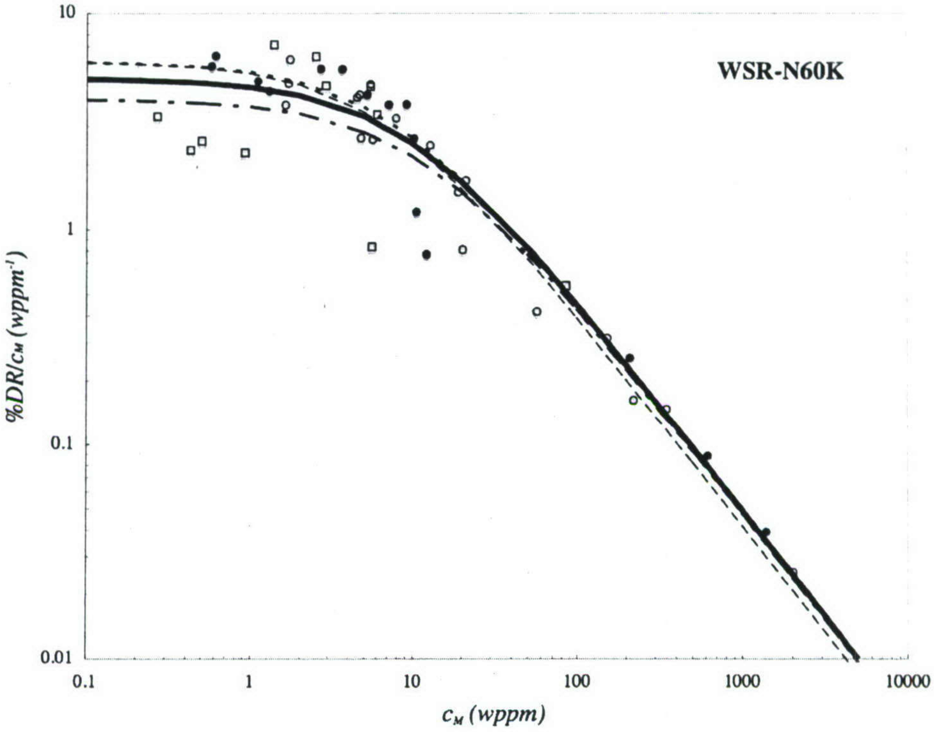
WSR-N60K
%DR/c_M ($wppm^{-1}$)
10
1
0.1
0.01
0.1
1
10
100
1000
10000
c_M (wppm)

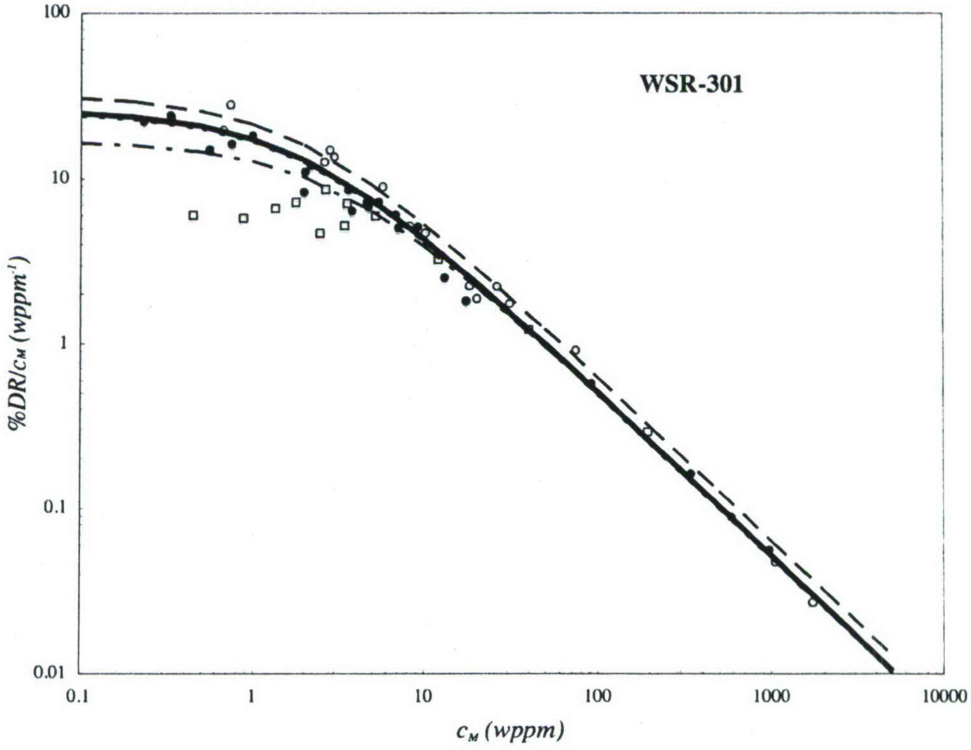
WSR-301
%DR/c_M ($wppm^{-1}$)
100
10
1
0.1
0.01
0.1
1
10
100
1000
10000
c_M (wppm)

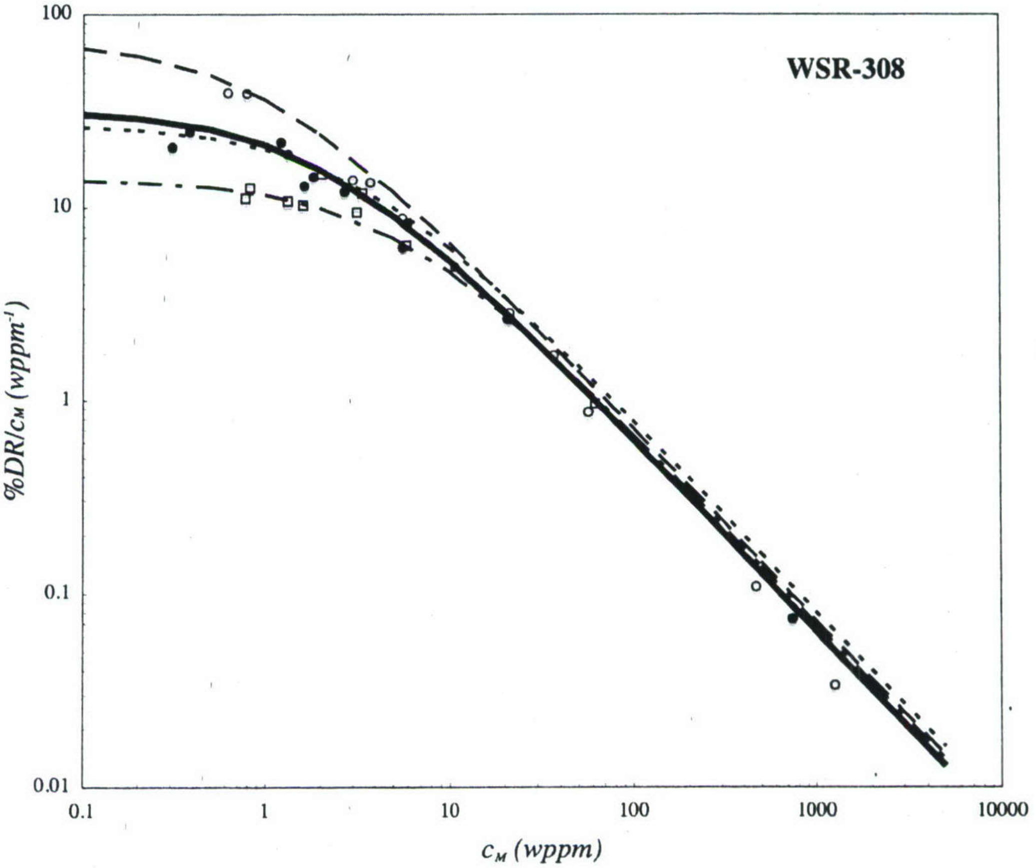

Figure 15: $\%DR/c_M$ *vs.* c_M for the three M_W examined: $U = 6.65$ (○), 13.2 (●), and 19.9 (☐) ms^{-1}. Curves fitted to Eq. 7.4 are plotted for each speed (dashed lines) and for all speeds together (solid line). Values of intrinsic drag reduction and intrinsic concentration derived from the fitted curves are provided in Table 6.

Appendix C:

BUBBLE-INDUCED SKIN-FRICTION DRAG REDUCTION AND THE ABRUPT TRANSITION TO AIR-LAYER DRAG REDUCTION

BRIAN R. ELBING, ERIC S. WINKEL, KEARY A. LAY, STEVEN L. CECCIO,
DAVID R. DOWLING, AND MARC PERLIN

Department of Mechanical Engineering University of Michigan, Ann Arbor, MI 48109, USA

(Submitted to the *Journal of Fluid Mechanics* –November 2007)

To investigate the phenomena of skin-friction drag reduction in a turbulent boundary layer (TBL) at large scales and high Reynolds numbers, a set of experiments has been conducted at the US Navy's William B. Morgan Large Cavitation Channel (LCC). Drag reduction was achieved by injecting gas (air) from a line source through the wall of a nearly zero-pressure-gradient TBL of a flat plate test model that was either hydraulically smooth or fully rough. Two distinct drag reduction phenomena were investigated; bubble drag reduction (BDR) and air layer drag reduction (ALDR).

The stream-wise distribution of skin-friction drag reduction was monitored with six skin-friction balances at downstream distance-based Reynolds numbers to 220 million and at test speeds to 20.0 ms^{-1}. Near-wall bulk void fraction was measured at twelve stream-wise locations with impedance probes, and near-wall ($0 < Y < 5$ mm) bubble populations were estimated with a bubble imaging system. The instrumental suite was used to investigate the scaling of BDR and the requirements to achieve ALDR.

Results from the BDR experiments indicate that: significant drag reduction (> 25%) is limited to the first couple *meters* downstream of injection; marginal improvement was possible with porous-plate versus slot injector design; BDR has negligible sensitivity to surface tension; bubble size is independent of surface tension downstream of injection; BDR is insensitive to boundary layer thickness at the injection location; and no synergetic effect is observed with compound injection. Using these data previous BDR scaling methods are investigated, but data collapse is observed only with the "initial zone" scaling, which provides little information on downstream persistence.

ALDR was investigated with a series of experiments that included a slow increase in the volumetric flux of air injected at free-stream speeds to 15.3 ms^{-1}. These results indicated that there are three distinct regions associated with drag reduction with air injection: Region I) BDR; Region II) transition between BDR and ALDR; and Region III) ALDR. In addition, once ALDR was established: friction drag reduction in excess of 80% was observed over the entire smooth model for speeds to 15.3 ms^{-1}; the critical volumetric flux of air required to achieve ALDR was observed to be approximately proportional to the square of the free-stream speed; slightly higher injection rates were required for ALDR if the surface tension was decreased; stable air layers were formed to free-stream speeds of 12.5 ms^{-1} with the surface fully roughened (though approximately 50% greater volumetric air flux was required); and ALDR was sensitive to the inflow conditions. The sensitivity to the inflow conditions can be mitigated by employing a small faired step (10 *mm* height in the experiment) that helps to create a clean separation line.

1. Introduction

As skin-friction drag is an important component of resistance in nearly all transportation systems moving in a fluid, skin-friction reduction techniques have been investigated for several decades. Prior investigations have shown that skin-friction drag reduction can be achieved by injecting gas (air) into the near-wall region of a liquid (water) turbulent boundary layer (TBL). Bubble drag reduction (BDR), has been shown to produce local drag reduction in excess of 80% in laboratory scale experiments, and has therefore attracted the interest of numerous investigators. Unfortunately, the majority of BDR experiments to date have been conducted at low Reynolds numbers (on the order of 10^7, based on downstream distance) and small scales (typically one meter or less), and the proper scaling laws remain unclear. For practical application of BDR to full-scale ships, experimental results at large scales and high-Reynolds numbers approaching those of full-scale craft are needed.

High Reynolds number experiments on BDR were reported by Sanders *et al.* (2006) for flows of a near-zero pressure gradient TBL. They showed that significant levels of BDR could be achieved near the injection location. However, they also reported that there was limited persistence of the BDR, which lasted only a meter or two from the location of injection. For BDR to be feasible, the propulsive power saved by drag reduction must exceed the power requirements for gas injection. And, the further downstream drag reduction persists, the less overall gas must be injected. However, with such low levels of persistence, BDR would require a large number of gas injection locations and a large volume of gas. Researchers have speculated that the gas injection process can be optimized to minimize pumping requirements and improve BDR persistence, as the geometry of injector will influence the size and speed distributions of the injected gas bubbles.

Sanders *et al.* (2006) also observed that, at lower flow speeds and higher gas injection rates, a layer of gas would form on the underside of the flat-plate and persist along its entire length. Such air layers would lead to skin friction reduction of greater than 80%. Air layers were observed for only a limited number of flow conditions, as examination of this phenomenon was not the principal goal of that study. However, the prospect that stable air layers can be formed, even at higher speeds, has led to increased interest in this phenomenon, which we term air layer drag reduction (ALDR) (see Winkel, 2006).

We present here a brief review of BDR and ALDR research. A seminal study of BDR was conducted 35 years ago when, using electrolysis to generate bubbles near the leading edge of an axisymmetric body, McCormick and Battacharyya (1973) showed promising results for skin-friction drag reduction. Net drag reduction approaching 40% was observed on a body 0.91 m in length at flow speeds to 2.6 ms^{-1}. In another early study, Bogdevich and Evseev (1976) observed that drag reduction peaks immediately downstream of the point of injection; however further downstream skin-friction returned to its usual level. Since, numerous BDR experiments have been conducted that investigated the parameters influencing drag reduction, some of which are described below. Gas is injected typically through a slot, porous-plate, or an array of holes at the wall of a TBL on an axisymmetric body or flat plate. Through this research a number of parameters have been identified which influence the level of drag reduction including: downstream distance from the injector, gas flow rates, free-stream velocity, plate orientation (buoyancy), injector geometry, and surface roughness. A review of skin-friction drag-reduction can be found in Merkle and Deutsch (1992).

Researchers at the Pennsylvania State University have conducted a number of BDR experiments. Here, we mention some highlights of their efforts, and subsequently we refer to their work as necessary. Madavan *et al.* (1984a, b) measured drag reduction in a laboratory scale flat-plate TBL. From these experiments they observed that: drag reduction was relatively independent of injector pore size (from 0.5 to 100 μm), bubble size distributions are determined primarily by the free-stream velocity and gas flow rate (increasing with increasing injection rate and decreasing free-stream speed), and drag reduction improves when the bubbly layer is beneath the solid surface of a plate rather than above it. Clark and Deutsch (1991) investigated drag reduction on an axisymmetric body with imposed pressure gradients. Their results showed that a mild favorable pressure gradient reduces the efficiency of BDR and that in adverse pressure gradients, gas injection leads to separation and high-levels of drag reduction. (Similar results were found more recently by Kawakita and Takano (2000) where pressure gradients were applied to a flat-plate TBL with gas injection. Skin-friction measurements showed improvements in drag reduction with the application of adverse pressure gradients near the point of injection.) Finally, Fontaine and Deutsch (1992) used five different gases with varying density and solubility and showed that the type of gas has little or no effect on the observed drag reduction.

The influence of bubble size on BDR processes has been examined by several researchers. McCormick and Battacharyya (1973) reported drag reduction of 10% to 30% with small bubbles generated by electrolysis, despite estimated mean void fractions in the boundary layer on the order of only 1%. Kawamura *et al.* (2003) produced bubbles with two different methods: the first involved injecting air through a slot, producing bubbles from 0.5 to 2 *mm* in diameter. The second enlisted bubble formation through out-gassing to produce bubbles 1/10th to 1/100th the size of the injected bubbles. (Here the "plate-on-bottom" configuration was employed and hence their finding may be a result of the increase in rise-velocity of the larger bubbles, causing them to migrate from the plate surface much more quickly.) They report that the smaller bubbles are nearly twice as effective at reducing skin-friction at equivalent void fractions. In contrast, Takahashi *et al.* (2001) examined BDR on a towed body and used surfactants to reduce the bubbles size. They reported no apparent difference in the resulting drag reduction. The majority of BDR experiments have been conducted in fresh water. If bubble size is an important factor in drag reduction, equivalent flows of salt water would be expected to have a significant influence on the bubble sizes produced and the resulting levels of drag reduction. Winkel *et al.* (2004) showed that bubble formation is modified and the resulting size distributions are reduced by approximately a factor of four (in diameter) in saltwater relative to freshwater. However, direct skin-friction measurements made by Shen *et al.* (2006) with gas injection into both fresh and saltwater produced no measurable difference in drag reduction. In most studies of BDR, the bubble sizes are much larger than the viscous length of the TBL, and it is possible that the injection of very small bubbles with dimensions on the order of the viscous length may lead to enhanced bubble turbulent interactions and drag reduction. However, Shen *et al.* (2006) injected very small (on the order of $10l_v$, *i.e.* 10 viscous wall units) lipid-stabilized bubbles into the boundary layer and saw no measurable improvement in drag reduction compared to BDR flows with larger bubbles and equivalent void fractions.

A group of Japanese researchers have performed experiments at large scales to directly address the issue of BDR scaling. Long, slender flat-bottom ship models, ranging from 12 to 50 *m* in length, have been towed at speeds to 7 ms^{-1} with gas injection (Watanabe *et al.*, 1998 and Kodama *et al.*, 1999). The test models were very slender, with a beam/width of 0.6 or 1.0 *m*. Gas was injected over the center 50% of the model span. Drag reduction was observed to decay with downstream distance, and by the end of the 50 *m* model only slight drag reduction existed, on the order of a few percent. Overall skin-friction reduction approaching 20% on the 50 *m* model was reported. However, it should be noted that there were no "skegs" or "strakes" to contain the gas underneath the models, thus gas may have escaped from the sides of the vessel. Kodama *et al.* (2002) reported that drag reduction measurements made in the span-wise direction showed poor uniformity, decreasing from a maximum at the model centerline to nearly zero at the outer edges. This observation agrees with the concept of gas escaping from underneath the test models.

The same Japanese research group has attempted at least two BDR experiments on full scale vessels exceeding 100 *m* in length. Gas was injected near the bow of a ship through horizontal arrays of holes at flow rates to 43 m^3s^{-1}. During the first at-sea demonstration (Kodama *et al.*, 2000) no net power savings was observed. The researchers reported that, although skin-friction reductions were thought to have been achieved, an offsetting reduction in propulsive efficiency occurred because of gas entrainment in the propeller. In more recent at-sea demonstrations (Nagamatsu *et al.*, 2002; and Kodama *et* *al.*, 2006), net friction reductions and power savings (after gas injection costs) of a few percent were demonstrated. Due to the scale and complexity (surface curvature, surface roughness, and sloped surfaces) of these at-sea demonstrations, almost no details of the distribution (stream-wise and span-wise) of the gas and corresponding drag reduction were measured.

The underlying physical mechanisms of BDR are not yet fully understood. It is generally agreed that for bubbles to reduce skin-friction they must in some way reduce the turbulent momentum exchange in the buffer region of the boundary layer. A number of different mechanisms have been proposed, and results suggest that multiple mechanisms work simultaneously. A reduction in the bulk density may play a role in the shear-stress reduction, by reducing the Reynolds stresses, $-\rho\langle u'v'\rangle$ in the near-wall region. Moreover, if the drag reduction effect is due to a simple density reduction, the observed level of drag reduction should scale with the near-wall void fraction. Lumley (1973, 1977) hypothesized that the presence of bubbles locally increased the viscosity in the buffer region. This increase in local viscosity would then reduce turbulent fluctuation levels and increases the thickness of the sub-layer and buffer region of the TBL. Similarly, Pal *et al.* (1989) observed that not only did mean skin-friction levels decrease during gas injection, but fluctuations in skin-friction were suppressed. In contrast to the proposed reduction in turbulence levels, using PIV Nagaya *et al.* (2001) observed an increase in turbulent fluctuations with gas injection. Although increases in both u' and v' fluctuation components were observed during drag reduction, they de-correlated, effectively reducing the Reynolds stresses. Finally, Meng and Uhlman (1998) propose "bubble-splitting" as a mechanism for BDR. Their argument is that energy is extracted as a larger bubble is split into two or more bubbles; the surface area, A_s, increases resulting in a higher surface energy, σA_s, where σ is the surface tension.

Numerical simulations of bubbly turbulent flows have been conducted that also yield insight to the mechanism(s) of BDR at relatively low Reynolds numbers. Using direct numerical simulation (DNS) of a bubbly shear-layer, Druzhinin and Elghobashi (1998) showed that bubbles migrate to the vortex cores in a turbulent shear flow and reduce turbulent fluctuations. Lu *et al.* (2005) examined bubbly channel flow and demonstrated the importance of bubble deformation whereby entrainment of bubbles into near-wall vortices suppressed the formation of stream-wise vorticity and drag; this effect was not observed for non-deforming bubbles. Similarly, van den Berg *et al.* (2005) examined friction drag reduction in a Taylor-Couette flow and also found a significant influence of bubble size and deformation on the bubble-vortex interactions and friction modification. These studies provide valuable insight into the scaling and mechanisms of BDR.

Though BDR has been studied extensively for more than 30 years, a universal scaling law that adequately collapses the experimental results has yet to be developed. The drag reduction is presented as a percentage drag-reduction, *%DR*, where τ_{wo} is the shear stress without gas injection and τ_w is the (reduced) skin friction with gas injection:

$$\%DR = 1 - \frac{\tau_w}{\tau_{wo}} \tag{1.1}$$

We would like to determine how *%DR* scales with the other independent parameters of the flow, such as the flow speed, U_∞, and the injected gas flux, Q_a, and other flow parameters. Madavan *et al.* (1985) report *%DR* as a function of the mean void fraction of air in the TBL, $\overline{\alpha}$, defined by (1.1)

$$\overline{\alpha} = \frac{Q_a}{Q_a + Q_W} \tag{1.2}$$

where Q_W is the volumetric flux of the liquid through the unmodified momentum boundary layer defined by (1.3) where δ_{99} is the boundary layer thickness, δ^* is the displacement thickness, and B is injector span,

$$Q_W' = U_\infty B\left(\delta_{99} - \delta^*\right). \tag{1.3}$$

While this scaling can collapse the data for a singe set of specific experiments, it does not adequately collapse experimental data across different flows, as it neglects several parameters which influence bubble drag reduction.

More recently, Deutsch *et al.* (2003) and Sanders *et al.* (2006) suggest other scaling relationships for BDR on rough and smooth plates, respectively. They developed the scaling parameter

$$\frac{Q_a}{Q_a + U_\infty B\theta_0}\frac{u_\tau}{u_\tau^*} \tag{1.4}$$

for both rough and smooth plates, where θ_0 is the unmodified local momentum thickness, and u_τ and u_τ^* are the friction velocities of smooth and rough surfaces, respectively. Sanders *et al.* (2006) proposed a similar scaling law for BDR on smooth surfaces,

$$\frac{Q_a}{Q_a + U_\infty B(\theta_{0,inj} - \theta_0)}, \tag{1.5}$$

that produces a better collapse of the data. However, it should be noted that the improvement in the collapse is due likely to the reduction in the length scale $[\theta_{0,\,inj} - \theta_0] < \theta_0$.

As opposed to BDR, ALDR occurs when a continuous or nearly-continuous layer of air is formed between a solid surface and the outer liquid flow, as observed for a limited number of conditions by Sanders *et al.* (2006). Although little or no experimental investigations have been conducted to investigate specifically the phenomenon of ALDR, BDR researchers have inadvertently created and reported some of the characteristics of ALDR. Madavan *et al.* (1985) reported a maximum level of drag reduction, typically in excess of 80-90%, where the increase of gas injection yielded little or no improvement in skin-friction reduction, likely associated with the formation of an air-layer. Kodama *et al.* (2002) described an attempt to establish an air-layer along a flat-plate test model at a free-stream speed of 10 ms^{-1}. Although the exact gas injection rates were not described, no stable persistent air-layer was established. They described an air-film that persisted 20 *cm* downstream of injection, and subsequently separated into slugs of air and eventually bubbles further downstream.

In the present work, we continue the study of BDR and ALDR using the test model employed by Sanders *et al.* (2006). We report on our continuing effort to understand the mechanisms underlying the limited persistence of BDR. Furthermore, we significantly extend our examination of ALDR. And, finally, we examine the influence of surfactants and surface roughness on the observed levels of drag reduction. The paper is organized in the following sections: we discuss the experimental methods used in the collection of the data in § 2 as well as the experimental program; the results of our experiments are presented in § 3 along with a discussion regarding the scaling of BDR and ALDR; and in § 4 the paper is summarized and conclusions are drawn.

2. *Experimental methods and the experimental program*

Three separate tests were conducted in the LCC on the same test model, and table 1 provides a summary of the experimental setups. (For a complete description of the LCC facility and its use, see Etter *et al.,* 2005.) The schematic of the test model working surface for the primary experiment, Test 1, is shown in figure 1. The two additional ALDR experiments investigated surface roughness (Test 2) and inlet condition sensitivity (Test 3). Test 2 used the same layout shown in figure 1 without the near-wall imagers and electrical impedance probes. Test 3 included a 1 *cm* step at the injector that was faired upstream to the model nose; the shear stress was integrated over sections of the body using six load sensors spanning nearly the entire model length. As in all the experiments, a coordinate system is used with the origin located in the plane of the plate's leading edge and X defined downstream, Y defined plate normal from the working surface of the model, and Z the span-wise coordinate. The suite of measurement devices included skin-friction force balances, *in situ* remote-controlled laser illumination for the onboard photographic imagers, electrical impedance probes, and flow metering. Bubble photographs and electrical impedance measurements were made in the near-wall region of the test model.

2.1. Instrumentation

2.1.1. Gas Injectors and Flow Metering

Gas was injected through the lower surface of the test model at two locations, $X = X_{inj} = 1.38$ and 3.73 *m* where X_{inj} is the injector downstream location. Two different types of injectors (slot and porous-plate), spanning the center 2.65 *m* of the test model (~ 87% of the model span) were tested; cross-sectional schematics of the porous-plate injector can be found in Sanders *et al.* (2006) while the slot injector used in Test 1, Slot A, is shown in figure 2. The porous-plate injector consisted of a slot inclined at a mean angle of 25° from the working surface of the test model and contracting at a full angle of 10°. The slot was capped by a layer of porous (40 *μm* mean pore diameter) sintered stainless steel (Mott Corporation), 2.0 *mm* thick extending 25 *mm* in the stream-wise direction. The layer of sintered metal was flush with the working surface of the model and fastened to the injector to ensure that all of the injected air passed through the porous material (Sanders *et al.*, 2006). Slot A was inclined 12° from the working surface with a constant throat gap of 5.75 *mm* that produced an opening in the stream-wise direction of 28 *mm*. Tests 2 and 3 used the Slot B design, also shown in figure 2, which had the slot inclined at a shallow 5.7° from the model surface and contracting at a full angle of 6.1°. The downstream edge was broken giving it a convex surface that produced a 1.5 *cm* opening on the test model surface. During Test 2, a porous material was used in the contracting slot to produce pressure drop close the surface opening (required for a separate experiment not discussed here). Test 3 used a modified injector from test 2 with a 1.3 *cm* step affixed to the upstream edge of the injector opening. The injector opening was 1.4 *m* downstream of the leading edge of the plate. The step was constructed of PVC and continued forward to the nose of the model where it was faired with fiberglass reinforced epoxy. The injector from Test 2 was modified slightly with the installation of nine equally spaced vanes in the injection slot to maintain its shape. Two of these vanes, along with the previously installed baffles and screens, divided the injector into three sections. Each of these sections had its own manifold as well as airflow regulation (as described below).

The gas injection rate was monitored using two insertion thermal mass-flow meters (640S Steel-Mass, Sierra Instruments) mounted at the center of a 6.3 *cm* inner diameter straight steel pipe. To ensure that the flow was fully developed at the monitoring locations, the flow meters were located 30 inner diameters (1.90 *m*) downstream and 10 inner diameters (0.63 *m*) upstream of any junctions in the line. The flow meters were factory calibrated for the range of 0 - 820 *SCFM* or equivalently 0 – 23.2 *SCMM* (Standard m^3 min^{-1}) over an operating range of 0-345 *kPa* and 10-54 °C. An analog voltage signal from each flow meter was recorded simultaneously with the skin-friction data. Gas was delivered to the injectors via 40 ports evenly spaced along a manifold that spanned the rear of each injector. Inside the manifold, three layers of screens and baffles were employed to generate a pressure drop to ensure the even distribution and uniformity of gas flux along the injector span.

2.1.2. Skin-friction Force Balances

Local skin-friction measurements were made at six stream-wise locations using floating-plate-type drag balances; their locations are shown in figure 1. The floating plate is 15.2 *cm* in diameter, 0.79 *cm* thick, and made of 17-4PH stainless-steel. The plate was fixed rigidly to a beryllium copper flexure that was instrumented with a full wheat-stone bridge of semiconductor strain gages. The drag balance and its housing were flush mounted using an eight point leveling system. The annular gap between the housing and the floating plate was 60 ± 20 *μm*. The semi-conductor strain gages were excited using a Vishay signal-conditioning amplifier (Model 2310, Vishay Measurement Group). The sensor outputs were amplified and low-pass filtered at 10 *Hz* with the same Vishay unit. The output signal was recorded at 50 *Hz* with a National Instruments NI-DAQ data acquisition board and a LabView virtual instrument.

The skin-friction balances were calibrated *in situ* with loads ranging from zero through 8.9 *N*. The loads were applied to the floating plate *via* a suction cup affixed to the plate and a tensioning cable attached to a precision load cell (Model LCEB-5, Omega Engineering). Tension was applied to the cable by moving the precision load cell with a linear traverse. Such a setup was necessary to eliminate biases that were found if the weights were simply suspended with cables and pulleys. The tensioning load cell was calibrated in the vertical position using precision weights prior to its use. Multiple calibrations were performed on the skin-friction sensors to confirm their repeatability and to assess the uncertainty of the measurement.

Test 3 used a different setup that measured the integrated skin-friction over six sections (approximately 1.6 m^2 each) spanning the entire model length. To accomplish this, precision rails and linear bearings were used to affix the model skin to the body of the model. Each of the six sections was instrumented with force transducers/load cells to measure the total frictional force on the respective section.

2.1.3. Bubble Imaging Systems

Images of the near-wall gas-laden boundary layer were acquired using three monochrome ½-*inch* format CCD cameras (Model CV-M10-SX, JAI, 659 x 494 pixel resolution) with 50 *mm* focal length lenses (HF-50HA-1B, Fujinon) and 40 *mm* extension tubes. To minimize blurring, the camera shutter speeds were set to 1.25 μs, creating a maximum image shift of less than two pixels (< 20 μm in the stream-wise direction) at the highest flow speeds. Images were acquired at 25 *Hz* with three analog frame grabbers (Model IMAQ-1409, National Instruments) through a LabView interface. As much as 4 *W* of blue-green light from three different argon-ion lasers (Model 5300, Lexel; Innova I-

90, Coherent; and Innova 70C, Coherent) were used to illuminate the bubble images. The laser light was delivered to the bubble images using multi-mode fiber optics at each of the three stream-wise locations.

A special technique was necessary to view the near-wall region. Using a periscope-like assembly, the image path utilized a "bump-out" prism protruding 5 *mm* from the surface of the test model. A cross-sectional schematic of the near-wall bubble imaging system is shown in figure 3. The image plane was normal to the lower model surface and aligned with the flow. The imaging regions and scales were slightly different for each of the three near-wall cameras, but all were approximately 8 *mm* (stream-wise) by 6 *mm* (vertical). The imagers were focused at the surface of the prism and the depth of field was measured to be 2 *mm* in air using a target inclined at 45° and noting where its image was in-focus. It should be noted that recorded bubble populations may be contaminated somewhat by the flow disturbance caused by the proximity to the protruding prism.

2.1.4. Electrical Impedance Probes

Electrical impedance probes were mounted on the model surface to measure the bulk void fraction in the near-wall region of the flow. (These measurements along with those from the near-wall cameras provided corroborative data regarding void fraction. Due to the difficulties involved with measurements of this type, redundant information was deemed necessary not just advantageous.) Each probe consisted of two brass electrodes soldered to signal conductors. The brass electrodes that were to be in contact with the flow were machined flush and mounted in an 11.4 *cm* diameter non-conducting, flat PVC disk. Each disk had a large (3.2 *mm* diameter electrodes with 6.4 *mm* cross-stream separation) and a small (1.6 *mm* diameter electrodes with 3.2 *mm* cross-stream separation) pair embedded. The purpose of the two sizes was to detect qualitatively void fraction gradients normal to the surface as illustrated in Cho *et al.* (2005). The probes were positioned 1.91 *cm* upstream and 1.91 *cm* downstream of the disk center for the small and large probes, respectively. The disks were positioned slightly off the cross-stream centerline and centered at 12 stream-wise locations (X = 1.07, 1.96, 2.59, 3.41, 5.09, 5.94, 6.61, 7.43, 9.23, 10.05, 10.68, 11.50 *m*). Each probe's interior surface was encased in an epoxy, which electrically isolated each electrode prior to contact with the flow.

The basic circuit for the electrical impedance probes is shown in figure 4 and consists of an AC excitation voltage (V_s), reference resistor (R_{ref}), probe electrical impedance associated with the flow (Z_{el}), stray capacitance from the input and output wires (Z_{c1} and Z_{c2}, respectively), and stray capacitance between the input and output wires (Z_{c3}). The stray capacitance between the input and output leads was minimized by shielding each separately, but is included due to its significant influence during measurement of higher void fractions. The input and output stray capacitance could not be neglected due to the length of the wires required for the experimental setup. This stray capacitance was measured *in situ* by short circuiting the probe with a known resistor and measuring the voltage across R_{ref}, V_{ref}. The stray capacitance was measured repeatedly throughout testing and showed negligible variation. The circuit AC excitation voltage was produced with a signal generator (8904A multifunction synthesizer, HP), and the reference resistor had a nominal resistance of 75 $k\Omega$, which maximized the output signal and sensitivity. Applying Kirchhoff's current law to the circuit provides the relationship between the electrode impedance and the known parameters:

$$Z_{el} = \frac{\left(V_s - V_{ref}\right) R_{ref} Z_{c2} Z_{c3}}{V_{ref}\left[Z_{c2}\left(R_{ref} + Z_{c3}\right) + R_{ref} Z_{c3}\right] - R_{ref} Z_{c2} V_s} \tag{2.1}$$

Four impedance measurement systems were fabricated to facilitate simultaneous measurements. During each experiment, measurements were acquired from each pair, necessitating a system for rapid probe multiplexing, performed using a 128-channel multiplexer (PXI-2530, National Instrument) that was capable of switching between each set of four probes at more than 200 *Hz*. The sampling time for each probe was approximately three seconds, the data were acquired at 1000 *Hz*. Data acquisition was initiated once the skin-friction sensors had achieved steady state.

Increased probe sensitivity was accomplished by recording the deviation of the measured impedance from the baseline impedance at zero void fraction. A lock-in amplifier (LIA) (SR830 DSP LIA, Stanford Research Systems) and a signal generator (8904A multifunction synthesizer, HP) were used to excite and balance the bridge as well as to demodulate the resulting signal. The typical output from the LIA was the amplitude and phase of V_{ref} - V_w with a gain of 20, averaged over 3 *ms*, and band-pass filtered (0.01 *Hz* about the center frequency). Each circuit had a separate excitation frequency (5, 7, 9, and 11 *kHz*). A single computer controlled all the probe multiplexing, V_w amplitude and phase variation, and data acquisition *via* a LabView virtual instrument and data acquisition card (PCI-6040E, National Instruments).

2.2. Data Analysis Techniques

2.2.1. Analysis of Skin-friction Drag Reduction

The drag reduction is presented as a percentage drag-reduction, *%DR*, defined by (1.1), where τ_{wo} is the shear stress without gas injection and τ_w is the (reduced) skin friction with gas injection. As gas was injected into the confined volume of the LCC, even with improved pressure control, the static pressure in the test section increased. And, these pressure excursions led to baseline drift in the measured shear stress as well as changes in the injected volume flux of gas. To account for this bias, a time-record of the static pressure on the upper wall of the test-section was recorded simultaneously with the skin-friction and gas injection rate data. As BDR scales with the volume of gas injected into the boundary layer (Shen *et al.*, 2006), the mass-flow rate recorded by the flow meters (as standard volumetric flow-rate) was converted to a true volumetric flow-rate at the test model surface using the ideal gas law. In addition, the increase in test-section pressure resulted in a decrease in the mass flow-rate. Thus, over the course of a gas injection test (typically 30-60 *s*) the volumetric injection rates decreased by as much as 30% (dependent on the free-stream velocity and gas injection rate), which can have a significant effect on the level of drag reduction achieved. To account for this, the time traces of shear stress and volumetric gas injection rate were segmented into 0.5 *s* intervals. The drag reduction observed during each interval was distributed among ten bins based on the volumetric injection rate.

2.2.2. Near-wall Void Fraction Analysis

The region of influence of the electrode pair can be defined as the radial distance, *R*, from the model surface through which a nominal percentage of the current passes (Cho *et al.*, 2005). Here the "influence volume" is bounded by two arbitrary values of *R*/*L* (with *L* the electrode spacing), through which 50% (*R*/*L* = 0.85) and 75% (*R*/*L* = 1.93) of the electrical current flows. A value for *R*/*L* of 1.4 was selected, the average of the 50% and 75% values, which yield influence radii of 4.4 and 8.8 *mm* for the 3.2 and 6.4 *mm* electrode pair spacing, respectively.

The measured impedance of (2.1) can be related to the volume averaged void fraction, α, using Maxwell's mixture model, (2.2) (Ceccio and George, 1996). This model provides an estimate only since the analysis of Hewitt (1978) following Maxwell (1881) assumed a uniformly disperse bubbly mixture, which is not expected in the present experiments.

$$\alpha = \frac{(Z_m - Z_w)(2 + \varepsilon_g/\varepsilon_w)}{(2Z_m + Z_w)(1 - \varepsilon_g/\varepsilon_w)} \tag{2.2}$$

Z_m and Z_w are the impedance of the mixture and water, respectively. σ_g (~ 0) and σ_w are the conductivity of the gas and water, respectively. For the current study the complex part of the mixture impedance is assumed to be negligible since $\sigma_w >> 2\pi f \tilde{\varepsilon}_L \varepsilon_o$, where σ_w is the conductivity of water (~3.5 $\mu S\ cm^{-1}$), f is the input frequency (~10 *kHz*), $\tilde{\varepsilon}_L$ is the non-dimensionalized permittivity of the water (~80), and ε_o is the permittivity of a vacuum ($8.85 \times 10^{-12}\ F\ m^{-1}$) (George *et al.*, 2000). The real part of the mixture impedance (*i.e.* the conductivity) dominates when σ_w is greater than 0.44 $\mu S\ cm^{-1}$.

2.2.3. Bubble Population Measurements

The resolution in the near-wall video images (Y ~ 0 to 5 *mm*) was determined from images of a scale recorded periodically throughout the test. The image resolutions from the three near-wall cameras ($X\text{-}X_{inj}$ = 0.58, 4.56, and 9.30 *m*) were determined to be 10.9 ± 0.2, 12.0 ± 0.2, and 12.5 ± 0.2 $\mu m\ pixel^{-1}$, respectively. The stated uncertainty in the resolutions is the 95% confidence interval determined from four different image calibrations and the Student's *t*-distribution

The images used for the bubble populations were selected at random and analyzed using National Instruments Vision Assistant program. The "measurement tool" of this data analysis software was used to draw line segments across the (approximate) diameter of the near spherical bubbles, in the stream-wise direction. Only in-focus bubbles were tabulated in a method described in Sander *et al.* (2006).

Approximately 1000 bubbles were counted from as many as 10 images for each flow condition. This is a sufficient number of bubbles to provide an accurate representation of the test data as the histograms are consistent on an image-to-image basis. An effort was made to count all the in-focus bubbles in each image to eliminate any random error; the worst possible bias error is estimated at two pixels (~25 μm) for the detection of each edge of the bubbles. This provides a bound on the smallest detectable bubbles in the images, about 25 μm, and while bubbles smaller than one pixel might appear as specks in the images, this was not observed.

The physical size of the bubbles observed in the image analysis ranged from approximately 25 to 1,000 μm. The resultant bubble diameters were placed in 25 μm bins.

The bubble size distributions, *N(d)*, were normalized such that $\sum_{i=1}^{L_d} N(d_i) = 1$, where L_d is the number of bins and *i* is the bin index.

2.3. Experimental Program

2.3.1. Experimental Test Matrix

In Test 1 the free-stream liquid velocity, gas injection rate, injection location, background surface tension and injector type were varied. Free-stream speeds ranging from 6.7 to 20.0 ms^{-1} and gas mass flow-rates of 100 to 800 *SCFM* (2.83 to 22.7 *SCMM*) with a maximum volumetric flux of 0.14 $m^2\ s^{-1}$ per unit injector span were tested. These experiments investigated BDR and ALDR from a single injection location, possible synergistic effects produced from compound injection from two slot injectors 2.35 *m* apart in the stream-wise direction, and the influence of background surface tension on BDR and ALDR. To test this latter effect, the LCC background water surface tension was reduced from about 70 to 50 $dyne\ cm^{-1}$ by adding 15 *wppm* of a common soluble surfactant, Triton-X-100. Research conducted by Winkel *et al.* (2004) showed that the addition of surfactant to the tunnel volume can reduce mean bubble diameters by more than a factor of two immediately downstream of injection. However, this phenomenon was not observed in the current results, which indicates that it is limited to near the injector.

Test 2 investigated ALDR on a roughened surface in two parts: Test 2a repeated a subset of conditions from Test 1b to determine sensitivity to injector design. Then, in Test 2b the entire model surface was roughened using epoxy paint (High Build Semi-Gloss 97-130, Aquapon) with glass bead grit. The particles were tightly packed producing a sand grain type roughness. Based on the skin-friction measurements and assuming a fully roughened surface the first 75% of the model was very uniform yielding an average roughness height, *k*, between 400 and 600 μm. The remaining 25% of the model was rougher with *k* ranging from 800 to 1100 μm. Free-stream speeds ranging from 6.7 to 15.8 ms^{-1} and volumetric fluxes from 0.03 to 0.14 m^3s^{-1} per unit injector span were tested.

Test 3 investigated ALDR via an alternate drag measurement method, and the effect of injecting air behind a small step to mitigate the effect of large turbulent structures at the injection point. Six large (1.6 m^2) floating plates were used to measure integral drag on the plate, as opposed to the six small floating balances used previously. Free-stream speeds ranged 5.9 to 11.8 ms^{-1} and gas injection rate per unit injector span varied from 0.049 to 0.16 m^2s^{-1}.

For all drag reduction experiments, prior to each injection a baseline (non-injection) skin-friction measurement was made for a period of about 15 seconds. For an injection run, shear stress data acquisition was started five seconds prior to gas injection and stopped five seconds post injection. In addition to the shear stress measurements, the gas mass flow-rate to one or both injectors and the static pressure of the LCC test section was recorded simultaneously. A control valve was preset to provide a desired gas injection rate according to the pre-determined test matrix. Two manual 10.2 *cm* diameter vents were added to the top of the LCC test section to help regulate pressure rise in the test section during a gas injection run. While the vents improved the pressure control there were still variations and some pressure rise did occur during gas injection.

2.3.2. Comparison with the Setup and Methods of Sanders et al. (2006)

The results presented aim to extend and improve the data set collected from a first phase of BDR tests, see Sanders (2004) and Sanders *et al.* (2006). All phases of the present experiment are meant to extend the current BDR research to larger scales, higher Reynolds numbers, and higher speeds in a well-controlled test environment. The previous phase of experimentation investigated drag reduction using injection from a single porous-plate injector located either 1.3 or 9.8 *m* downstream of the leading edge. The primary experiment investigated: *i)* the influence of injector geometry; *ii)* the influence of compound injection *via* simultaneous injection from two slot injectors (X = 1.38 and 3.73 *m*) for a variety of injection conditions; and *iii)* the influence on BDR due to a reduction in surface tension from the addition of surfactant. Both experiments investigated similar ranges of flow speeds, from 6.7 to 20.0 ms^{-1}, and gas injection rates to 22.7 *SCMM*.

In addition to the different set of test parameters, the present experiment provided higher fidelity measurements than those of Sanders *et al.* (2006). The main improvements are in the control of tunnel pressure through the addition of test section vents and simultaneous measurement of that pressure and the gas injection rate. As gas was injected from the test model, the vents were controlled manually to allow air and water to be purged from the tunnel to accommodate the injected volume of air. Secondly, the accuracy of air injection rate and tunnel pressure were improved by recording the time traces with the skin-friction balances, whereas for Sanders *et al.* (2006), static pressure and air flow-rate were monitored visually from a digital display. The improved measurements of the present experiments allow for real time comparison of drag reduction with volumetric gas injection rate.

3. Results

The presentation of results is divided into three subsections: Non-injection (baseline) results, BDR results, and ALDR results. The BDR and ALDR are separated as they are fundamentally differing flows, though air layers can arise as a consequence of bubble injection. These subsections are further divided according to our principal findings, including the effects of various parameters and the examination of potential scaling methods.

3.1 Baseline Results

3.1.1. Smooth Model Baseline Flow

Figure 5 shows the non-injection skin-friction coefficients obtained from Tests 1 and 2a on the smooth model, where $C_{fo} = \tau_{wo} / \frac{1}{2}\rho U_\infty{}^2$. Also plotted with the current baseline results is the best-fit curve from Sanders *et al.* (2006), and the Schultz-Grunow (1941) curve:

$$C_{fo} = 0.370 \log^{-2.584}\left(\mathrm{Re}_X\right) \tag{3.1}$$

where $\mathrm{Re}_X = U_\infty X/\nu$, X is the distance measured form the leading edge of the test model, and ν is the kinematic viscosity. It should be noted that Sanders *et al.* (2006) suspected their absolute skin-friction measurements were biased low due to both calibration bias from pulley friction and possible flow through the sensor housing. The current data were acquired after measures were taken to eliminate these effects, as described above. The current results indicate that Sanders *et al.* results were indeed biased low and that the present results from the same model are in good agreement with the Schultz-Grunow (1941) friction line.

3.1.2. Rough Model Baseline Results

Figure 6 shows the non-injection results obtained from Test 2b on the roughened model surface. The particles embedded in the epoxy coating were tightly packed giving an average roughness height, $k \sim 460 \pm 120\ \mu m$. This k value was uniform across the first nine meters of the plate, however along the last four meters, the coating was not applied as uniformly resulting in approximately double the k value. These skin-friction coefficient curves were used also to estimate the average roughness height by assuming the surface is fully rough, which is supported by the Reynolds number independence of the skin friction coefficient. The surface roughness was inferred from the measured drag after examining White's and Schlichting's friction curves for fully rough flow over a flat plate (White, 1991). This method yielded average roughness heights of 400, 550, 580, 1100, and 830 μm at X = 1.96, 5.94, 7.43, 9.23, and 10.7 m, respectively. These results are also consistent with a visual examination of the surface embedded with the particles.

3.2. Bubble Drag Reduction

3.2.1. Down-stream Persistence of Bubble Drag Reduction

Skin-friction drag reduction, *%DR*, is shown versus downstream distance from the injector (X-X_{inj}) in figures 7, 8, and 9 for the three primary test speeds (U_∞ = 6.7, 13.3, and 20.0 ms^{-1}). Both the porous-plate and slot-style injectors are shown with injection from the first injector ($X = 1.38$ m). Provided in the figures for each condition are the volumetric injection rates corrected for the static pressure in the test section. Also presented in the legend is whether that condition corresponds to BDR, ALDR, or transition between BDR and ALDR. These regions are defined subsequently, but are provided here for clarity. For the current discussion of BDR only the three lowest injection rates (2.55, 4.81, and 9.06 $m^3 min^{-1}$) at 13.3 ms^{-1} and all 20.0 ms^{-1} cases are used. Thus for the BDR conditions near the injector, high levels of drag reduction are observed and then decay rapidly with downstream distance. The decreasing drag reduction with downstream distance is associated with the migration of bubbles from the near-wall region where they are effective at reducing drag. Shear induced lift forces from the mean velocity gradients in the boundary layer are suspected of driving the bubbles from the solid surface resulting in poor persistence of drag reduction. Simple models that map the trajectory of a single bubble in an unmodified TBL have been presented in Meng and Uhlman (1989) and Sanders (2004) demonstrate this effect. As a result, at higher speeds nearly the entirety of drag reduction was lost after the first two meters.

3.2.2. Near-wall Void Fraction Measurements

Prior research has shown that gas distribution (void fraction) in the boundary layer during BDR has a peak occurring some distance (typically a few hundred wall units) from the wall (Merkle and Deutsch, 1990). Furthermore, Pal *et al.* (1989) have reported that bubbles do not reside in the viscous sub-layer region, indicating that the void fraction asymptotes to zero at the wall. This near bubble-free zone in the near-wall region has been termed the "liquid layer". The existence of a liquid layer is evidenced by the near-wall bubble imaging cameras; shown in figure 10 is a wall-normal image of the bubbly layer at $X = 5.94$ *m* and $U_\infty = 13.3$ ms^{-1} (where the measured drag reduction was about 10%). The image shows a dark region immediately adjacent to the plate surface; the dark area indicates that there are few air-water interfaces (*i.e.* bubbles) to scatter the laser light.

Electrical impedance measurements also indicate that void fraction increases with increasing distance from the wall. Only the electrical impedance measurements on the plate surface at 20.0 ms^{-1} are included here. Void fraction estimates versus $X\text{-}X_{inj}$ are shown for the two electrode pair spacings (3.2 and 6.4 *mm*, *i.e.* small and large, respectively) in figure 11. At 20.0 ms^{-1} the void fraction measurements beyond the first two meters were on the order of a few percent. Also of interest is that the void fraction measurements made by the electrodes with the larger spacing consistently show higher void fraction. The larger electrode spacing resulted in a larger "influence volume" and therefore measured the impedance of a larger portion of the boundary layer. From this, we qualitatively infer that the void fraction increased with distance from the wall, as discussed by Cho *et al.* (2005). This result agrees with the results reported by Nagaya *et al.* (2001). In figure 12 the void fraction versus $X\text{-}X_{inj}$ is shown for the four nominal injection rates to compare the two-injector geometries and the addition of surfactant, all at

20 ms^{-1} free-stream speed. Similar results were obtained with the porous-plate injector with and without surfactant in the background, and the near-wall void fractions were consistently higher with the porous-plate injector than with the slot injector. This increase in void fraction is consistent with the mild improvements observed in the drag reduction using the porous-plate injector. The skin-friction drag reduction is shown in figure 13 as a

function of the estimated near-wall mean void fraction measured by the impedance probes at 20.0 ms^{-1} for both electrode pair spacings. Both are reasonably well represented by a straight line with the smaller electrode spacing having approximately double the slope of the large spacing. This reinforces that bubble stratification away from the wall occurs near the wall.

3.2.3. *Scaling of Bubble Drag Reduction*

The scaling laws developed from previous BDR research (described in § 1) are evaluated with the present data set. First, the scaling law developed by Madavan *et al.* (1985), which assumes that drag reduction is proportional to the mean void fraction, $\overline{\alpha}$, across the *entire* boundary layer is applied and the results shown in figure 14 for the two injector styles. This scaling produces a rather poor collapse of the experimental results obtained in the present study. Second, the more recent scaling law developed by Deutsch *et al.* (2003) is implemented and the outcome is shown in figure 15, where the length scale employed is the momentum thickness, θ_o rather than the boundary layer thickness. Once more this scaling produces a rather poor collapse of the current data set.

To improve BDR scaling, we posit a new "initial zone" scaling. Following Madavan *et al.* (1984a), we begin with drag reduction as a function of the dimensionless quantity,

$$\frac{Q_a}{U_\infty S}, \tag{3.1}$$

where S is the area through which the gas is injected. In their study, gas was not injected from a line-source, but through the surface area of the plate spanning the tunnel width and 23 *cm* in the stream-wise direction. This scaling is modified to represent a nominal air-layer thickness, t_a, given by (3.2) by assuming that the injected gas is moving at the free-stream velocity, where B is now the injector span rather than the area of gas injection:

$$t_a = \frac{Q_a}{BU_\infty}. \tag{3.2}$$

Drag reduction measurements taken from the first shear-stress balance ($X-X_{inj} = 0.58\ m$) are presented in figure 16 as function of t_a. The present results show a good collapse of the data and agree well with the findings of Madavan *et al.* (1984a), whose results are also shown in figure 16. Although a reasonable collapse is evident, unfortunately this scaling yields no information about the downstream persistence of BDR.

3.2.4. Bubble Drag Reduction with Compound Injection

To investigate whether any advantage is obtained with the combination of nearby injection locations, experiments were conducted where gas was injected into the boundary layer simultaneously from two slot-type injectors spaced 2.35 *m* in the stream-wise direction. Drag reduction was measured for a variety of nominal gas injection rates at the three nominal test speeds. Aggregate gas injection rates from both injectors were limited to 22.7 *SCMM*, the maximum flow rate of a single injector. To analyze the effect of compound injection on drag reduction, the sum of drag reduction achieved with slot 1 and slot 2 independently is compared with the drag reduction obtained with the same flow rates using compound injection. In many cases it was found that there was little difference between the two, such as shown in the upper graph of figure 17 for 13.3 ms^{-1}. However, the lower graph of figure 17 shows a unique condition at 13.3 ms^{-1} where for the same aggregate injection rate, a single injector yielded much larger drag reduction than simultaneous injection from two slots. Here, injecting the full gas flux from slot 1, produced near 100% drag reduction over the entire plate. This observation is a result of the transition from BDR to ALDR, which will be discussed later in the paper. In contrast, no stable air film was formed when the gas flow-rate was split evenly between the two injectors – the drag reduction decayed drastically – even if the total volume was larger than the single injector case. These results indicate that there are no synergistic effects of compound injection that improve efficiency of BDR over the range of parameters investigated; rather, splitting the gas injection between two injectors can actually reduce the total drag reduction by preventing a transition from BDR to ALDR.

3.2.5. Influence of Injector Geometry

The skin-friction drag reduction results presented in figures 7 through 9 indicate that changes in the injector geometry as tested has only a weak effect on either the effectiveness or the downstream persistence of BDR. However, rather consistently at all speeds and injection rates, slightly higher levels of drag reduction were observed with the porous-plate injector than with the slot injector, although the differences lie within the uncertainty of the measurements. This result qualitatively agrees with the findings of Madavan *et al.* (1985), who showed that gas injection from porous-plate injectors with two different pore diameters (0.5 and 100 μm) showed measurable yet minor differences in drag reduction.

3.2.6. Influence of Surface Tension on BDR

To investigate the influence of bubble size on drag reduction, a surfactant was employed to reduce the surface tension and, in theory, the bubble size. A common soluble surfactant (Triton-X-100) was added to the background volume of the test facility at a concentration of 15 *wppm*. Winkel *et al.* (2004) showed that this can reduce bubble size by a factor of two, at least near the injector. The surface tension of samples from the tunnel volume was measured with an *in situ* tensiometry device, which is described in Lapham *et al.* (1999). The surface tension of the tunnel volume was measured to be 70 ± 1 $dyne\ cm^{-1}$ prior to the addition of the surfactant and about 50 ± 2 $dyne\ cm^{-1}$ during testing. The surfactant employed, Triton-X-100, has been shown to have time dependent properties by Lapham *et al.* (2001), but repeated measurements during the surfactant test period revealed that less than 3 $dyne\ cm^{-1}$ change occurred. Drag reduction at 13.3 and 20.0 ms^{-1} for the porous-plate injector, with and without surfactant in the tunnel volume, are compared in figure 18, exhibiting little significant difference in drag reduction. Although there was a measurable difference in surface tension, the bubble cameras showed little or no measurable reduction in bubble sizes (table 2) in the near-wall region, in contrast to the findings reported by Winkel *et al.* (2004) where measurements were made immediately downstream of injection. However, the observation that drag reduction performance was unaffected by the addition of surfactant agrees with the findings of Takahashi *et al.* (2001). In addition, histograms of the bubble populations in the near-wall region at 20.0 ms^{-1} are shown in figure 19 for the 5.66 and 22.7 *SCMM* injection rates for the porous-plate, slot, and surfactant (porous) injection tests. This shows that bubble sizes downstream from the injector are independent of injector design and background surface tension, and that the mean bubble diameters increase with increasing gas injection rate.

3.2.7. Influence of Boundary Layer Thickness

The influence of boundary layer thickness at the line of injection on drag reduction is shown in figure 20, comparing the drag reduction results for a single injection rate from either slot 1 ($X = 1.38\ m$) or slot 2 ($X = 3.73\ m$) at 13.3 and 20.0 ms^{-1}. Although the data points are rather sparse, the data appear to collapse, indicating that boundary layer thickness at the line of injection may have minimal influence on the magnitude or persistence of BDR. The ratio (slot 2 / slot 1) of the boundary layer thickness and friction velocities are about two and one, respectively. Therefore, while the boundary layer thickness did change for the two cases, the resulting drag reduction was not strongly influenced. This brings into doubt scaling based solely on outer variables, such as that proposed by Madavan *et al.* (1985) and Sanders *et al.* (2006) where TBL thickness is a length used to scale *%DR*.

3.3. AIR LAYER DRAG REDUCTION

3.3.1. The Abrupt Transition to Air Layer Drag Reduction

Under certain conditions, drag reduction approaching 100% was achieved over the entire downstream length of the test model (approximately 10 *m* in length). This high level of drag reduction resulted from the formation of an air-layer between the model and the liquid flow. The formation of an air-layer is evidenced by dark images from the near-wall cameras as none of the laser light was scattered from air-water interfaces, by the saturation of the electrical impedance probes at values approaching the impedance measured in air, and by the qualitative images from an oblique view of the lower plate surface from outside the tunnel during the second phase of the present experiments.

Sanders *et al.* (2006) achieved air layer drag reduction for only a limited set of flow conditions. Reported here are the results from a series of experiments meant to investigate the conditions necessary to achieve air layers and hence ALDR. Experiments were conducted only for the porous-plate injector (with and without surfactant in the tunnel background) from the upstream location ($X = 1.38$ *m*) at four free-stream speeds, nominally 6.7, 8.9, 11.1, and 13.3

ms^{-1}. ALDR was not observed at speeds higher than 13.3 ms^{-1} in this first set of experiments due to the limitations in the capacity of the gas delivery and metering systems. (In § 3.2.3 additional experiments with surface roughness added are discussed and speeds to 15.3 ms^{-1} are reported.) For each free-stream speed, the gas injection was varied slowly (approximately 0.142 to 0.283 *SCMM* s^{-1}) from zero using a manual controlled valve, until a maximum level of drag reduction was observed over the entire length of the test model. Once a maximum level of drag reduction was observed, the flow rate was decreased slowly to zero injection. No appreciable differences were observed in drag reduction values when increasing or decreasing gas flow rates were employed, *i.e.* no hysteresis was observed.

From the varying injection rate experiments, *%DR vs.* volumetric gas injection rate per unit span, q, curves were generated at a given flow-speed and downstream location. *%DR* versus q is presented in figure 21 for four sensor locations and a flow speed of 11.1 ms^{-1}. As observed in BDR, over the lower-range of gas injection rates, *%DR* decreases with downstream distance. However, above a critical gas injection rate, q_{crit} (see figure 23), high levels of drag reduction were observed with no apparent decay with downstream distance over the entire downstream test surface.

To investigate further the transition from BDR to ALDR, we examine more carefully another location, $X\text{-}X_{inj} = 6.05$ *m*, not shown in figure 21. Three distinct regimes are apparent and identified in figure 22 with $\%DR$ versus q for 11.1 ms^{-1}: Region I – BDR zone where $\%DR$ increases linearly with gas injection rate; Region II - A transition zone between BDR and ALDR where the $\%DR$ versus q slope increases dramatically relative to region I, but still exhibits linear change; and Region III – ALDR zone where the level of drag reduction has reached a maximum

(~ *100%*) and increasing the gas injection-rate shows little or no improvement in drag reduction due to the near complete elimination of friction drag. Two gas injection rate thresholds are defined; a transition threshold, q_{trans}, and a critical gas injection rate for ALDR, q_{crit}. These gas injection rates are located at the break point (abrupt slope change) between regions I and II (q_{trans}) and between regions II and III (q_{crit}) as seen in figure 22. Shown in figure 23 are the results for q_{crit} and q_{trans} from the primary experiment without surfactant in the background that define the transition between drag reduction regimes.

3.3.2 Scaling of Air Layer Drag Reduction

The gas injection rate thresholds are observed to be influenced strongly by the free-stream velocity, as observed in figure 23 for the porous-plate injector without surfactant. The critical gas injection rates per unit span with and without surfactant in the tunnel background are shown in figure 24 as a function of free-stream velocity, U_∞. The lines shown in figure 24 are least mean-square-error quadratic fits to the experimental data. Interestingly, the gas requirement for ALDR is about 5 to 10% higher with surfactant in the tunnel background. This implies that the interfacial tension plays a role in the formation and/or the stability of the air layer. Though we do not fully understand this, we conjecture that the reduced surface tension (with surfactant present) allows the liquid-gas interface to deform more readily (decreased pressure with the same curvature);

hence the liquid-gas interface allows larger fluctuations to occur, and a larger flux of gas is required to maintain the air layer. In addition, the small difference seen in figure 18 that shows less *%DR* with surfactant than without surfactant may manifest itself here.

Additionally, if a true air-layer is formed between the model surface and the outer-flow, the nominal thickness of the air layer, t_a, can be estimated using (3.2), $t_a = Q_A / BU_\infty$, the same parameter used successfully for the "initial zone" scaling of BDR. Although no measurements of the velocity of the gas-phase were recorded, it is assumed presently that they are on the order of and proportional to the liquid free-stream velocity. Again, when the critical gas injection rate is plotted with the corresponding nominal thickness, t_a, a linear relationship is observed as shown in figure 25. And as can be seen in the figure, values of t_a from approximately 4 to 8 *mm* were required to maintain an air-layer over the entire test model.

To provide perspective for our ALDR results, we resort to other large-scale experiments. The large-scale model tests on flat bottom models, to 50 *m* in length, by the Japanese group at the National Maritime Research Institute (i.e. Kodama and co-workers) have exceeded the gas injection rates used here. However, a persistent air-layer with dramatic drag-reduction was not observed over the length of their models. At a speed of 7 ms^{-1}, with t_a about 4 *mm*, drag reduction exceeding 40% was not observed beyond the first few meters of the 50 *m* test model of Kodama *et al.* (2002). The difference is possibly the result of span-wise gas diffusion on their test models. The test models used were at most one meter in width, with gas injected over only the center 50%. Kodama *et al.* (2002) report that the span-wise uniformity of drag-reduction was quite poor; it decreased linearly from the centerline to almost zero at the edge of the model. In addition, it is possible that gas could have escaped from beneath the test model as the models had no "skegs" to help capture the air beneath the ship. Contrastingly, in the present experiments, gas was injected over nearly 90% of the test model and it was "trapped" underneath the model by the tunnel walls (*i.e.* the model spanned the entire width of the test section) perhaps explaining the difference in results.

3.3.3 Roughness Effects on ALDR

The first supplementary experiment to better understand ALDR was that of the roughened model surface. As this configuration used a different injector design (Slot B rather than the porous-plate), data were collected once again, as described above, initially on the smooth model for free-stream speeds ranging from 6.7 to 15.3 ms^{-1}. At the highest free-stream speed, 15.3 ms^{-1}, ALDR was observed on the skin-friction balances, but the required air flux exceeded the flow meter calibration range. At the conclusion of these additional smooth surface experiments, the model was roughened and data were collected for free-stream speeds ranging from 6.8 to 12.5 ms^{-1}. Figure 26 shows q_{crit} for the two smooth model tests and the rough model experiment with outline data points corresponding to results that exceeded the calibration range of the flow meter. As is evident in the figure, while ALDR was observed for a given speed, it required about a 30 to 50% larger volumetric gas flux to transition than did the smooth plate. Note further that the lower two curves in the figure exhibit reasonable repeatability – these first and second experiments with the hydraulically smooth plate were conducted about a year apart.

Video imaging of the flow captured the transition to and from BDR and ALDR as the flow evolved. The imager was mounted below the test surface and had a view of a fixed location about five meters downstream of the leading edge. Figure 27 displays images from the video at three times during the injection process with a free-stream speed of 6.8 ms^{-1}. Figure 27 (left) was recorded prior to air injection and shows the roughened model surface; figure 27 (center) was recorded prior to achieving the critical volumetric flux to transition to ALDR (*i.e.* during BDR); and figure 27 (right) was recorded following the transition to ALDR. During BDR (middle), the layer adjacent to the plate is opaque and the hatch and sampling port (small rectangle in upper right used for a separate experiment) that are visible in the left image are no longer evident. Once transitioned to ALDR (right), the layer becomes near-transparent again as evidenced by the reappearance of the sampling port. These images support the concept that transition from BDR to ALDR corresponds to a change in flow regimes.

3.3.4 The Importance of Inflow Conditions: Use of a Faired Step

In a third experiment to investigate air layers (as well as air cavities), we discovered that uniformity and lack of large (with respect to the LCC) turbulent eddies (on the order of 1 *cm*) in the inflow TBL to the injection location was required to obtain ALDR with flush injection. This has important ramifications for implementation of ALDR. In the LCC, the disturbances were caused by an attempt at *in situ* repairs to the test model surface upstream of the injector that resulted in a highly disturbed TBL upstream of the injector. After observing that we could no longer achieve ALDR at equivalent gas fluxes, a different injector configuration was implemented. This setup included a 1-*cm* step, faired upstream into the nose of the plate. Once installed, the step provided a clean separation line for the flow between the gas and the liquid. This allowed for the formation of air layers, although at increased air-flux. This result indicates that care must be taken to insure that the TBL upstream of air-layer formation should be free of large-scale non-uniformity, and that the use of a small step will help insure a clean flow separation for the air layer, even if the incoming TBL is not highly uniform.

4. Summary and Conclusions

From the high-Reynolds-number drag reduction experiments conducted on the test model, the following conclusions can be drawn with regard to bubble drag reduction (BDR). 1) Prior scaling laws developed by Madavan *et al.* (1984a), Deutsch *et al.* (2003), and Sanders *et al.* (2006) do not adequately collapse BDR and ALDR data for the range of parameters investigated here. 2) The present results collapse using an "initial zone" scaling and agree reasonably well with the results of Madavan *et al.* for the sensor immediately (0.6 *m*) downstream of the gas injector. 3) Drag reduction decays rapidly with downstream distance at higher free-stream speeds and drag reductions exceeding 10-20% were not observed beyond about two meters at 20.0 ms^{-1}. 4) Injector geometry has only a marginal effect on the magnitude or persistence of drag reduction, at least for the two different geometries here. 5) Reducing the surface tension by employing a surfactant has little effect on BDR away from the injector. 6) Downstream of the injector decreasing the surface tension has negligible effects on bubble size. 7) Changes of TBL thickness by a factor of about two at the point of injection has little or no influence on BDR. And, 8) Compound injection (gas injection through two injectors spaced in the stream-wise direction) showed no "synergistic" effects (*i.e.* no improvement over injecting the entire flux through a single injector), and under certain conditions compound injection can reduce drag reduction by preventing the transition to ALDR.

The following conclusions can be gleaned from the air layer drag reduction (ALDR) experiments conducted on the test model. 1) Drag reduction can be divided into three distinct regions: Region I) a BDR zone, where DR grows linearly with gas injection rate; Region II) a "transition zone" where drag reduction increases linearly with a much steeper slope than in Region I; and Region III) an ALDR zone characterized by a thin air film between the test model surface and the liquid free-stream where 90% ± 10% drag reduction is observed and hence increasing injection rate yields little or no improvement in drag reduction. 2) The "critical" gas injection rate required to form a persistent air layer is approximately proportional to the square of the free-stream liquid velocity (or linearly proportional to the nominal air layer thickness, $t_a = Q_a / BU_\infty$). 3) The "critical" gas injection rate was observed to increase slightly with surfactant solution in the tunnel volume. A drop in surface tension from 70 to ~ 50 $dynes\ cm^{-1}$, increases the gas requirements by ~10%, implying that surface tension plays a role in the formation and stability of an air layer. 4) ALDR was observed to persist over the entire length of model (X-X_{inj} ~ 10 m) at speeds to 15.3 ms^{-1} with no decay in the level of drag reduction. Therefore, it is conjectured that ALDR may have persistence lengths much greater than the length of the current test model. 5) Significantly increasing the surface roughness results in an increase in the critical volumetric flux to transition to ALDR, but a stable air layer still forms and was observed to free-stream speeds of 12.5 ms^{-1}. 6) Inflow conditions significantly affect the stability and formation of the air layer, but this deficiency can be mitigated through the use of clean separation lines *via* a faired step.

ACKNOWLEDGMENT

The authors would like to thank the technical staff of the US Navy's William B. Morgan Large Cavitation Channel, especially Dr. J. Michael Cutbirth and Mr. Robert Etter. Mr. Kent Pruss, Mr. William Kirkpatrick and co-workers of the UM machine shops contributed substantially to the construction of the test model and instrumentation. Dr. Duncan Brown of the Johns Hopkins University Applied Physics Laboratory and Dr. Howard Petrie of the Pennsylvania State University provided helpful insight and advice. Others who have contributed to this research include Dr. Ghanem Oweis, Dr. Wendy Sanders, Dr. Shiyao Bian, Dr. Xiaochun Shen, Dr. Jaehyug Choi, Dr. Chinar Aphale, Dr. Natasha Chang, and Mr. Ruben DeBruin. This research was sponsored by DARPA under Contracts HR0011-04-1-001 and HR0011-06-1-0057 (Dr. Thomas Beutner, Program Manager) and by ONR under Contract N00014-06-1-0244 (Dr. L. Patrick Purtell, Program Manager). The content of this document does not necessarily reflect the position or the policy of the United States Government, and no official endorsement should be inferred.

REFERENCES

Bodgevich, V. G. & Evseev, A. R. 1976 The distribution of skin friction in a turbulent boundary layer of water beyond the location of gas injection. *Investigations of Boundary Layer Control* (in Russian), Thermophysics Institute Publishing House, **62**.

Ceccio, S. L. & George, D. L. 1996 A review of electrical impedance techniques for the measurement of multiphase flows. *Journal of Fluids Engineering* **118**, 391-399.

Cho, J., Perlin, M., & Ceccio, S. L. 2005 Measurement of near-wall stratified bubbly flows using electrical impedance. *Measurement Science and Technology* **16**, 1021-1029.

Clark, H. & Deutsch, S. 1991 Microbubble skin friction reduction on an axisymmetric body under the influence of applied axial pressure gradients. *Physics of Fluids* **A3**, 2948-2954.

Deutsch, S., Money, M., Fontaine, A., & Petrie, H. 2003 Microbubble drag reduction in rough walled turbulent boundary layers. *Proceedings of the ASME-Fluids Engineering Division Summer Meeting* 2003, 1-9.

Druzhinin, O. A. & Elghobashi, S. 1998 Direct numerical simulations of bubble-laden turbulent flows using two-fluid formulation. *Phys. Fluids* **10**, 685–697.

Etter R. J., Cutbirth, J. M., Ceccio, S. L., Dowling, D. R., & Perlin, M. 2005 High Reynolds Number Experimentation in the U. S. Navy's William B. Morgan Large Cavitation Channel. *Measurement Science and Technology*, **16(9)**, 1701-1709.

Fontaine, A. A. & Deutsch, S. 1992 The influence of the type of gas on the reduction of skin friction drag by microbubble injection. *Experiments in Fluids* **13**, 128-136.

George D.L., Iyer, C.O. and Ceccio, S.L. 2000 Measurement of the Bubbly Flow Beneath Partial Attached Cavities Using Electrical Impedance Probes. *Journal of Fluids Engineering*, **122**, 2000.

Hewitt, G.F. 1978 *Measurement of Two-Phase Flow Parameters*. Academic Press, London.

Kawakita, C. & Takano, S. 2000 Microbubble skin friction reduction under the influence of pressure gradients and curved surfaces. *Journal of the Society of Naval Architects of Japan*, **188**, 11 – 21.

Kawamura, T., Moriguchi, Y., Kato, H., Kakugawa, A., & Kodama, Y. 2003 Effect of bubble size on the microbubble drag reduction of a turbulent boundary layer. *Proceedings of the ASME Fluids Engineering Conference Summer Meeting* 2003, 1-8.

Kodama, Y., Kakugawa, A., & Takahashi, T. 1999 Preliminary experiments on microbubbles for drag reduction using a long flat plate ship. *ONR Workshop on Gas Based Surface Ship Drag Reduction* (Newport, USA), 1-4.

Kodama, Y., Kakugawa, A., Takahashi, T. & Kawashima, H. 2000 Experimental study on microbubbles and their applicability to ships for skin friction reduction. *Intl J. Heat Fluid Flow* **21**, 582–588.

Kodama, Y., Kakugawa, A., Takahashi, T., Nagaya, S., & Sugiyama, K. 2002 Microbubbles: drag reduction mechanism and applicability to ships. *24th Symposium on Naval Hydrodynamics*, 1-19.

Kodama, Y., Hori, T., Kawashima, M. M., & Hinatsu, M. 2006 A full scale microbubble experiment using a cement carrier. *European Drag Reduction and Flow Control Meeting*, Ischia, Italy, 1-2

Lapham, G.S., Dowling, D.R., & Schultz, W.W. 1999 In situ force-balance tensiometry. *Experiments in Fluids*,**27**, 157-166.

Lapham, G. S., Dowling, D. R., & Schultz, W. W. 2001 Linear and nonlinear gravity-capillary water waves with a soluble surfactant. *Experiments in Fluids* **30** (4), 448-457.

Lu, J., Fernández, A., & Trygvasson, G. 2005 The effect of bubbles on the wall drag of a turbulent channel flow. *Physics of Fluids* **17**, Paper #095102

Lumley, J. L. 1973 Drag reduction in turbulent flow by polymer additives. *J Polymer Science, Macromolecular Rev.*, **7**, 283–290.

Lumley, J. L. 1977 Drag reduction in two phase and polymer flows. *Physics of Fluids* **20**, S64-S70.

Madavan, N. K., Deutsch, S., & Merkle, C. L. 1984a Reduction of turbulent skin friction by microbubbles. *Physics of Fluids* **27**, 356-363.

Madavan, N. K., Deutsch, S., & Merkle, C. L. 1984b Numerical investigation into the mechanisms of microbubble drag reduction. *ASME Journal of Fluids Engineering* **107**, 370-377.

Madavan, N. K., Deutsch, S., & Merkle, C. L. 1985 Measurements of local skin friction in a microbubble modified turbulent boundary layer. *Journal of Fluid Mechanics* **156**, 237-256.

Maxwell, J. 1881 *A Treatise on Electricity and Magnetism*, Clarendon Press (Oxford, England).

McCormick, M. E. & Battacharyya, R. 1973 Drag reduction of a submersible hull by electrolysis. *Naval Engineers Journal* **85**, 11-16.

Meng, J. C. S. & Uhlman, J. S. 1989 Microbubble formulation and splitting in a turbulent boundary layer for turbulence reduction. *Advances in fluid dynamics*, New York, Springer-Verlag, 168-217.

Meng, J. C. S. & Uhlman, J. S. 1998 Microbubble formation and splitting in a turbulent boundary layer for turbulence reduction. *Proceedings of the International Symposium on Seawater Drag Reduction*, 341-355.

Merkle, C. & Deutsch, S. 1990 Drag reduction in liquid boundary layers by gas injection. Bushnell, D.M. and Hefner, J.N. (eds) *Viscous drag reduction in boundary layers, Progress in astronautics and aeronautics AIAA* **123**, 351-412.

Merkle, C. & Deutsch, S. 1992 Microbubble drag reduction in liquid turbulent boundary layers. *Applied Mechanics Review* **45** (3), 103-127.

Nagamatsu, T. Kodama, T., Kakugawa, A., Takai, M., Murakami, K., Ishikawa., Kamiirisa, H., Ogiwara, S., Yoshida, Y., Suzuki, T., Toda, Y., Kato, H., Ikemoto, A., Yamatani, S., Imo, S., & Yamashita, K. 2002 A full-scale experiment on microbubbles for skin friction reduction using SEIUN MARU Part 2: The full-scale experiment. *Journal of the Society of Naval Architects of Japan* **192**, 15-28.

Nagaya, S., Kakugawa, A., Kodama, Y., & Hishida, K. 2001 PIV/LIF measurements on 2-D turbulent channel flow with microbubbles. *4th International Symposium on PIV*, Goettingen, Germany.

Pal, S., Deutsch, S., & Merkle, C. L. 1989 A comparison of shear stress fluctuation statistics between microbubble modified and polymer modified turbulent flow. *Physics of Fluids* **A1**, 1360-1362.

Sanders, W. C. 2004 Bubble drag reduction in a flat plate boundary layer at high Reynolds numbers and large scales. Doctoral thesis, University of Michigan.

Sanders, W. C., Winkel, E. S., Dowling, D. R., Perlin, M., & Ceccio, S. L. 2006 Bubble friction drag reduction in a high-Reynolds-number flat-plate turbulent boundary layer. *Journal of Fluid Mechanics* **552**, 353-380.

Schultz-Grunow, F. 1941 New frictional resistance law for smooth plates. *NACA* T M **17**, 1-24.

Shen, X., Perlin, M., & Ceccio, S. L. 2006 Influence of bubble size on micro-bubble drag reduction. *Experiments in Fluids* **41**, 415-424.

Takahashi, T., Kakugawa, A., Nagaya, S., Yanagihara, T. & Kodama, Y. 2001 Mechanisms and scale effects of skin friction reduction by microbubbles. *Proceedings of the 2nd Symposium on the Smart Control of Turbulence*, University of Tokyo, 1-9.

van den Berg, T. H., Luther, S., Lathrop, D. P., & Lohse, D. 2005 Drag reduction in bubbly Taylor-Couette turbulence. *Physical Review Letters* **94**, Paper #044501.

Watanabe, O., Masuko, A., & Shirose, Y. 1998 Measurements of drag reduction by microbubbles using very long ship models. *Journal of the Society of Naval Architects of Japan* **183**, 53-63.

White, F. M. 1991 *Viscous Fluid Flow*, McGraw Hill, Inc.

Winkel, E. S. 2006 High Reynolds Number Flat Plate Turbulent Boundary Layer Measurements and Skin Friction Drag Reduction with Gas or Polymer Injection. Doctoral thesis, University of Michigan.

Winkel, E. S., Ceccio, S. L., Dowling, D. R., & Perlin, M. 2004 Bubble size distributions produced by wall-injection of air into flowing freshwater, saltwater, and surfactant solutions. *Experiments in Fluids* **37**, 802-810.

Tables and Figures

	Test Type	Model	Injector	Skin-Friction Measurement
Test 1a	BDR	Smooth	Porous-plate & Slot A	Local
Test 1b	ALDR	Smooth	Porous-plate	Local
Test 2a	ALDR	Smooth	Slot B	Local
Test 2b	ALDR	Rough	Slot B	Local
Test 3	ALDR (Inlet Condition)	Smooth	Slot B (Modified)	Integrated

TABLE 1: Summary of tests conducted and the experimental setup employed for the BDR or ALDR experiments. The model surface condition, injector type, and the method of skin-friction measurement are listed.

Upstream location, X =1.96 m

Injection Rate	2.55 m^3min^{-1}	4.81 m^3min^{-1}	9.06 m^3min^{-1}	15.3 m^3min^{-1}
Sintered Metal	123 μm	146 μm	130 μm	138 μm
Surfactant	135 μm	105 μm	N/A	N/A
Slot 1	106 μm	133 μm	124 μm	178 μm

Downstream location, X = 10.68 m

Injection Rate	2.55 m^3min^{-1}	4.81 m^3min^{-1}	9.06 m^3min^{-1}	15.3 m^3min^{-1}
Sintered Metal	80 μm	92 μm	90 μm	181 μm
Surfactant	76 μm	88 μm	94 μm	149 μm
Slot 1	N/A	99 μm	99 μm	209 μm

TABLE 2: The mean bubble diameters measured with the near-wall bubble cameras ($Y < 5$ mm) at the upstream and downstream locations with a free-stream speed of 20.0 ms^{-1}. Bubble diameters are tabulated for the porous-plate (sintered metal) injection, porous-plate with surfactant injection, and slot A injection.

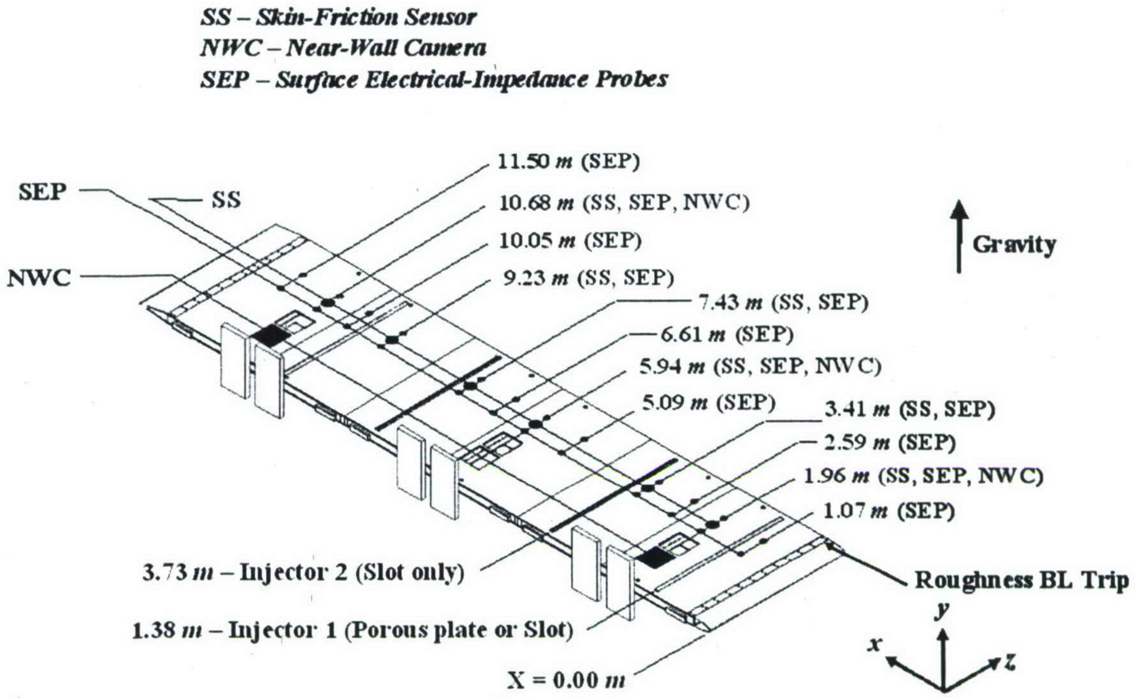

FIGURE 1. Schematic of the test model's working surface showing the injectors and instrument layout for Test 1. Gas injectors are located 1.38 and 3.73 *m* from the model's leading edge. Six skin-friction force balances and twelve surface electrical impedance probes are positioned in the stream-wise direction. Near-wall imagers are positioned at *X* = 1.96, 5.94, and 10.68 *m*.

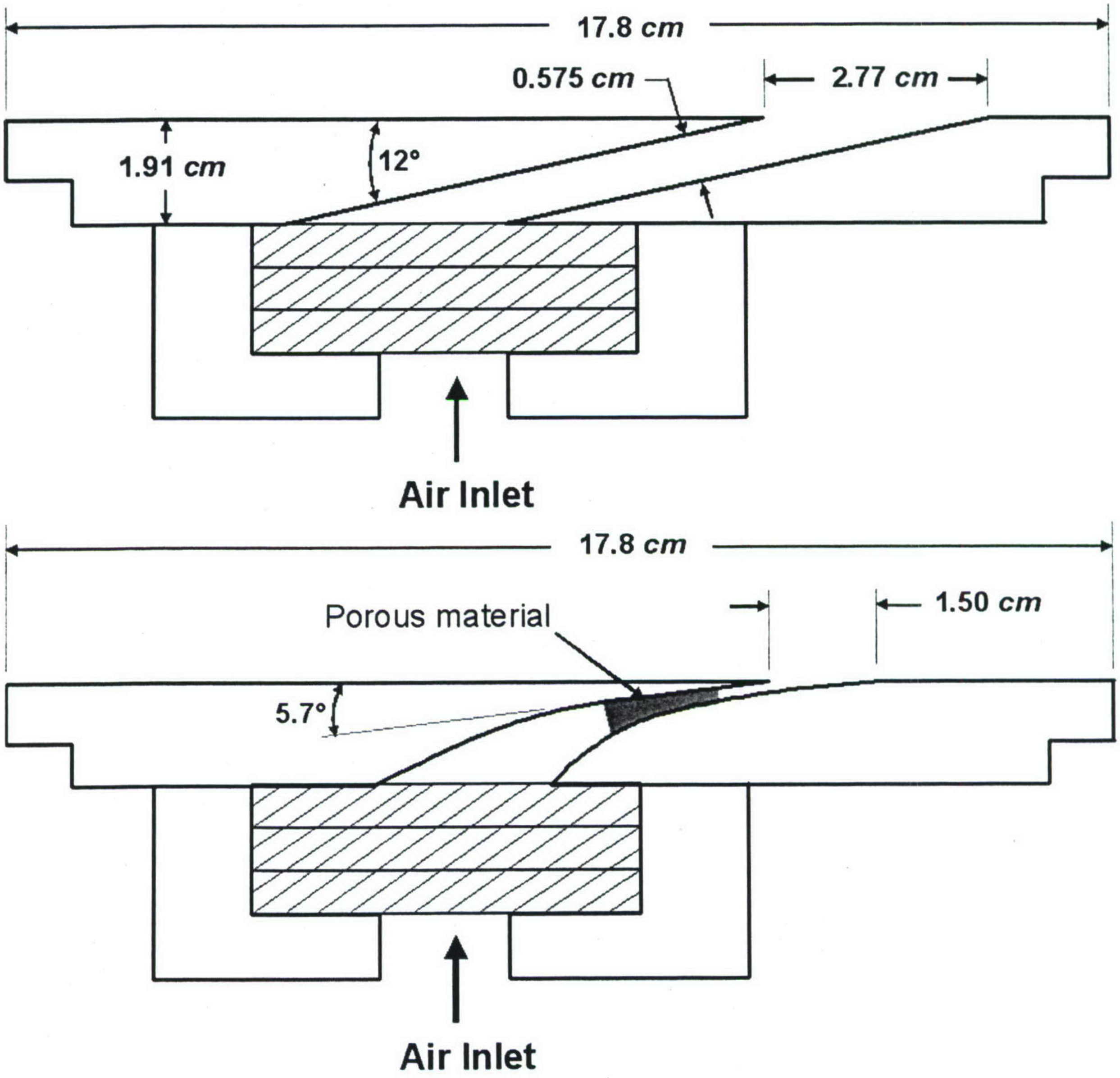

FIGURE 2. Cross-sectional schematic of (upper) Slot A used during Test 1 and (lower) Slot B used during Test 2. Test 3 used the lower injector without the porous material in the slot and a slightly modified air delivery system. Gas was distributed to the injector through 40 – 12.8 *mm* diameter ports evenly spaced along the span of the injector manifold. Three layers of baffles and screens served to create a pressure drop and evenly distribute the gas along the injector span. See Sanders *et al.* (2006) for the screen and baffle specifications.

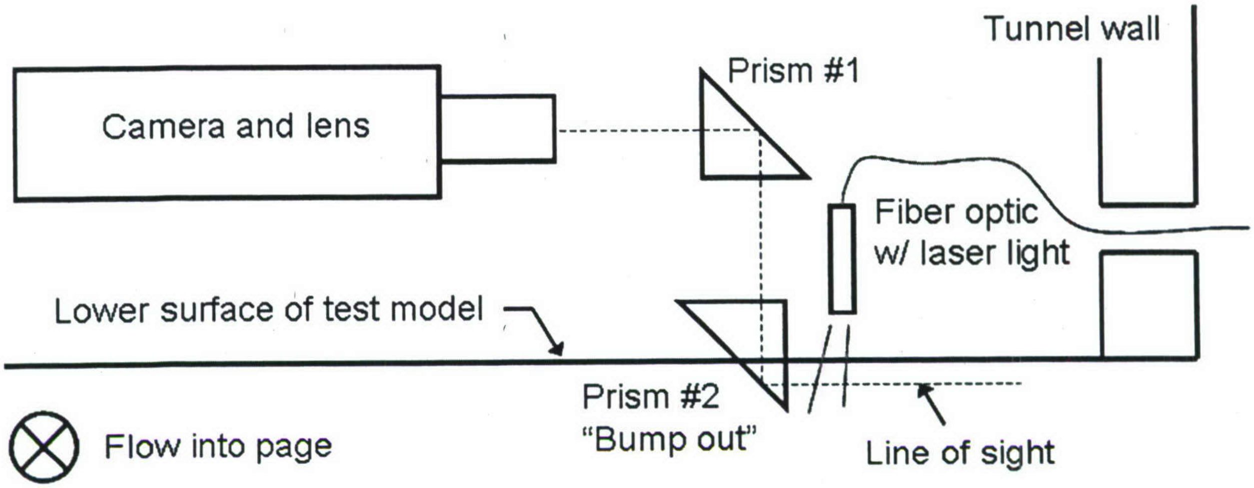

FIGURE 3. An elevation-view schematic of the near-wall imaging system used in Test 1. A periscope type assembly of two prisms was used to deflect the camera line of sight to the near-wall region. The image area was illuminated from the side using laser light delivered with a fiber optic cable.

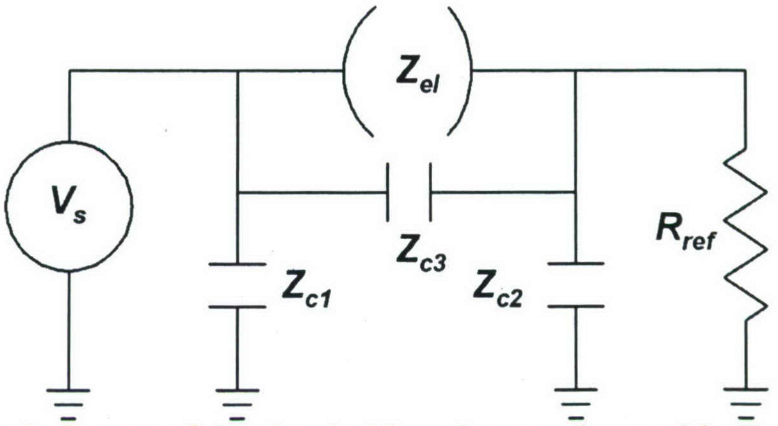

FIGURE 4: Circuit diagram of the electrical impedance probes used in Test 1. Shown is the voltage source, V_s, the impedance of the bubbly flow, Z_{el}, reference resistor, R_{ref}, and the stray capacitance from the lead wires Z_{c1}, Z_{c2}, and Z_{c3}.

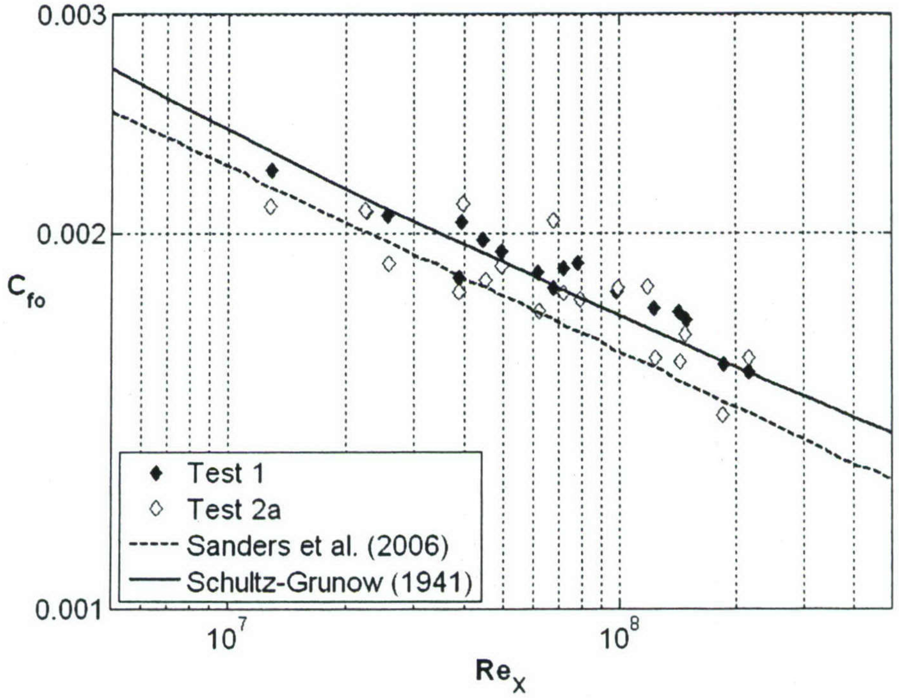

FIGURE 5: Baseline results obtained from Test 1 and 2a on the smooth model. Also shown is the best fit curve obtained by Sanders *et al.* (2006) on the same model and the Schultz-Grunow (1941) flat plate skin-friction curve.

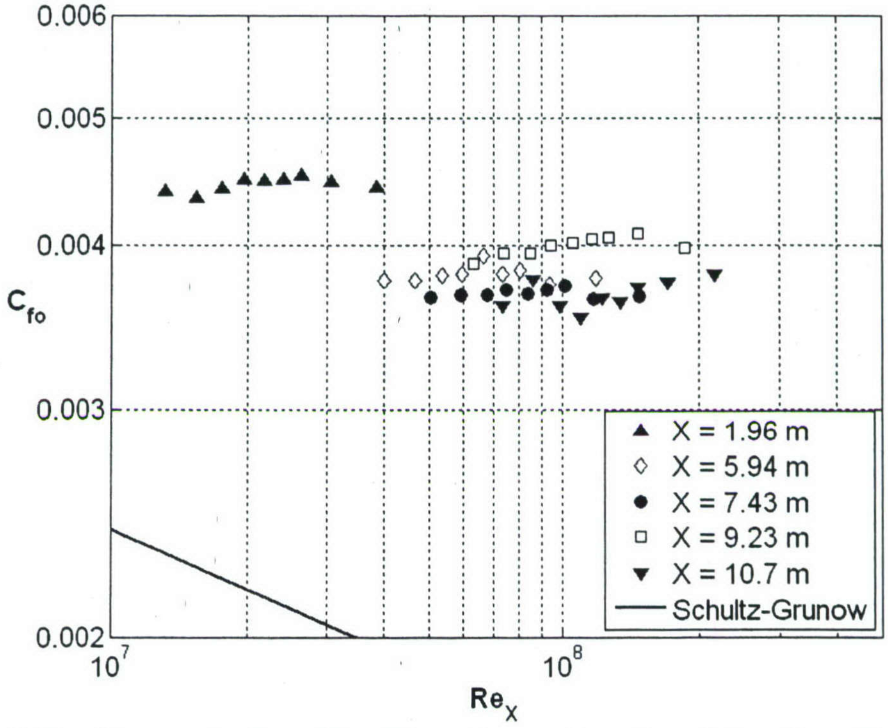

FIGURE 6: Baseline results from Test 2b on the roughened model surface. Data from each skin-friction balance are plotted separately (*X* = 1.96 to 10.7 *m*) to show the Reynolds number independence. Also shown is the Schultz-Grunow (1941) curve that approximates the smooth model baseline results.

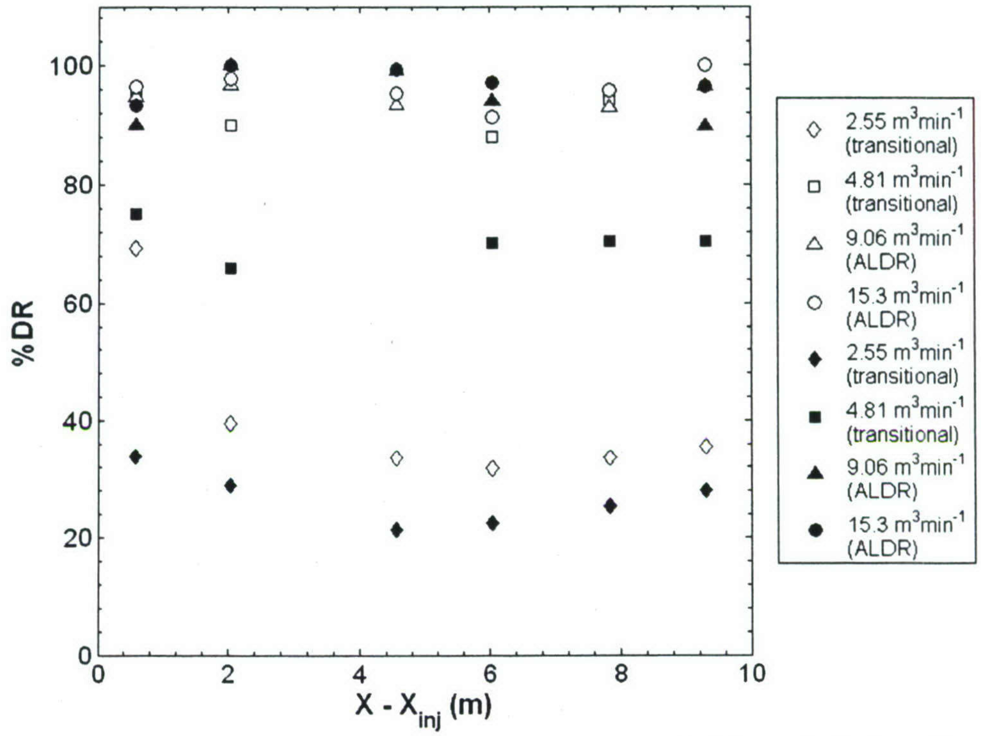

FIGURE 7: *%DR* versus *X-X_{inj}* at a free-stream speed of 6.7 ms^{-1} during Test 1. A comparison of the Slot A (solid symbols) and porous-plate (open symbols) injectors at the four gas injection rates is presented. Given in the legend is the volumetric gas injection rate corrected for test section static pressure, and in parentheses is whether this injection rate corresponds to BDR, ALDR, or the transition between BDR and ALDR.

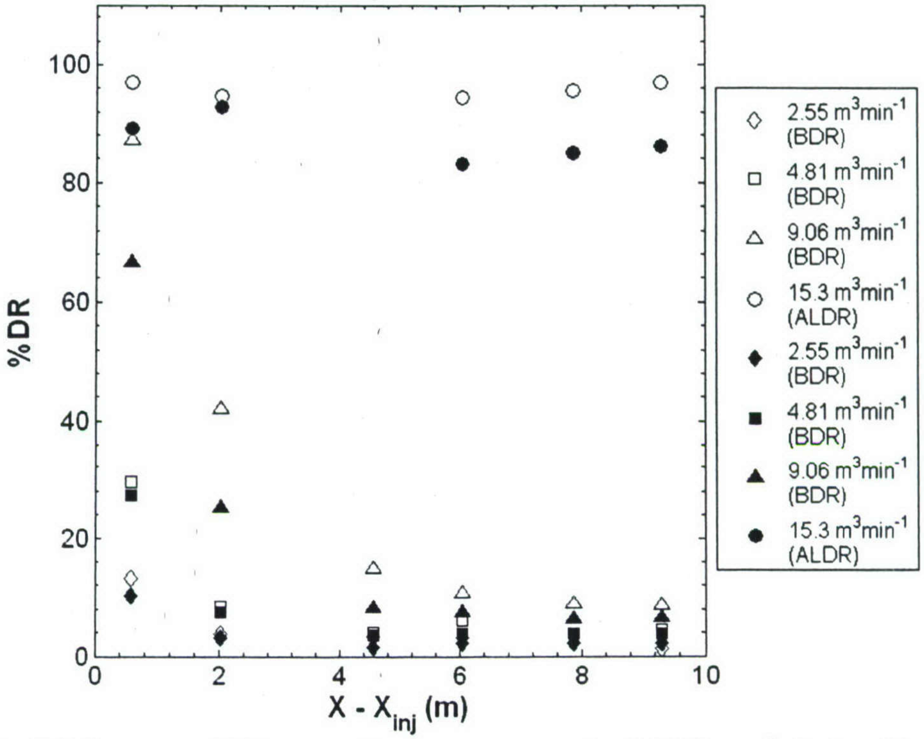

FIGURE 8: *%DR* versus *X-X*$_{inj}$ at a free-stream speed of 13.3 *ms*$^{-1}$ during Test 1. A comparison of the Slot A (solid symbols) and porous-plate (open symbols) injectors at the four gas injection rates is presented. Given in the legend is the volumetric gas injection rate corrected for test section static pressure, and in parentheses is whether this injection rate corresponds to BDR, ALDR, or the transition between BDR and ALDR.

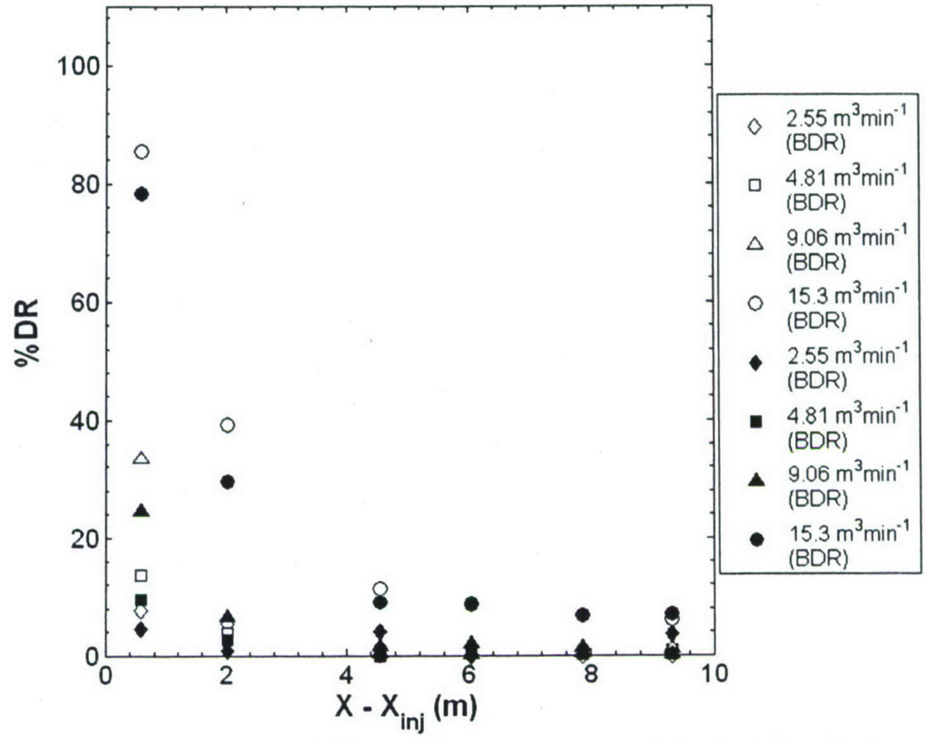

FIGURE 9: *%DR* versus $X\text{-}X_{inj}$ at 20.0 ms^{-1} free-stream speed during Test 1. A comparison of the Slot A (solid symbols) and porous-plate (open symbols) injectors at the four gas injection rates is presented. Given in the legend is the volumetric gas injection rate corrected for test section static pressure, and in parentheses is whether this injection rate corresponds to BDR, ALDR, or the transition between BDR and ALDR.

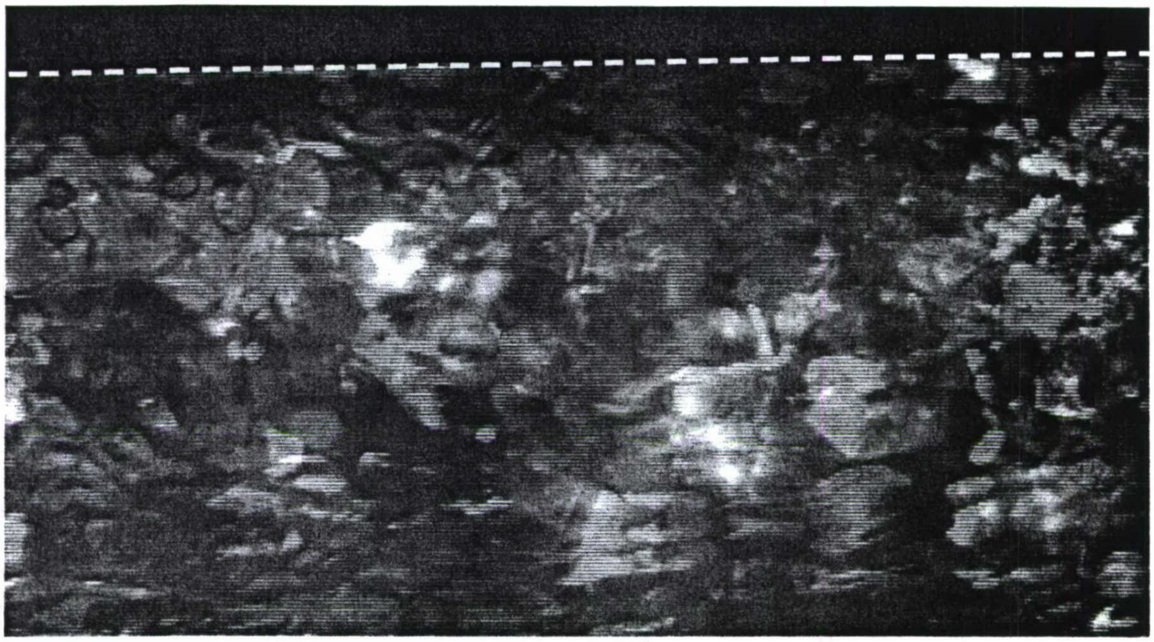

FIGURE 10: Photographic image of the near-wall bubbly flow at 13.3 ms^{-1} ($X = 5.94\ m$), 5.10 m^3min^{-1} injection (~10% %*DR*). The image is approximately 5 x 8 *mm*, and the flow is from right to left. The dark region adjacent to the wall (that is completely black and has been identified by the superposed white dashed line) exhibits the liquid-layer that is almost entirely depleted of bubbles.

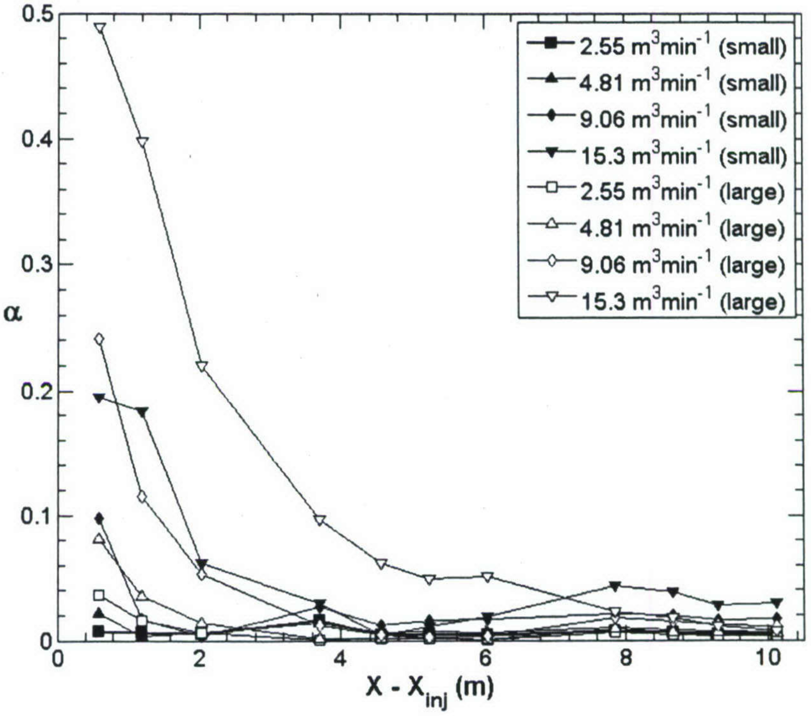

FIGURE 11: Near-wall void fraction, α, versus downstream distance from the injector at 20.0 ms^{-1} for the porous-plate injector (Test 1) measured by the surface electrical impedance probes for different gas flow rates (m^3min^{-1}). Two electrode pair spacings are shown: 3.2 *mm* (small) and 6.4 *mm* (large).

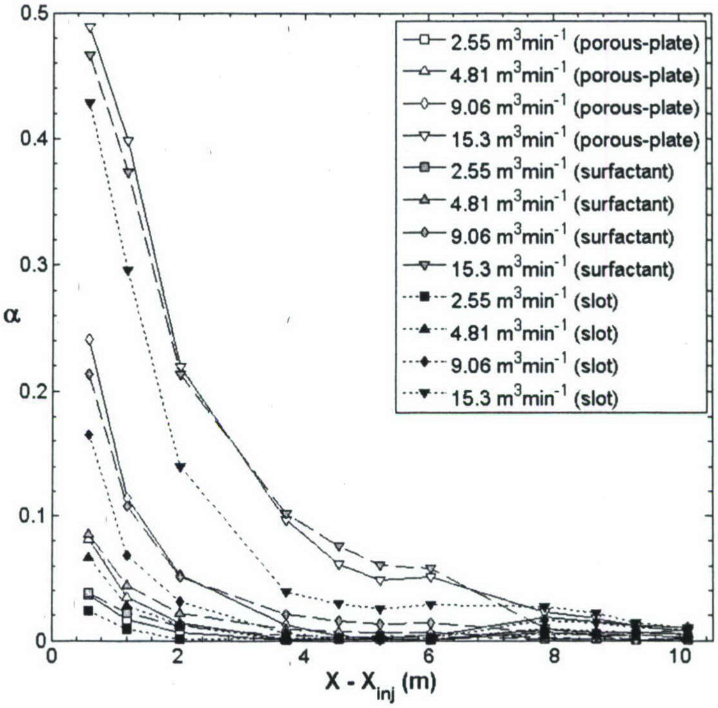

FIGURE 12: The near-wall void fraction, α, measured with electrical impedance probes versus downstream distance from the injector at the four nominal injection rates is shown for the porous-plate (with and without surfactant in the background) and upstream injection from Slot A without surfactant background. These data from Test 1 all correspond to free-stream speeds of 20.0 ms^{-1} and the large, 6.4 mm, electrode spacing.

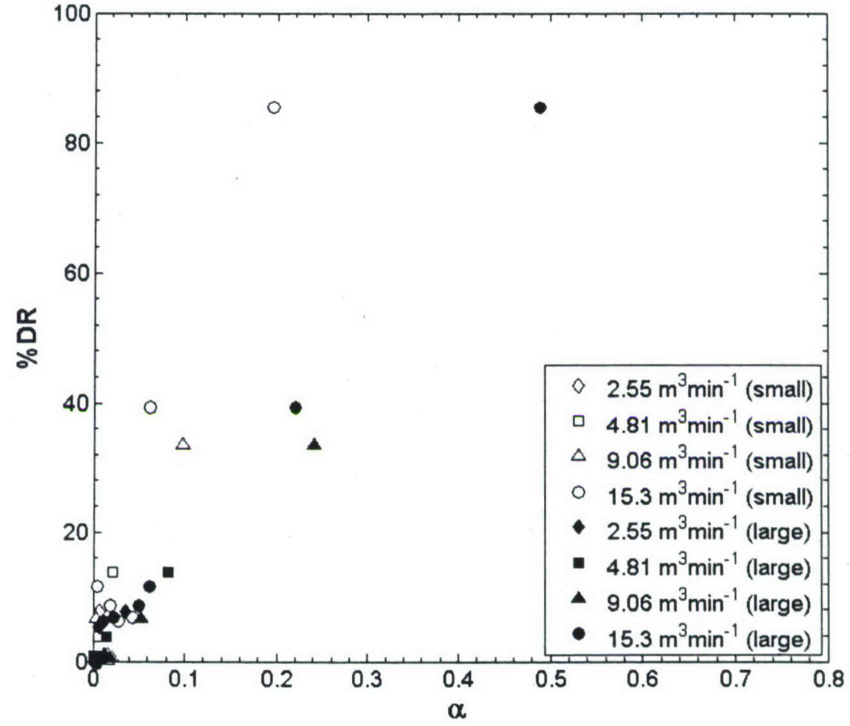

FIGURE 13: *%DR* versus α, the near-wall mean void fraction in the boundary layer measured by the surface impedance probes for the porous-plate injector at 20.0 ms^{-1} from Test 1.

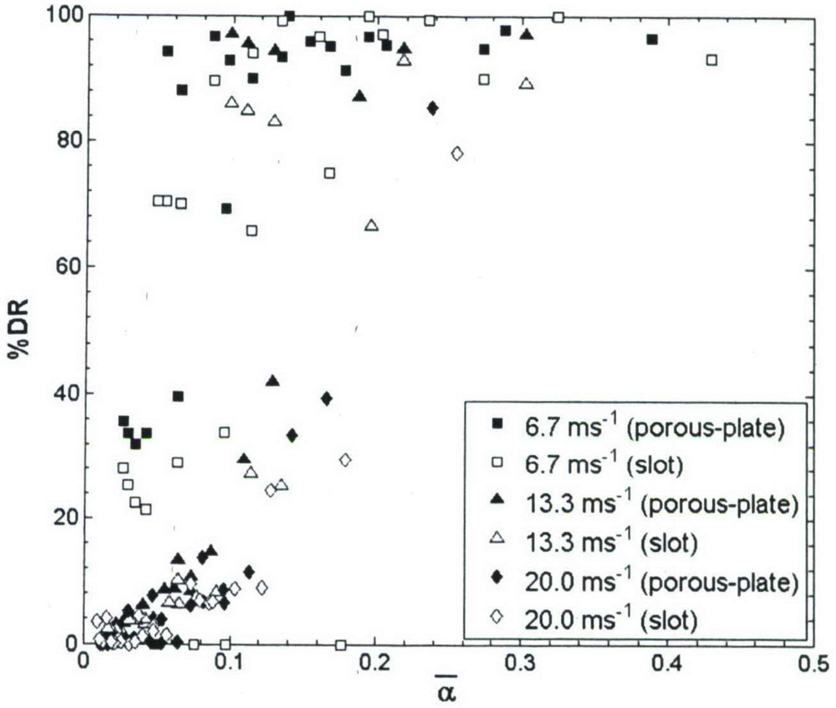

FIGURE 14: *%DR* versus $\overline{\alpha}$, the mean void fraction across the entire boundary layer, shown for the two injector styles and the three free-stream speeds from Test 1.

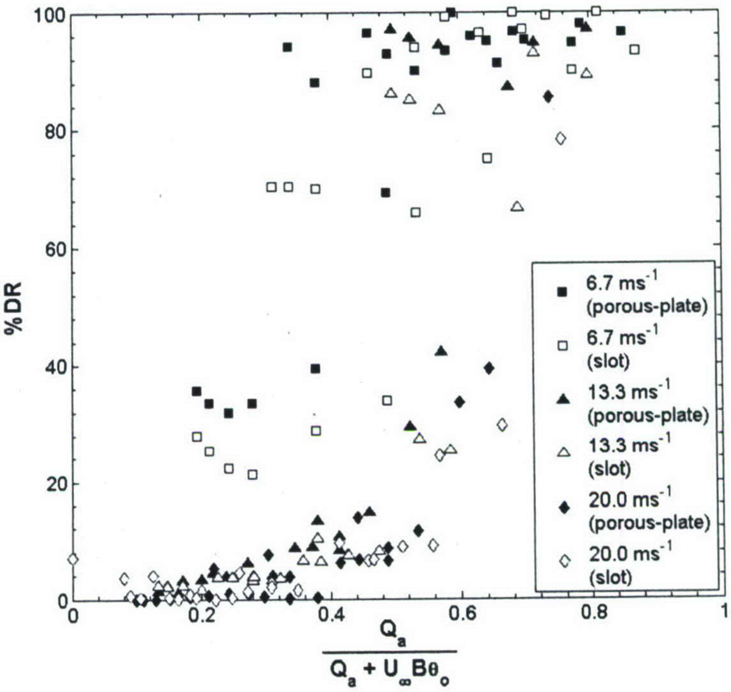

FIGURE 15: *%DR* versus the scaling of Deutsch *et al.* (2003), (1.4), for the smooth surface where $u_\tau = u_\tau^*$. Results are from Test 1 with porous-plate and Slot A injectors.

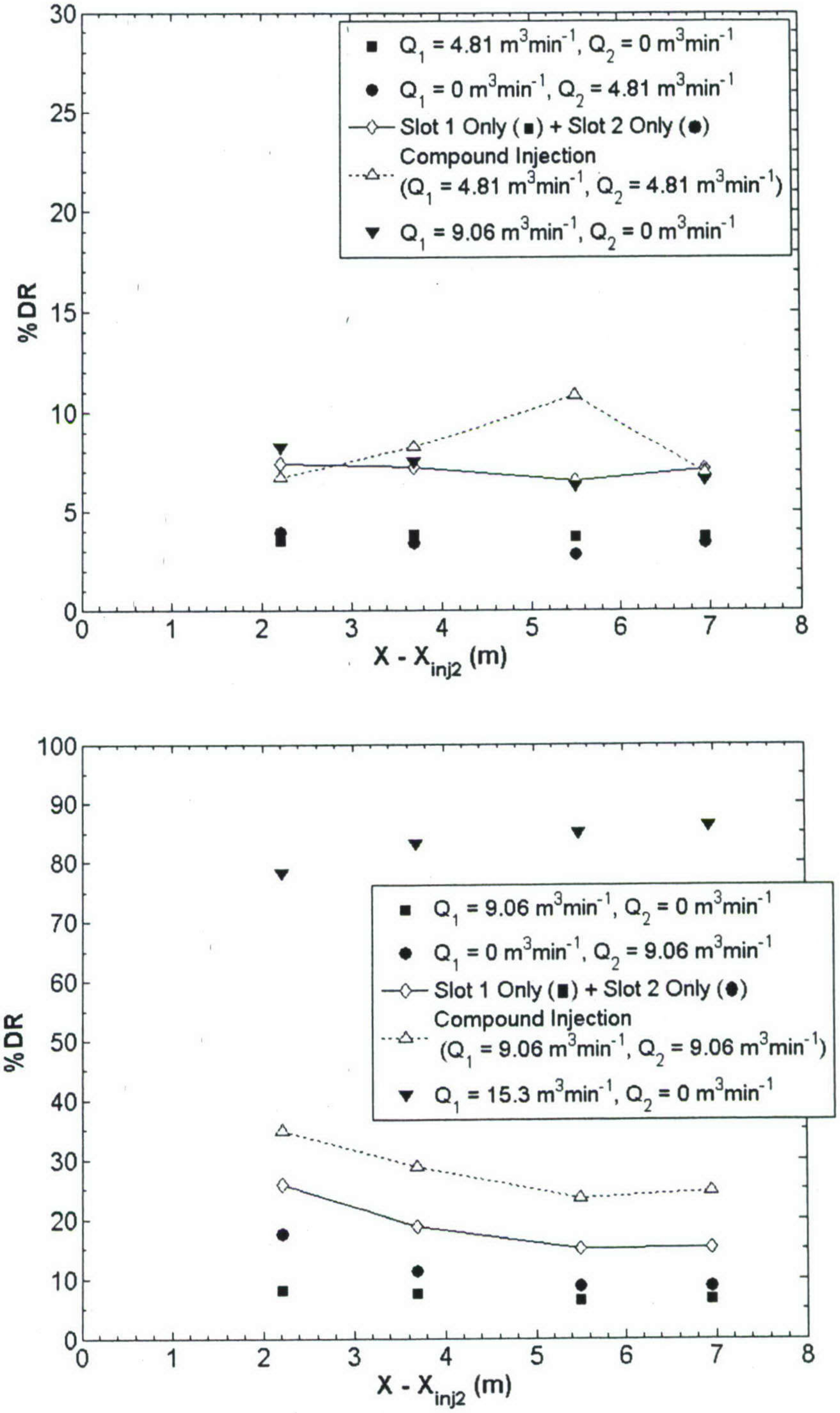

FIGURE 17: *%DR* obtained from Test 1 versus downstream distance from injector 2 ($X_{inj2} = 3.73\ m$) at 13.3 ms^{-1} with gas injection from slot 1 only, slot 2 only, and simultaneously from both slots at (upper) 4.81 m^3min^{-1} and (lower) 9.06 m^3min^{-1}. For comparison with compound injection, solid lines that represent the simple sum of drag reduction from slots 1 and 2 only (*i.e.* from the filled squares and circles) are shown; dashed lines represent compound injection. Also shown is (upper) 9.06 m^3min^{-1} and (lower) 15.3 m^3min^{-1} injected only from slot 1.

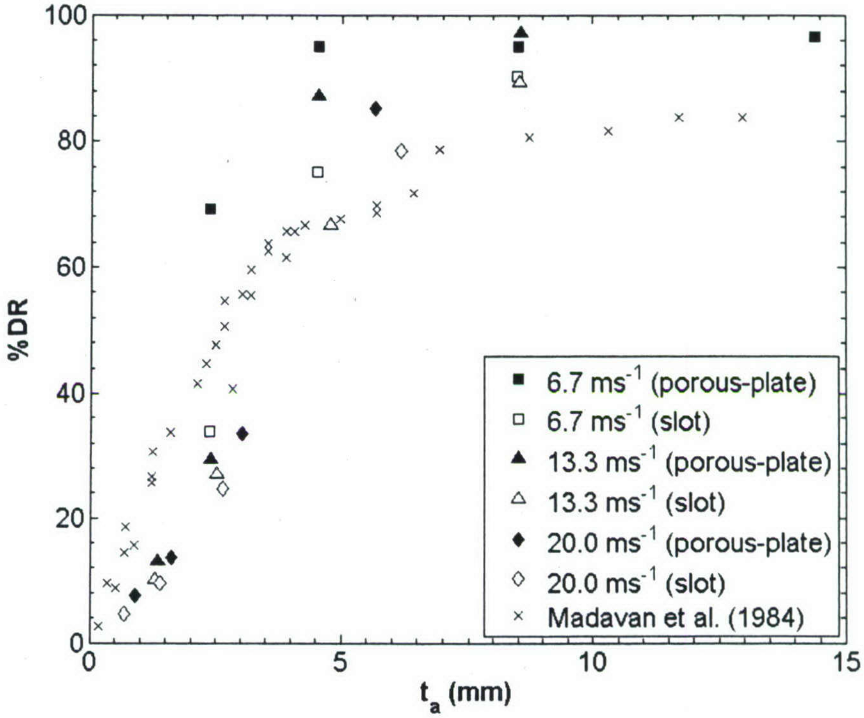

FIGURE 16: The first skin-friction balance ($X\text{-}X_{inj}$= 0.58 *m*) *%DR* versus an "initial zone" scaling nominal air-layer thickness, t_a. Data are presented for the porous-plate and slot injectors (Test 1) along with the results of Madavan *et al.* (1984a), where $X\text{-}X_{inj}$ = 0.254 *m* measured from the injector to the downstream edge of the drag balance.

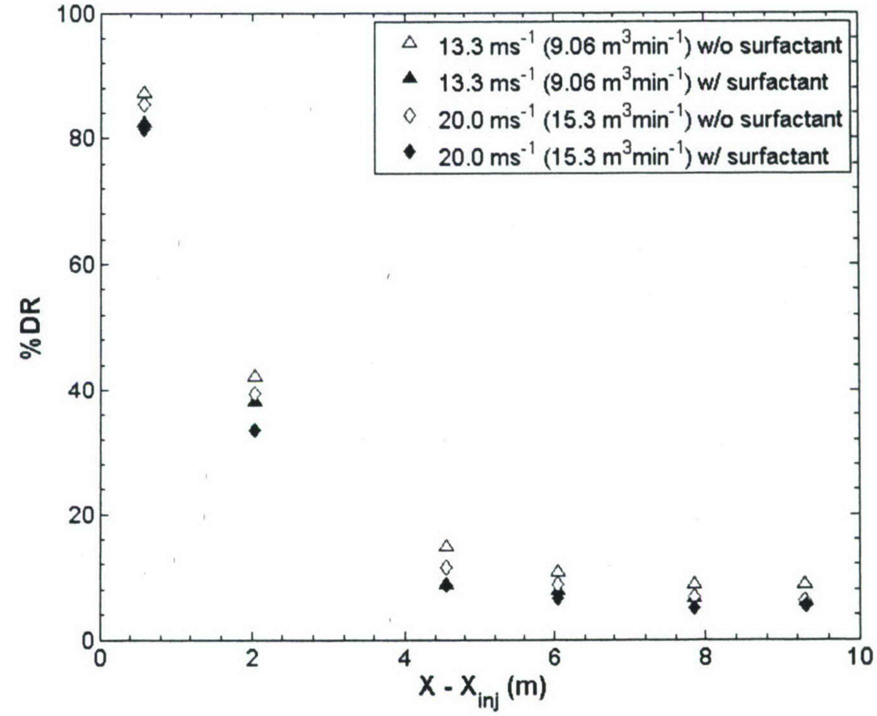

FIGURE 18: *%DR vs.* $X - X_{inj}$ using the porous-plate injector with and without surfactant in the background. Results from Test 1 indicate negligible differences in drag reduction with the reduction in surface tension from 70 to about 50 *dynes* cm^{-1}.

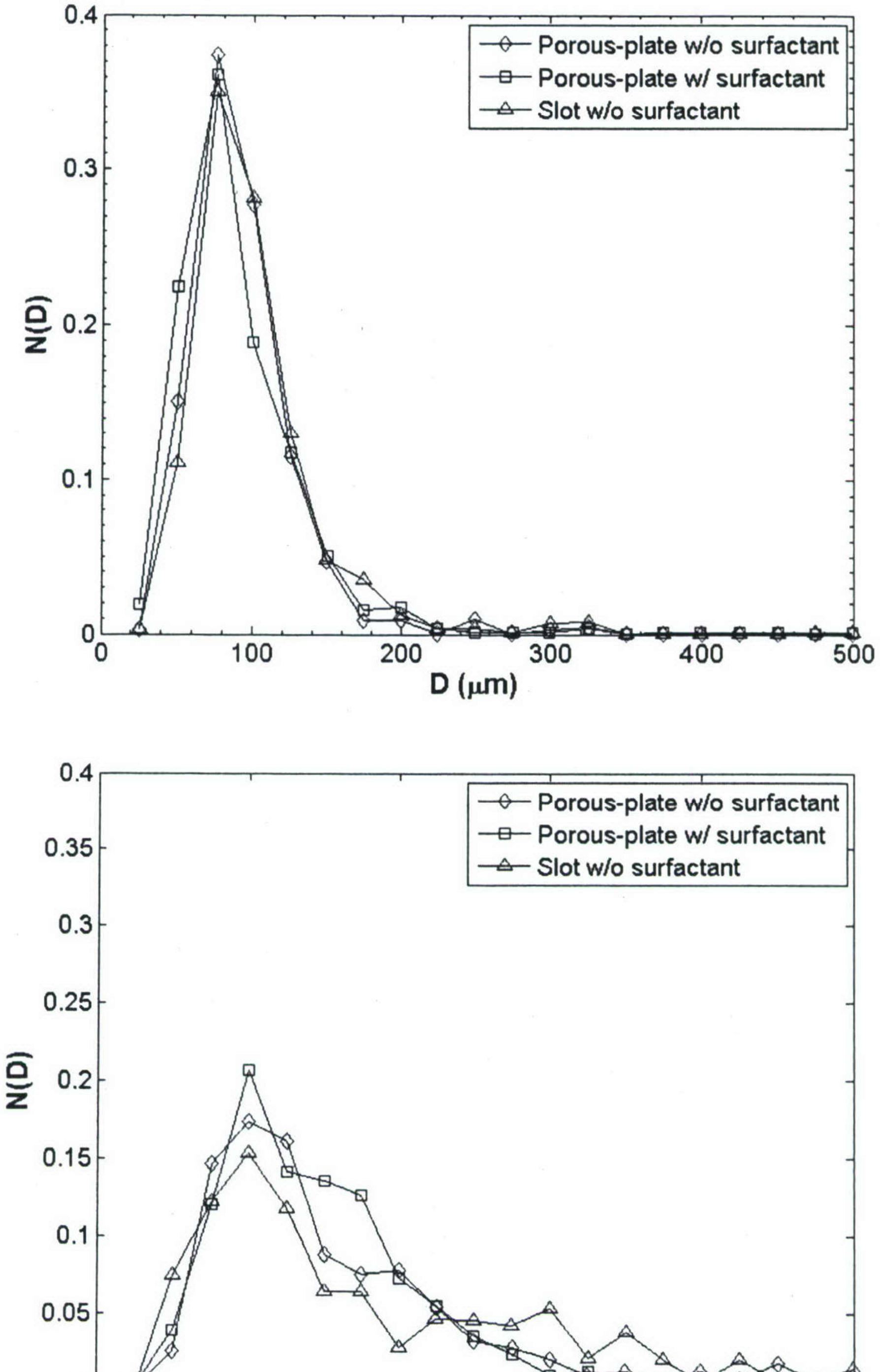

FIGURE 19: Bubble size distributions at 20.0 ms^{-1} free-stream speed with the porous-plate injector with and without surfactant and the upstream slot injector at (X-X_{inj} = 9.3 m) for (upper) 4.81 m^3min^{-1} injection and (lower) 15.3 m^3min^{-1} injection. Data were collected from the near-wall bubble cameras during Test 1a.

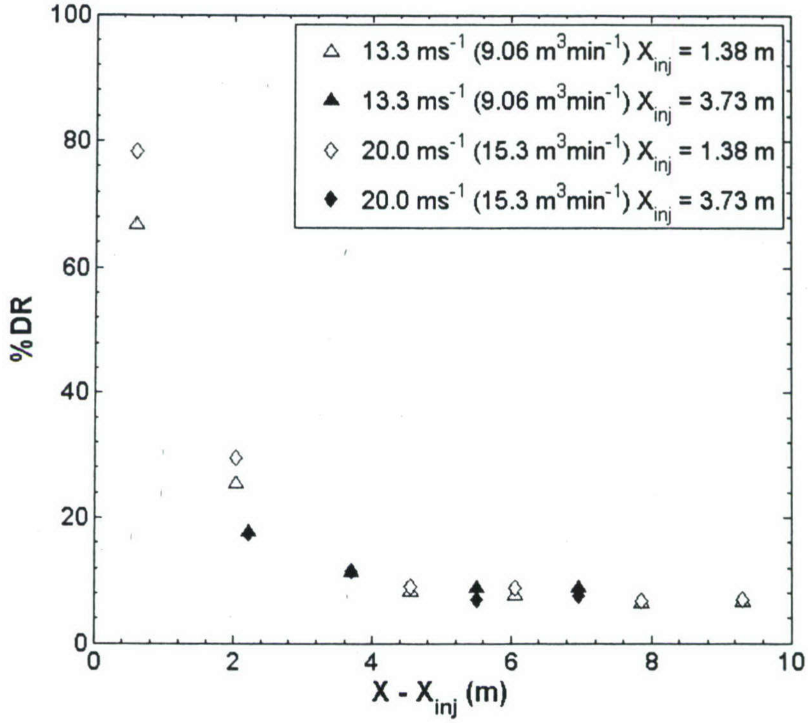

FIGURE 20: $\%DR$ versus X- X_{inj} (m) from Test 1a from Slot 1 (X_{inj} = 1.38 m) or Slot 2 (X_{inj} = 3.73 m) at free-stream speeds of 13.3 and 20.0 ms^{-1}. Open symbols represent slot 1 injection and closed symbols represent slot 2 injection. Results indicate that boundary layer thickness at the point of injection has little effect on drag reduction.

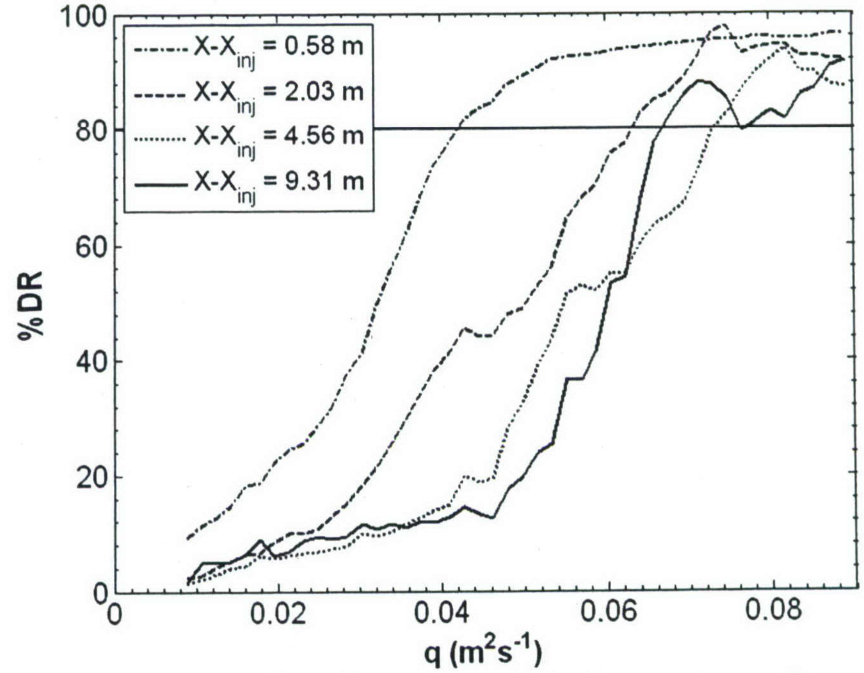

FIGURE 21: *%DR* versus *q*, the volumetric gas injection rate per unit span (m^2s^{-1}) from Test 1b for 11.1 ms^{-1} at four downstream locations. The solid horizontal line at *%DR* = 80% is the threshold used for defining ALDR.

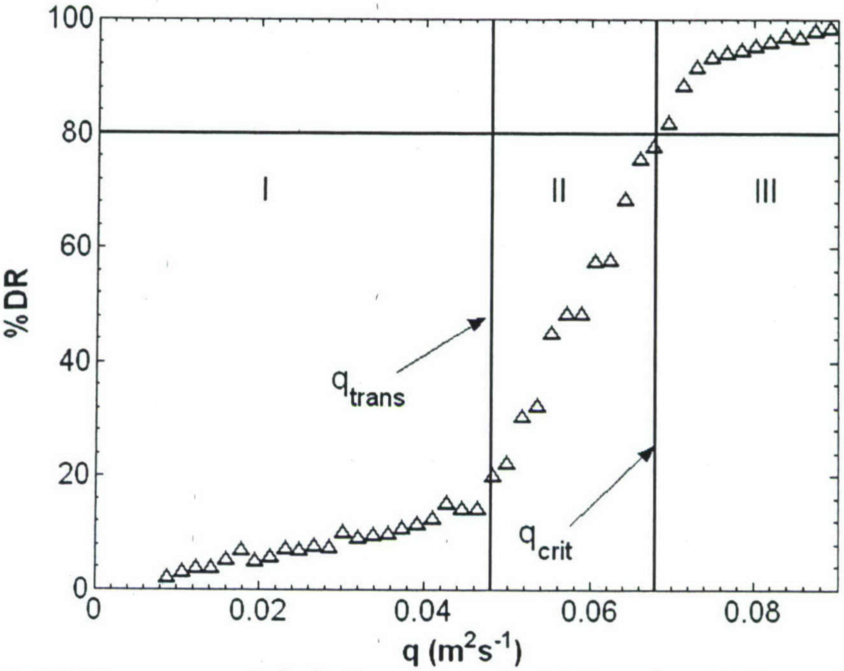

FIGURE 22: %*DR* versus *q* (m^2s^{-1}) from Test 1b 11.1 ms^{-1} at $X\text{-}X_{inj}$ = 6.05 *m*, which illustrates the three regimes of BDR and ALDR: I) a BDR regime where drag reduction is nearly linear with gas injection; II) a transitional region with a much steeper slope; and III) an ALDR regime where a maximum level of drag reduction is achieved.

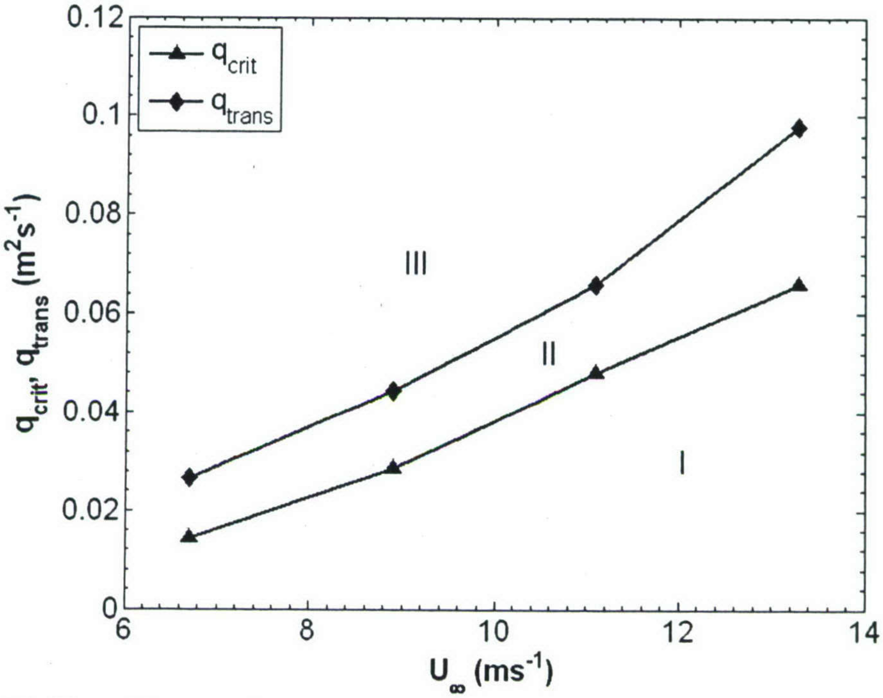

FIGURE 23: Transition gas injection rate, q_{trans} and critical gas injection rate, q_{crit}, (m^2s^{-1}) versus free-stream speed determined from Test 1b data. These two curves define the boundaries for the three drag reduction regions: I) BDR, II) transition region between BDR and ALDR, and III) ALDR.

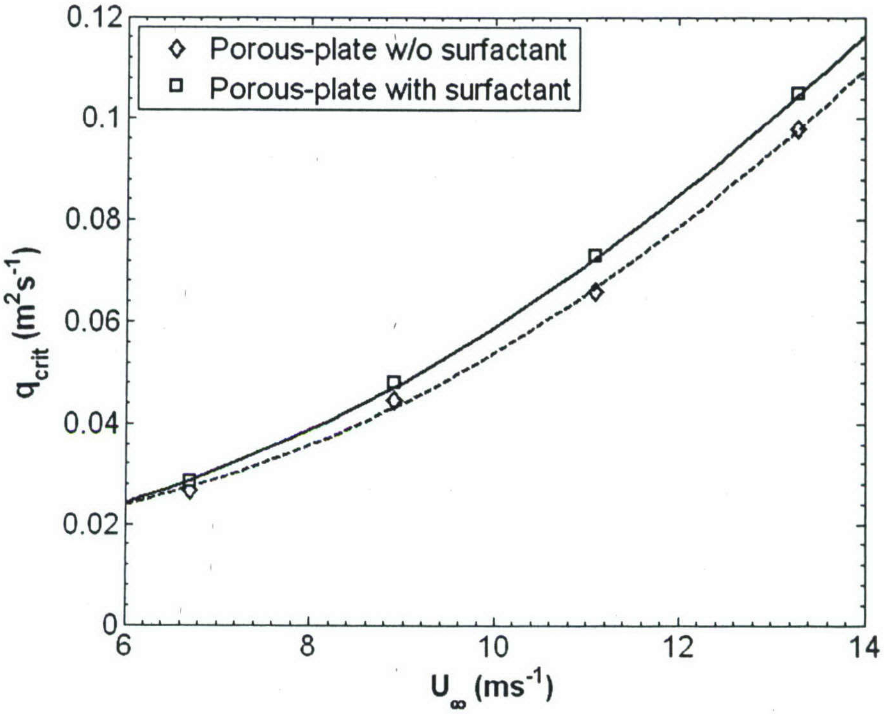

FIGURE 24: Critical gas injection rate, q_{crit} (m^2s^{-1}), for ALDR for the porous-plate injector without (◊) and with surfactant () in the background tunnel volume. The lines represent a least-squares quadratic fit to the experimental data collected during Test 1b.

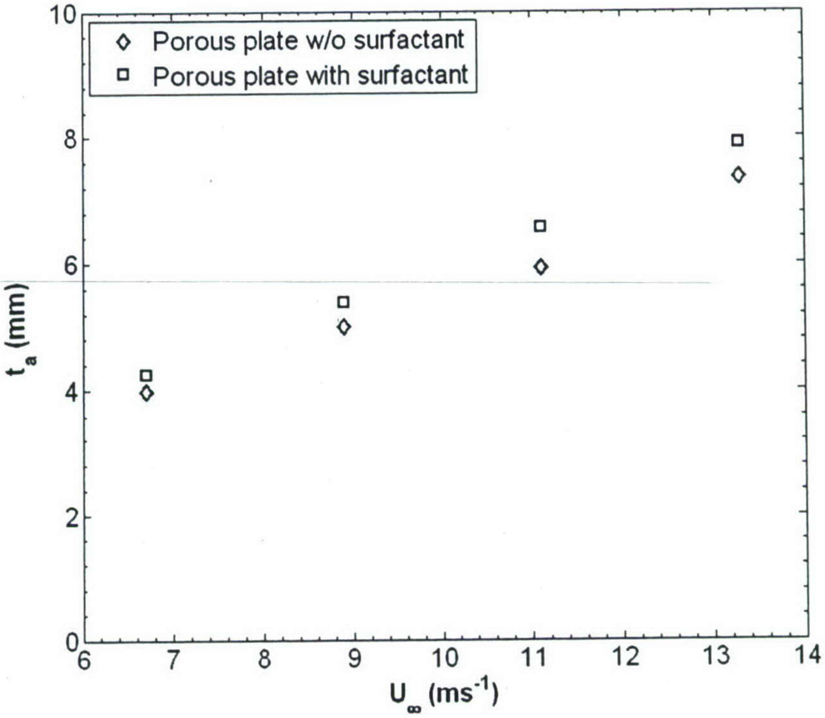

FIGURE 25: Critical air layer thickness, $t_a = Q_a/BU_\infty$, as a function of free-stream speed, U_∞, for ALDR with injection from the porous-plate injector with and without surfactant in the tunnel background. These data were from Test 1b.

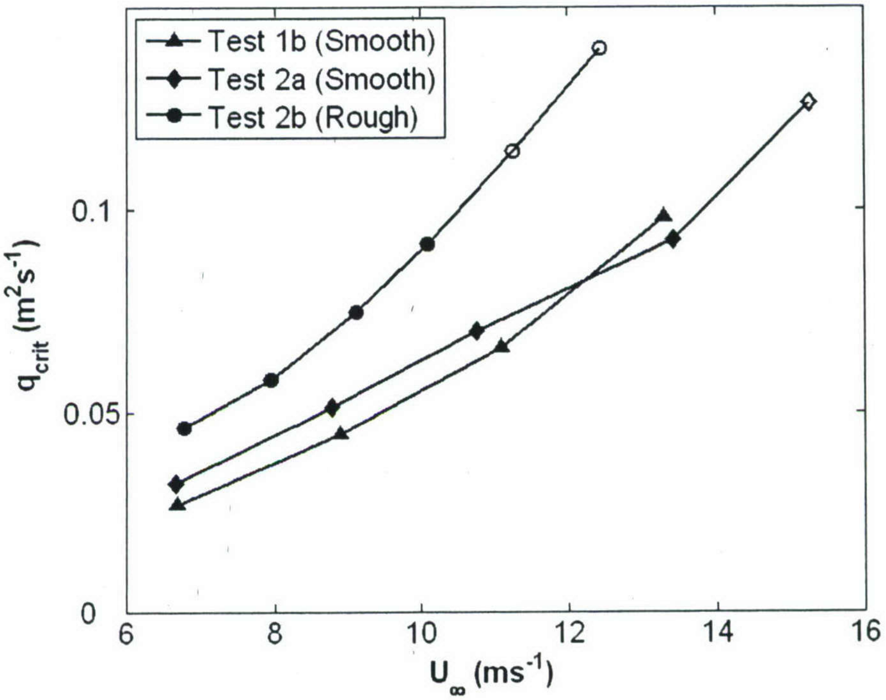

FIGURE 26: q_{crit} versus U_∞ for ALDR. Outlined symbols correspond to data points that exceeded the flow meter calibration range and are only estimates. Smooth model ALDR experiments, Tests 1b and 2a were conducted about a year apart with different injector geometry. The roughened model, Test 2b, was tested immediately following Test 2a with the same injector.

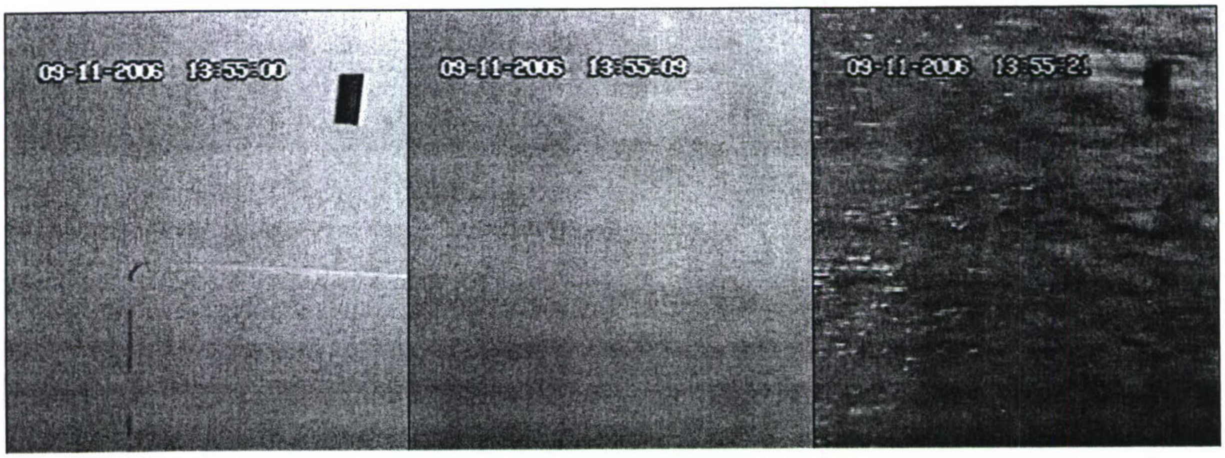

FIGURE 27: Images recorded during Test 2b of the roughened model surface at 6.8 ms^{-1}: (left) no injection; (center) bubble drag reduction; and (right) air layer drag reduction.